General Disclaimer

One or more of the Following Statements may affect this Document

- This document has been reproduced from the best copy furnished by the organizational source. It is being released in the interest of making available as much information as possible.

- This document may contain data, which exceeds the sheet parameters. It was furnished in this condition by the organizational source and is the best copy available.

- This document may contain tone-on-tone or color graphs, charts and/or pictures, which have been reproduced in black and white.

- This document is paginated as submitted by the original source.

- Portions of this document are not fully legible due to the historical nature of some of the material. However, it is the best reproduction available from the original submission.

N-3E-70-1

INVESTIGATION OF FACTORS AFFECTING THE PERFORMANCE OF POROUS STRUCTURES USED AS OXYGEN FUEL CELL ELECTRODES

by

T. Katan

Lockheed Palo Alto Research Laboratory
LOCKHEED MISSILES & SPACE COMPANY
A Group Division of Lockheed Aircraft Corporation

prepared for

NATIONAL AERONAUTICS AND SPACE ADMINISTRATION

NASA Lewis Research Center
Contract NAS 3-11833
R. E. Post, Project Manager

NOTICE

This report was prepared as an account of Government-sponsored work. Neither the United States, nor the National Aeronautics and Space Administration (NASA), nor any person acting on behalf of NASA:

A.) Makes any warranty or representation, expressed or implied, with respect to the accuracy, completeness, or usefulness of the information contained in this report, or that the use of any information, apparatus, method, or process disclosed in this report may not infringe privately-owned rights; or

B.) Assumes any liabilities with respect to the use of, or for damages resulting from the use of, any information, apparatus, method or process disclosed in this report.

As used above, "person acting on behalf of NASA" includes any employee or contractor of NASA, or employee of such contractor, to the extent that such employee or contractor of NASA or employee of such contractor prepares, disseminates, or provides access to any information pursuant to his employment or contract with NASA, or his employment with such contractor.

Requests for copies of this report should be referred to

National Aeronautics and Space Administration
Scientific and Technical Information Facility
P.O. Box 33
College Park, Md. 20740

N-3E-70-1

FINAL REPORT

INVESTIGATION OF FACTORS AFFECTING THE PERFORMANCE OF POROUS STRUCTURES USED AS OXYGEN FUEL CELL ELECTRODES

by

T. Katan

Lockheed Palo Alto Research Laboratory
LOCKHEED MISSILES & SPACE COMPANY
A Group Division of Lockheed Aircraft Corporation
Palo Alto, California 94304

prepared for

NATIONAL AERONAUTICS AND SPACE ADMINISTRATION

December 1969

CONTRACT NAS 3-11833

NASA Lewis Research Center
Cleveland, Ohio
R. E. Post, Project Manager

FOREWORD

This is a final report describing work conducted for the National Aeronautics and Space Administration, Lewis Research Center, under Contract NAS 3-11833, during the period 1 July 1968 to 8 December 1969. The work was performed at the Lockheed Palo Alto Research Laboratory, Palo Alto, California 94304, with Dr. R. E. Post, Direct Energy Conversion Division, NASA-Lewis Research Center, as Project Manager.

Dr. T. Katan was program manager and principal investigator. Valuable laboratory assistance was provided by Mr. G. J. Kersels for a 3-month period, and discussions with Mr. H. F. Bauman led directly to the results in Section 7 and to important improvements in the apparatus. Useful suggestions and discussions were also contributed by Drs. G. B. Adams, R. E. Post, and A. Wheeler, and by Messrs. G. W. Allen and G. J. Kersels.

Consultants were Dr. E. A. Grens, Associate Professor of Chemical Engineering, University of California, Berkeley, and Dr. A. J. Shaler, formerly Chairman of the Department of Metallurgy, Pennsylvania State University.

ABSTRACT

Design methods are detailed for improving structures of oxygen electrodes. Prime emphasis is given to control of liquid distribution and configuration, best accomplished by using electrode structures which are well characterized. The critical role of a pendular-funicular transition state for correct internal liquid configuration is shown, together with its relation to design and performance. Experimental studies included a determination of synergistic effects with double-porosity structures and the necessity of catalyst placement toward the electrolyte side of the electrode. Gold was found to act suitably as an oxygen catalyst, and Teflon in the gas electrode acted as though imparting differential pressure to the system. Theoretical studies involved design recommendations for evaporating electrodes and the relation of structural parameters of porous systems.

CONTENTS

ILLUSTRATIONS

Section 1
SUMMARY

This report presents design methods for improving structures of oxygen electrodes operating in 13.5 M KOH at 95°C. Experimental and theoretical studies are described which are concerned with structural parameters and operating conditions required for maximum performance. Tests on catalyst loading and distribution and on Teflon loading are included.

High performance of film-type oxygen cathodes was found to depend on the formation of continuous networks of gas and liquid in the porous medium. Disruption of either network, by excessive flooding or by rupture of liquid filaments at high differential pressures, causes deterioration in electrode performance. Prime emphasis is given to the control of liquid distribution and configuration, best accomplished by using electrode structures which are well characterized (Section 4).

The existence of a pendular-funicular transition state is demonstrated, and the critical role of this transition state for correct internal liquid configuration is shown,together with its relation to design and performance of oxygen gas electrodes (Section 5). The pendular-funicular transition state is defined as that state in which bulk electrolyte inside a porous electrode just forms continuous interconnected liquid paths on the pore walls without flooding the pores, leaving some wall areas still unflooded by electrolyte which are exposed to the continuous network of gas channels through the electrode. Before these continuous electrolyte paths are formed, a pendular state exists, and afterward a funicular state exists. With a balanced configuration near this transition state, the unflooded areas (where the important electrochemical processes occur) are adjacent to good ionically conducting paths of electrolyte, have short transport distances to these electrolyte paths, and retain a maximum of such area accessible to the gas channels.

Experimental studies utilized the well-known properties of sphere beds which were built up as oxygen electrodes in a unique apparatus (Section 3). In these studies, current densities for single-porosity electrodes having 156-μ diameter silver spheres were 27 mA cm^{-2} at 500 mV versus the H_2 reference electrode in the same solution when the differential pressure across the built-up electrode was 25 cm of water (2450 N/m^2). When the differential pressure was varied and increased to 42 cm of water (4100 N/m^2), a maximum in current density was obtained, 50 mA cm^{-2} at 500 mV. It was found that the effect of sphere diameter (effective pore diameter) and electrode thickness depended on the differential pressure used and that an optimum differential pressure exists at which performance is maximized (sections 4.2, 4.3, and 4.4). Addition of a fine layer of silver spheres, 14μ in diameter, at the electrolyte side of the 156-μ-diameter silver sphere bed caused a general improvement in performance in the differential pressure range studied, 5 to 100 cm of water (490 to 9800 N/m^2), and an increase in the maximum current density was observed, 63 mA cm^{-2} at 500 mV. Double-porosity electrodes performed better than predicted because of an unexpected synergistic effect (section 4.5). The best performance was obtained with an all-silver double-porosity electrode having a coarse layer of 54-μ spheres and a fine layer of 14-μ spheres at the electrolyte side. The optimum differential pressure was not attained with this electrode at the maximum value tested, 90 cm of water (8900 N/m^2), when the observed current density was 125 mA cm^{-2} at 500 mV (section 4.5).

Treatment of the coarse layer of the double-porosity electrode consisting of 156-μ- and 14-μ-diameter silver spheres with platinum catalyst at 0.8 mg/cm^2 of facial electrode area generally improved performance for this structure, and a maximum of 66 mA cm^{-2} at 500 mV was observed. However, treatment of the coarse layer with more platinum, 8 mg/cm^2, caused a deterioration in performance for differential pressures less than 57 cm of water (5600 N/m^2) because of uncontrolled flooding induced by the capillarity of these excessive amounts of platinum for the pressure range studied (section 4.7). The addition of powdered Teflon at only 3.5×10^{-3} mg/cm^2 of facial electrode area to the coarse layer of this last electrode improved its performance at a differential pressure of 42 cm of water (4100 N/m^2) from 46 to 79 mA cm^{-2} at 500 mV. Teflon effectively acts as though it imparts a differential pressure to the electrode (section 4.11).

Generalizations could be made for triple-porosity structures to explain the experimental results with these structures, and in catalyst distribution experiments it was found that a catalyst is most effective when placed at the electrolyte side of the electrode. In other experiments, it was determined that platinized nickel structures were comparable in behavior to platinized silver structures, although slightly poorer, and that gold could act as a suitable oxygen catalyst (Section 4).

In theoretical analyses, the influence of structure on performance was indicated during gross evaporation from the electrode, when unusual internal pressures may develop (Section 6), and the structural parameters were related for guidance in design (Section 7).

Simple electrode structures are recommended as oxygen electrodes based on the results of this study (Section 8).

The appendix provides a calculation of the cross-sectional area and perimeter of a sphere bed in a closest packing array.

Section 2
INTRODUCTION

2.1 PURPOSE AND BACKGROUND

Goals accomplished under this contract were (1) experimental analyses for determining structural parameters of practical importance in optimizing oxygen electrodes and (2) theoretical evaluations of structural parameters in order to help formulate principles of oxygen electrode design. The ultimate aim of this fuel-cell research is to devise from these principles a systematic method for design of optimum fuel-cell electrodes for specified applications. The immediate objective is to provide information to improve the operating characteristics of the oxygen electrode.

The Lewis Research Center, National Aeronautics and Space Administration, authorized the program which was proposed in LMSC-D080258 and which was put into effect in July 1968. At the time of authorization, little was known of the mode of operation of porous oxygen gas electrode structures. For guidance in the design, fabrication, and operation of oxygen electrodes, an understanding was required of the complex processes occurring in porous oxygen electrode structures which often even defy description. The research and development work was conducted in the Electrochemistry Laboratory of the LMSC Materials Sciences Laboratory.

This final report presents the results of the complete program. Essentially, the report consists of two parts: the first two sections in the body of the report are concerned with detailed experimental analyses of the oxygen electrode, and the last sections deal with the theoretical analyses of the mode of operation and structure of oxygen electrodes.

2.2 SCOPE

In the study of porous gas electrodes, the complexity of practical systems frequently prevents simple interpretation of effects caused by changes in pore size, electrode thickness, and pressure difference across the electrode. In this study, some of these effects have been examined with electrodes made of beds of small silver spheres of uniform size resting on a fine silver mesh. The use of a sphere bed enables the properties of a complex porous matrix to be approached while having the advantage of a system that can be specified and characterized for both the partially or the completely infiltrated conditions (Refs. 1 – 7) and the different packing configurations (e.g., see Refs. 8 – 11).

In this report, descriptions and interpretations are given of measurements taken of the performance of oxygen electrodes consisting of such beds of silver spheres operating in 13.5 M KOH at 95°C. Spheres in sizes from 14 to 156 μ in diameter and electrode thicknesses from about 200 to 2000 μ were used. In these electrodes, the electrochemical reaction is believed to occur beneath a film coating the walls of the gas-filled pores between the spheres.

Experimental studies were at first confined to all-silver electrodes to determine the optimum electrode thickness and the effect of sphere diameter (effective pore diameter). The finding that differential pressure had a strong influence on these two parameters complicated the work but enabled a better understanding of the results. In accord with the planned program, double- and triple-porosity structures were also examined with all-silver electrodes. Experimental results and apparatus are described in some detail in the hope that this will prompt suggestions or encourage other work.

Assorted experiments were also conducted for evaluations of platinized nickel as a catalyst, of gold as an oxygen catalyst, of Teflon loading, and of platinum loading and distribution on silver spheres. Although results were not always conclusive, these probe experiments provided useful information which aided in the final analyses.

Theoretical treatments are given in the last parts of this report. They include a presentation of the pendular-funicular transition state theory, some design suggestions for electrodes from which electrolyte evaporation occurs, and the relation of structural parameters to assist in design and fabrication.

Section 3
EXPERIMENTAL APPARATUS AND PROCEDURE

3.1 INTRODUCTION

It is the purpose of this section to describe in some detail the apparatus and procedure used in measurements of the performance of oxygen electrodes consisting of silver sphere beds operating in 13.5 M KOH at 95°C. Spheres were used in sizes from 14 to 156 μ in diameter, and electrode thicknesses were from about 200 to 2000 μ. In these electrodes, the electrochemical reaction is believed to occur beneath a film coating the walls of the gas-filled pores between the spheres.

Experiments were conducted in which preweighed amounts of silver spheres were deposited to form sphere beds resting on a fine silver mesh having uniform square holes much smaller than the sphere diameter. The electroformed mesh was sealed to the bottom of a tube, 1.26 cm in inside diameter, and to a silver rim which supplied external electrical contact, as shown conceptually in Fig. 1. The spheres, added at room temperature, were actually held in a small retaining chamber in the working electrode housing, below the electrolyte level, to be heated to the electrolyte temperature of 95°C before being dropped onto the working electrode. The bed thickness was increased by known increments by dropping known amounts of spheres onto the electrode. In some cases, nickel spheres and platinum- or gold-coated silver spheres were used. The determined density of the loosely packed spheres and the cross-sectional area were used to calculate bed thickness. The deposited sphere bed was employed as an oxygen electrode, and the performance of the electrode was determined at different thicknesses and applied oxygen pressure.

By using different sizes of spheres, the effective pore size was changed without appreciably changing the porosity. "Double-porosity" as well as single-porosity

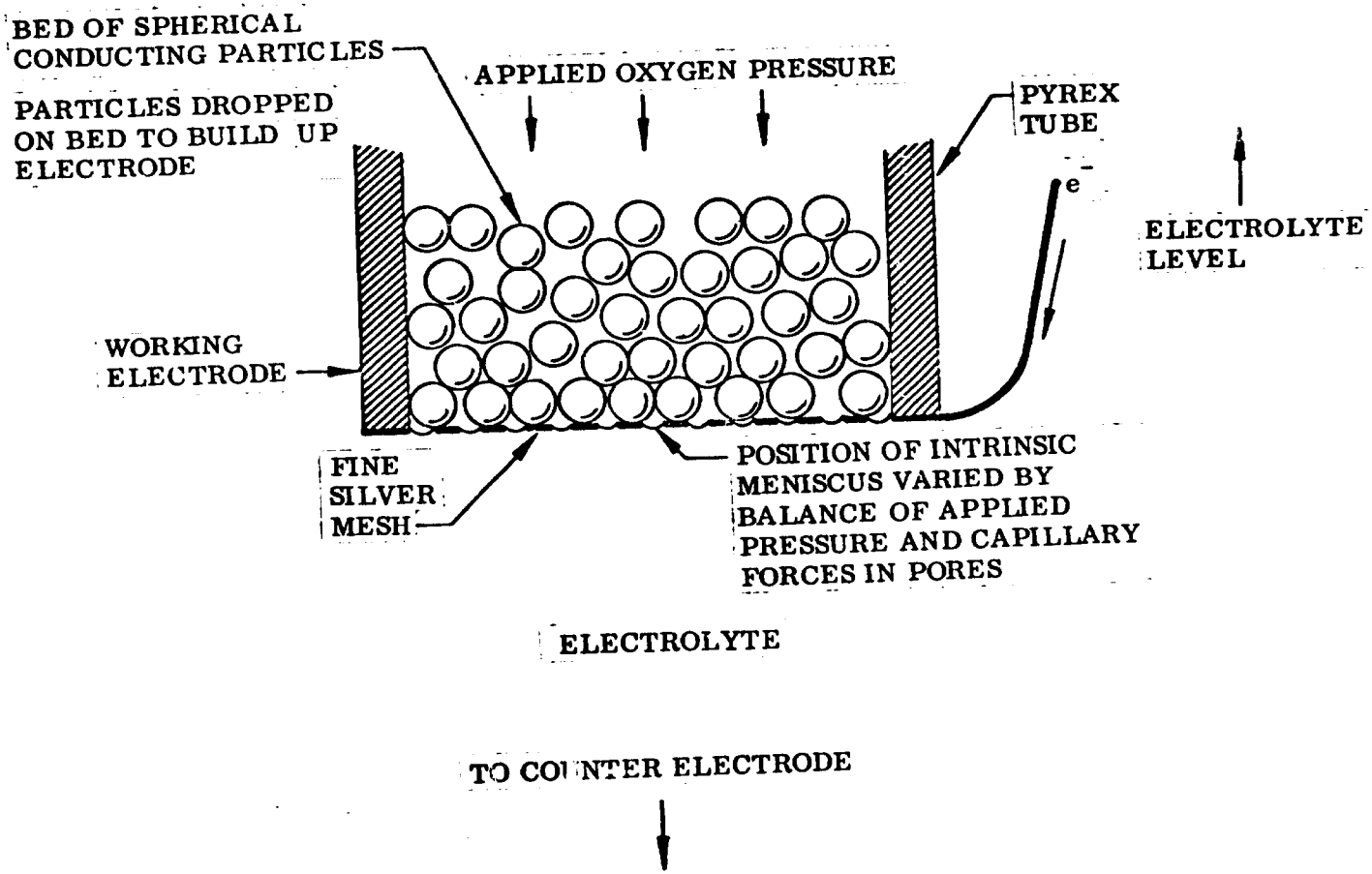

Fig. 1 Schematic Representation of Arrangement and Operating Principle of the Working Electrode

electrode structures were built up in this way and studied. Although the double-porosity electrodes had nearly uniform porosity, the fine layer had smaller effective pores. The pressure difference across the electrode, i.e., the differential pressure, was initially adjusted to 25 cm of water head so that the silver mesh remained unflooded on the gas side and so that no bubbling occurred. After the beds were built up, changes were made in the differential pressure so that the relative amount of electrolyte infiltration was changed, and the effect on electrode performance was observed. Bubbling did not occur with the built-up electrodes.

3.2 APPARATUS

3.2.1 General Arrangement

The apparatus required to maintain and observe the oxygen electrode consisted of the electrolytic cell, oxygen pressure and flow regulation equipment, and monitoring instrumentation for measuring the electrode response. The general experimental arrangement is shown in Figs. 2, 3, and 4. In Fig. 2 is shown the arrangement of the apparatus and equipment in the laboratory, and Fig. 3 is a schematic diagram of the apparatus with the gas flows and electrical connections. The electrical circuits are shown in Fig. 4. It can be seen that no special or unusual equipment is required, and the arrangement resembles the one which was reported previously for the experiments at room temperature and at lower KOH concentration (Refs. 12, 13). Certain changes were required, however, to accommodate the new set of operating conditions, 95°C and 13.5 M KOH.

3.2.2 Electrolytic Cell and Thermostating Bath

A 1-liter polypropylene bottle was used to hold the electrolyte which contained a hydrogen reference cell as well as the working and counter electrodes, as shown in Fig. 3. The wide-mouth bottle was 9 cm in diameter and 19 cm high with a 5-cm-diameter mouth. This cylindrical bottle was placed in a thermostated water bath maintained at 95 ± 0.2°C inside a 4-liter polypropylene beaker, shown in

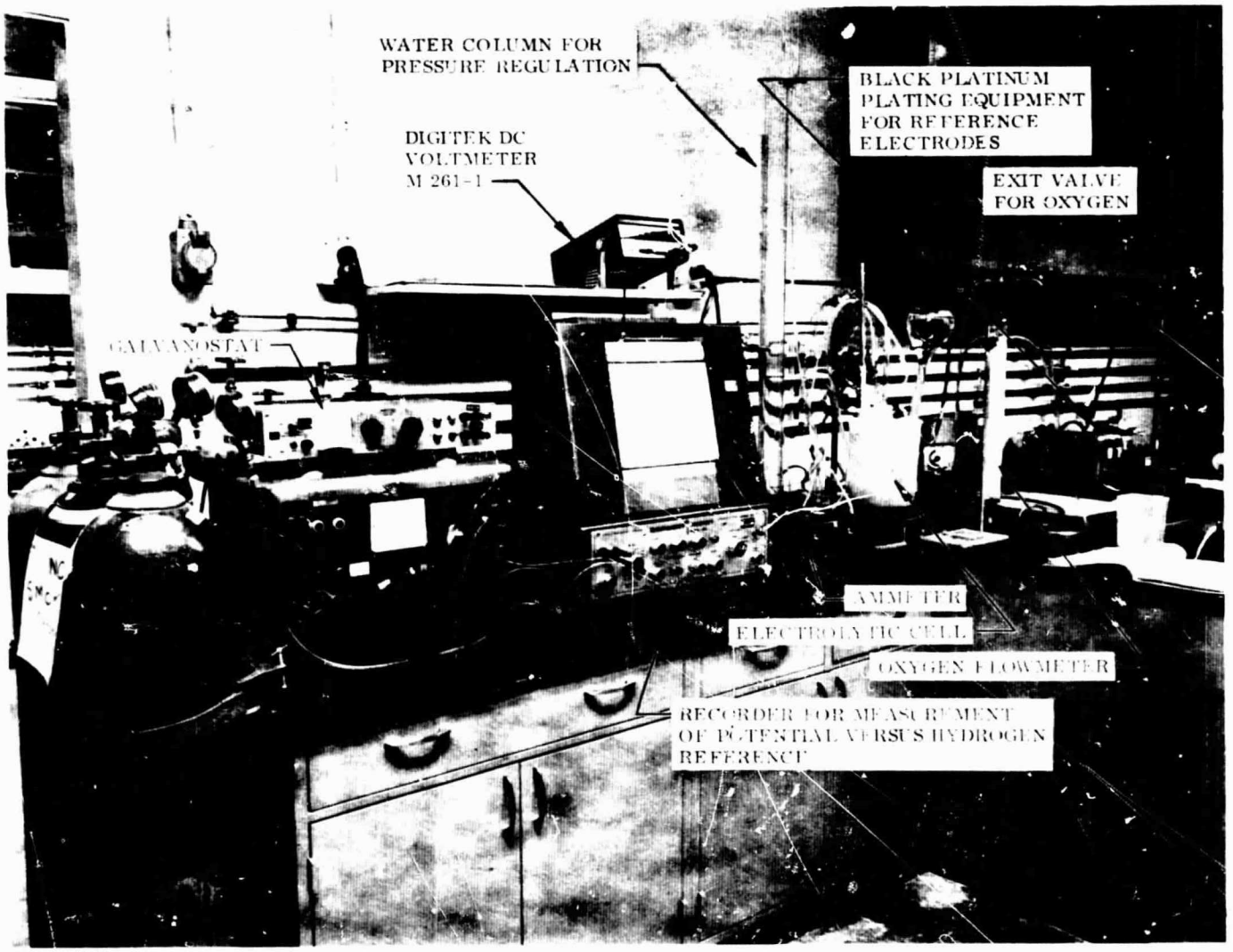

Fig. 2 Arrangement of the Experimental Apparatus and Equipment

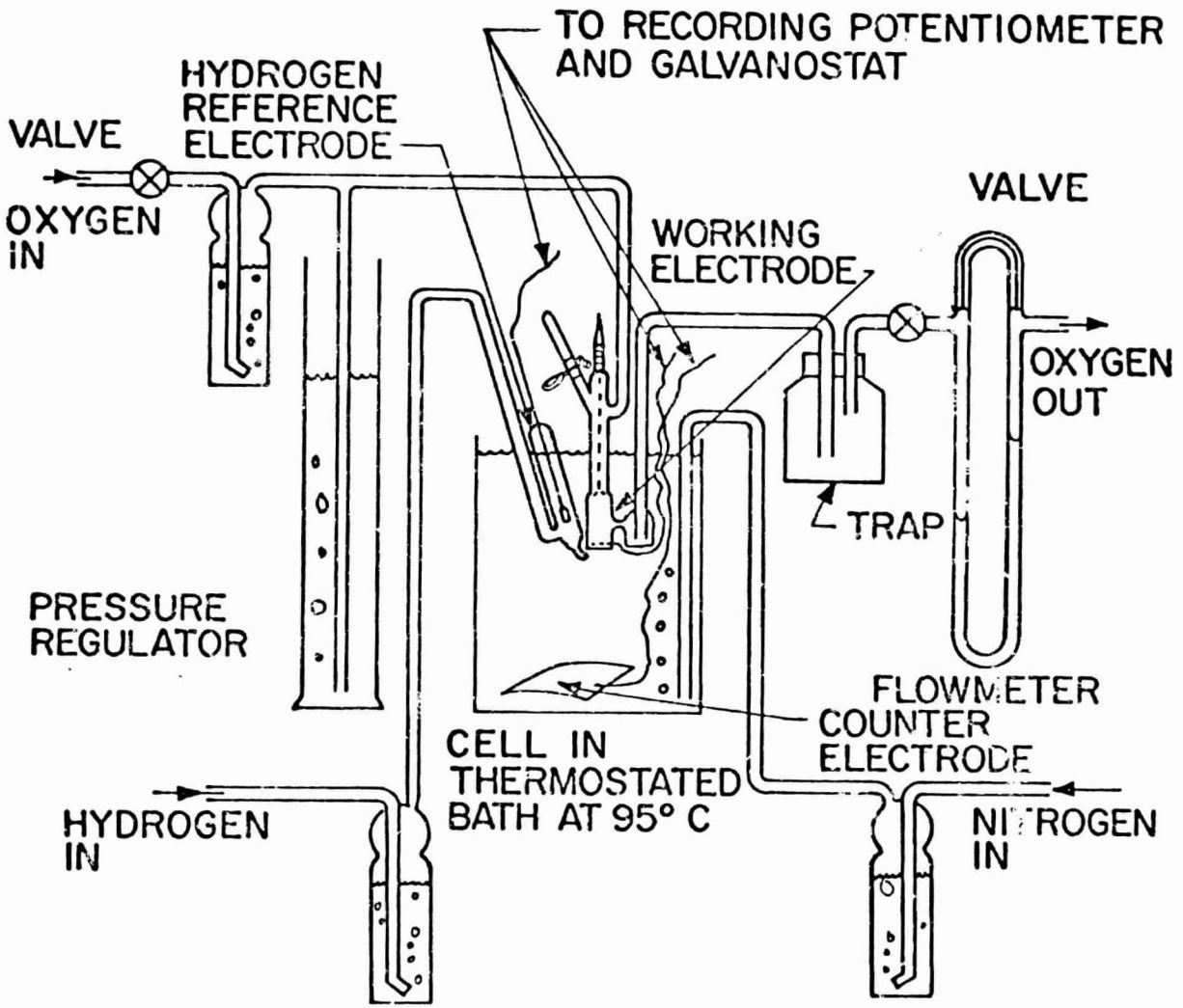

Fig. 3 Schematic Diagram of Apparatus for Oxygen Electrode Study

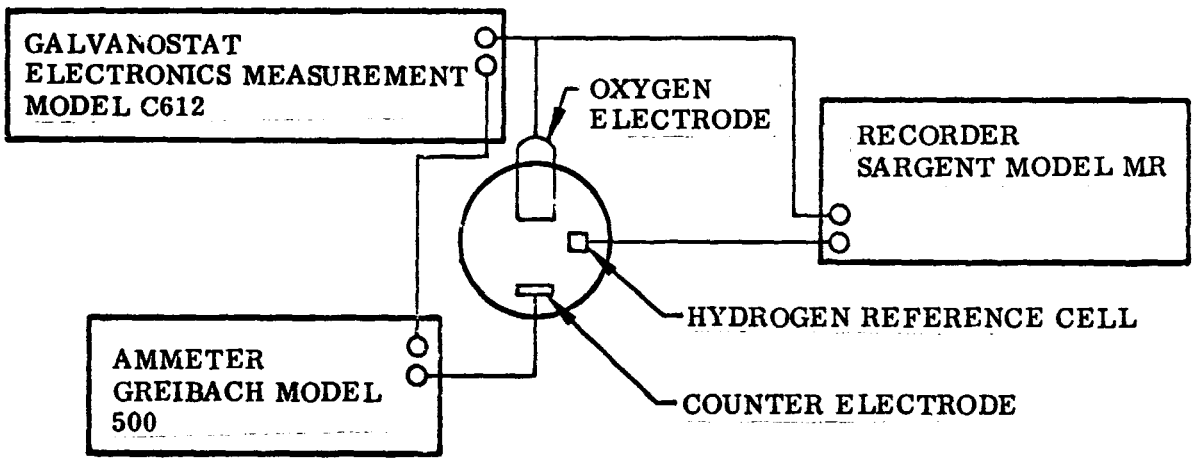

Fig. 4 Diagram of Electrical Circuit (Rubicon Potentiometer Model 2700 and Digitek DC Voltmeter Model 261-1 Used To Check Recorder)

Fig. 5. The bottle rested on a small aluminum table about 3 cm high which permitted the hot water to circulate around the bottle by means of a magnetic stirring bar situated below the table. The electrolyte level in the bottle was 2 cm below the level of the external water bath, and the electrolyte was continually purged with a stream of nitrogen at about 3 cc min^{-1} from a 1.5-mm-o.d. Teflon tube leading to and open at the bottom of the polypropylene bottle next to the counter electrode. This nitrogen stream furnished convective mixing and nitrogen saturation of the electrolyte and to some extent masked the surface of the electrolyte, which was open to the air, against carbon dioxide in the air. Evaporation loss of electrolyte during a typical experiment was usually less than 20 cc from the 900-cc volume of the 13.5 m KOH and was found not to affect the results of the work during the data accumulation period.

Hollow polypropylene spheres, 2 cm in diameter, were floated on the water bath to reduce evaporation losses. These Allplas floating spheres were purchased from Wire Machinery, Inc., Chicago, Illinois. Also, an inverted 1-liter volumetric flask, shown in Fig. 5, was used to replace the small amount of water evaporated from the thermostated bath to accurately maintain the water level during an experiment. An immersion heater in the bath was actuated by a temperature regulator, a Precision Scientific Co., Chicago, Illinois, Micro-Set, connected to a Fisher Scientific Co., Pittsburgh, Pennsylvania, Model 50 Unitized Bath Control. A thermometer was placed in the hot water bath to check the setting of the temperature regulator, and data collection was never started until 1 to 2 hr after the thermostated bath attained 95°C to assure temperature equilibration.

3.2.3 Working Electrode and Electrode Housing

The working electrode and the working electrode housing are shown in Figs. 6 through 9. The design of the working electrode can be seen in Fig. 6. The preweighed silver powder is added from a Pyrex vial, 7 cm long and 7 mm o.d., through a 7-mm-o.d. side arm, to the top of a conical, Pyrex trap door which is pressed tightly against the 10-mm-o.d. tube of the housing. The vial is attached to a

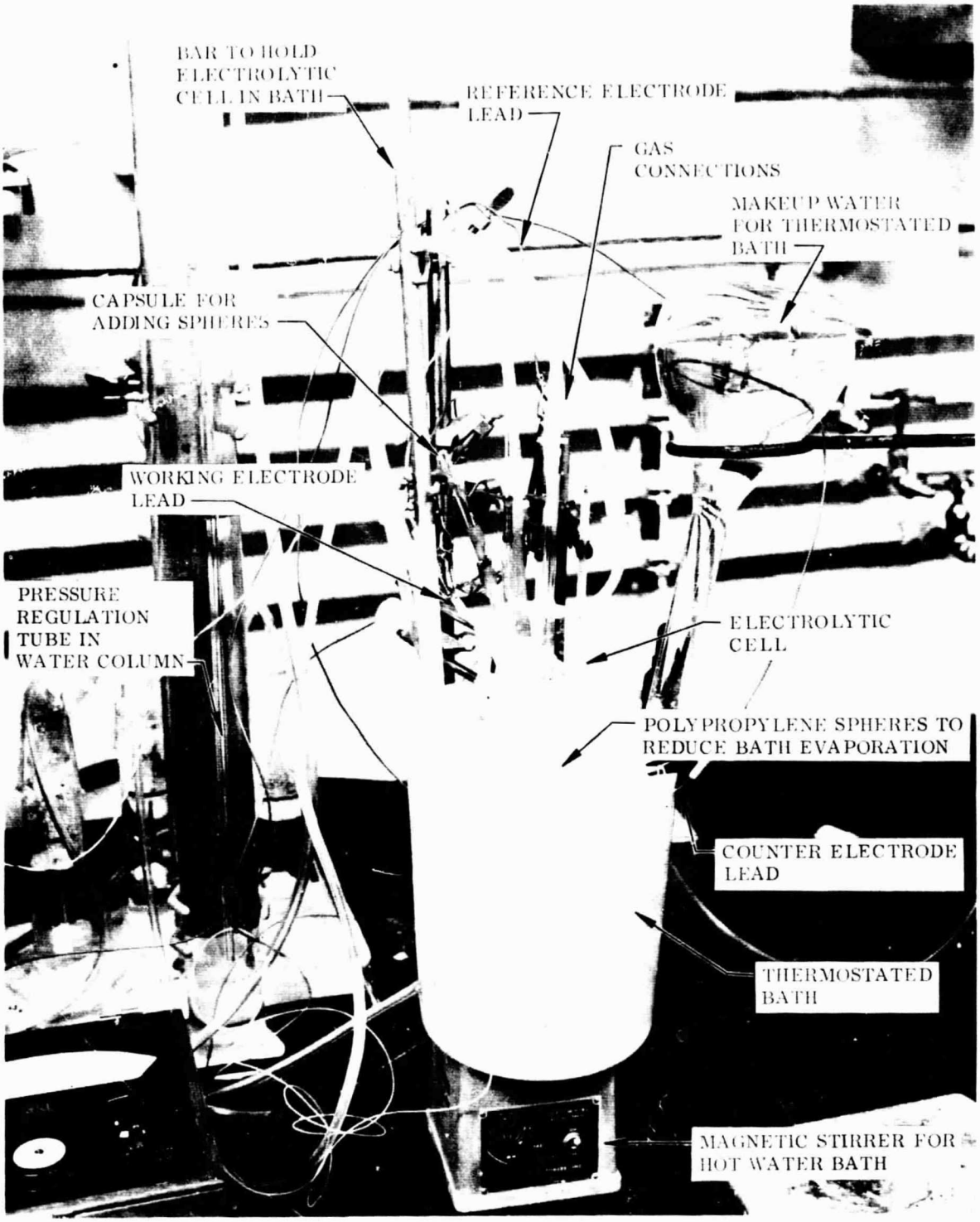

Fig. 5 Electrolytic Cell in Operation in Thermostated Bath

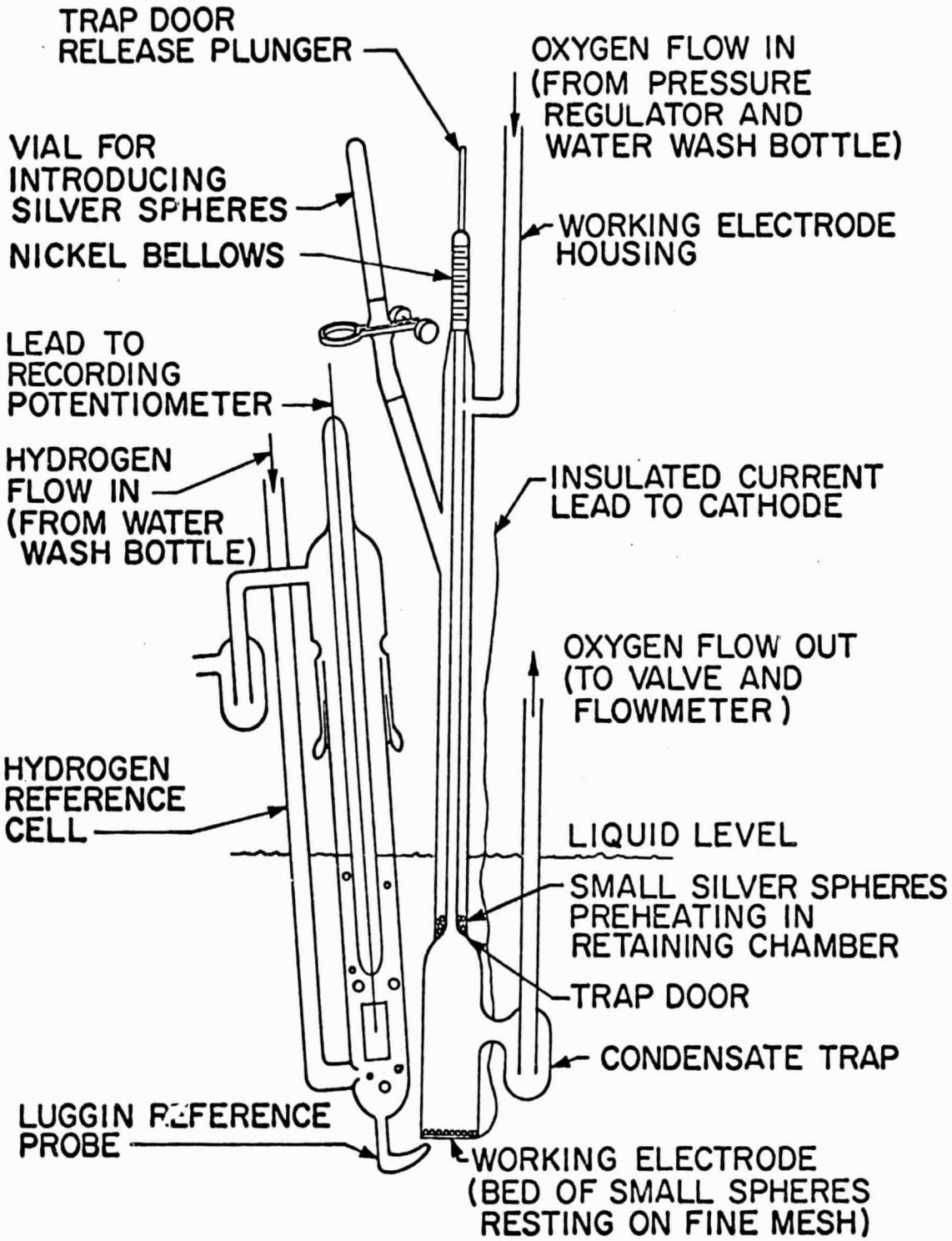

Fig. 6 Sketch of Working Electrode With Electrode Housing and Reference Electrode in Electrolytic Cell

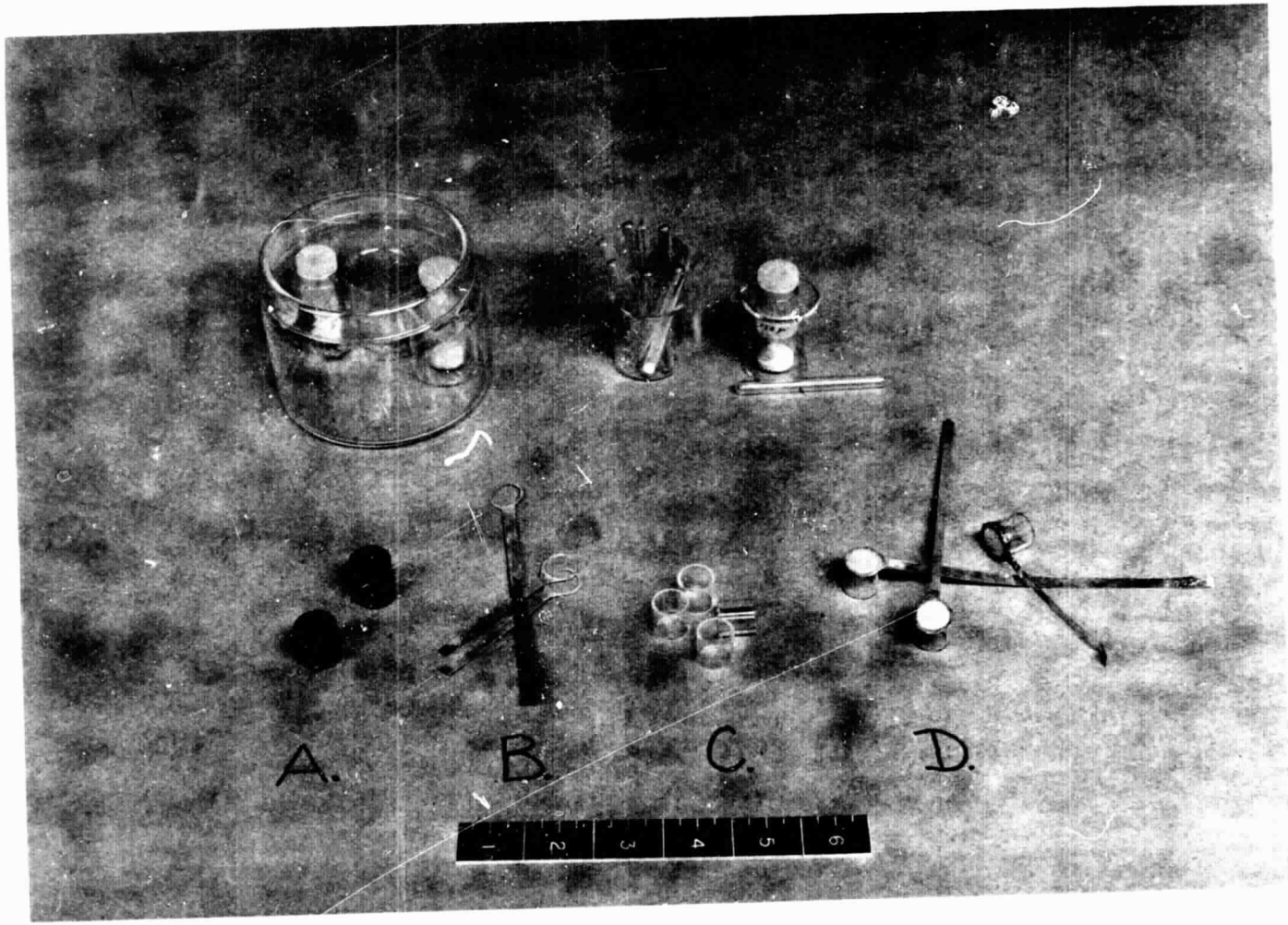

Fig. 7 Parts of the Working Electrode. A: Die used to trim silver foil rings. B: Silver foil rings, 6 mils thick, and expanded silver metal mesh used in some reinforced electrodes. C: Pyrex glass cylinders, cut to size, for holding working electrode support. D: Working electrode support ready for mounting to housing. Background: Silver spheres and capsules used to build up working electrode. Foreground: inch scale.

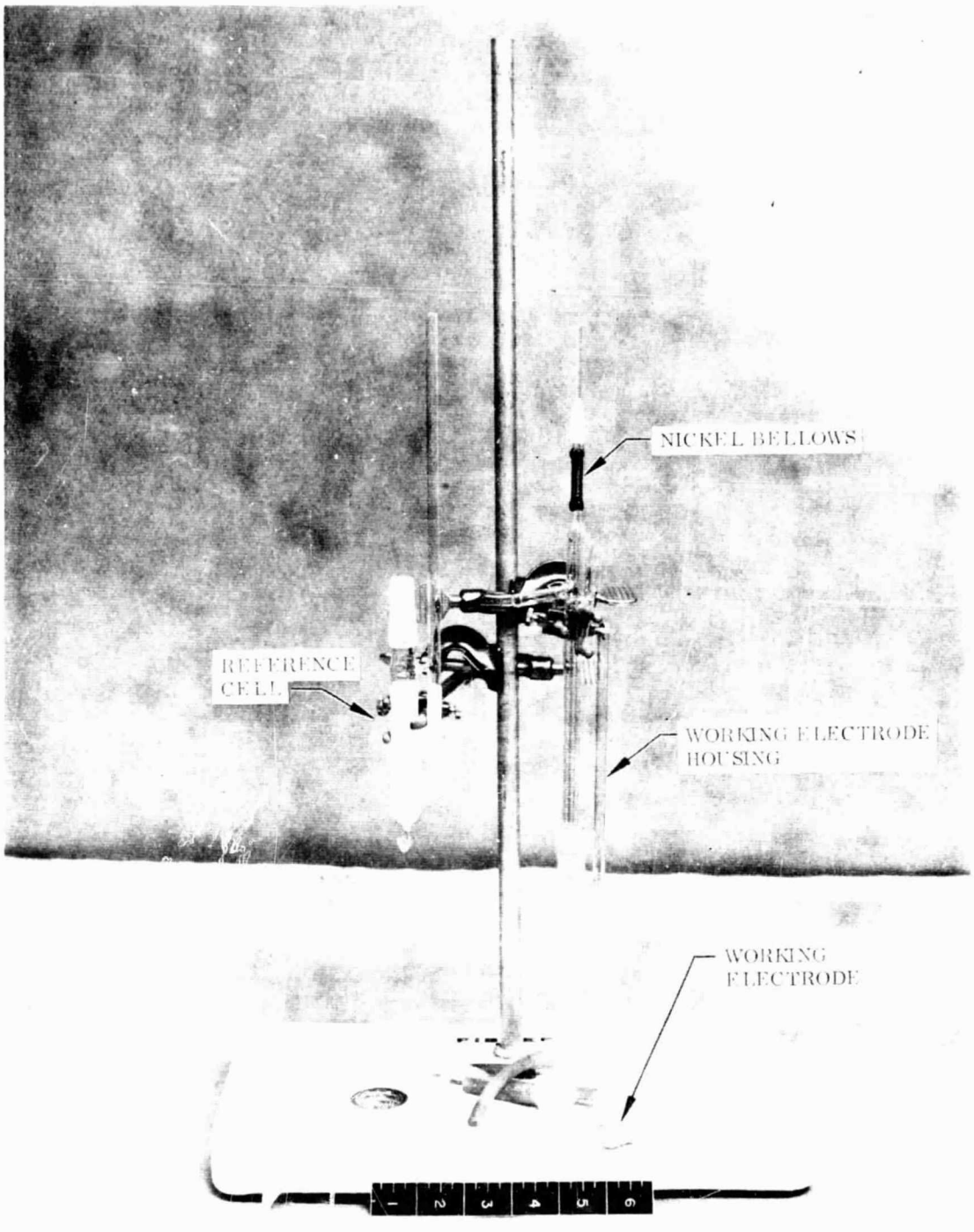

Fig. 8 Reference Electrode and Working Electrode With Housing Before Assembly

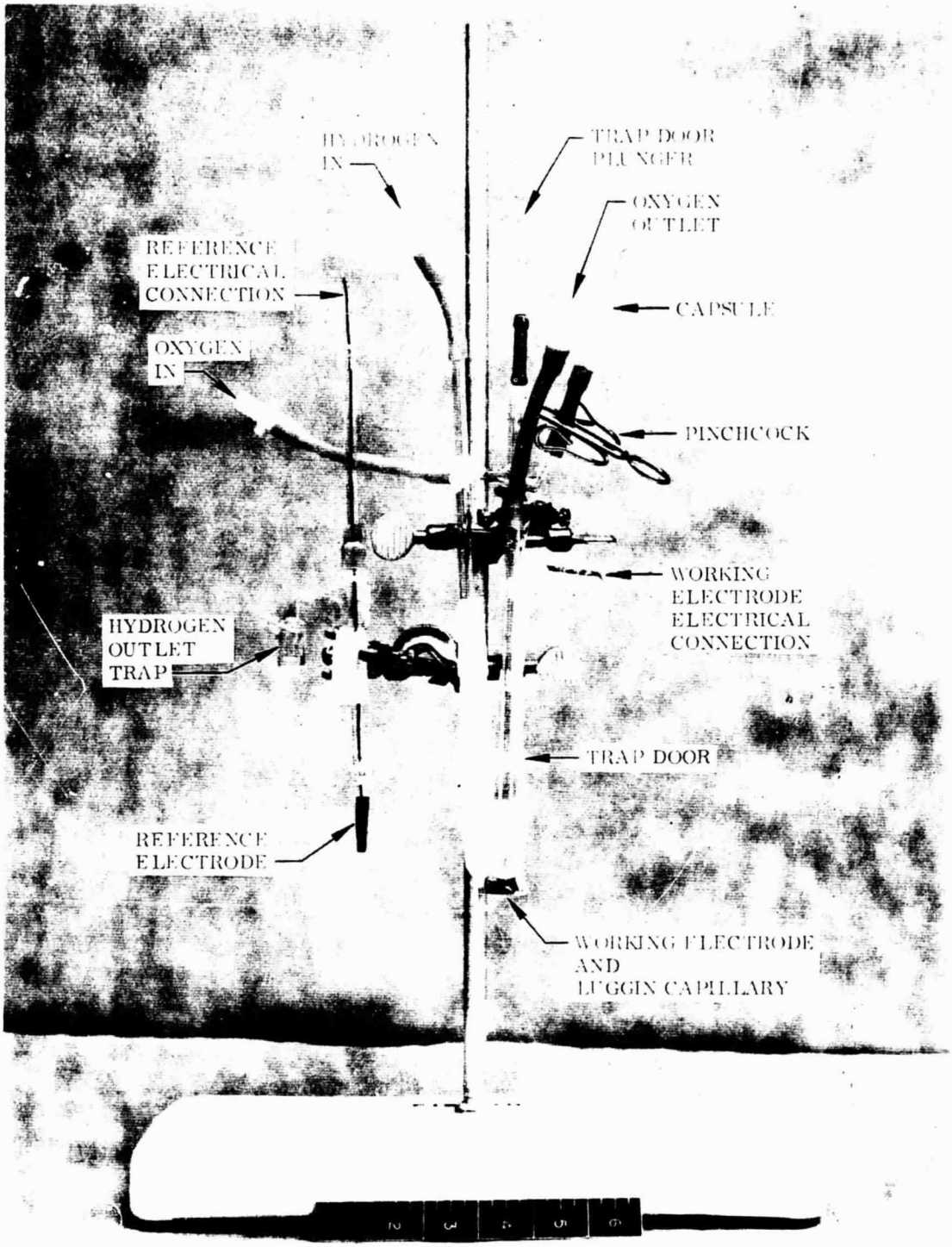

Fig. 9 Assembled Working Electrode and Reference Cell Ready for Insertion in Electrolytic Cell

neoprene tube connected to the side arm before the spheres are added. A pinchcock is used to seal the neoprene tube and maintain the applied oxygen pressure inside the housing when the Pyrex vials are exchanged during the buildup of the working electrode. A nickel bellows, P/N 1231 from Servometer Corp., Clifton, New Jersey, is sealed with Epon 828, Curing Agent Z, Shell Chemical Co., New York, N. Y., at its bottom end to the top of the 10-mm-o.d. housing tube and at its top end to a hollow, 3-mm-o.d. Pyrex plunger tube which leads to and is connected to the conical trap door below. The bellows supplies the tension needed to keep the trap door closed, and the plunger is pushed down to compress the bellows and open the door below while keeping the system sealed to maintain the internal oxygen pressure. After the added silver powder is heated to the temperature of the system while the powder rests on the trap door (i.e., after about 15 min), the trap door is opened, and the powder falls onto the electrode below to build up a uniformly thick layer. With the downward flow of oxygen into the housing, no powder hangup or condensate was observed inside the housing, mainly because the entering oxygen is relatively dry. A hole in the plunger tube permits oxygen to flow through the housing by passing through the plunger tube. The oxygen stream becomes more concentrated in water vapor from the saturated region above the electrode, and a trap collects condensate formed in the exit tube (about 0.3 cc in a 4-hr period).

The silver mesh support for the working electrode is sealed to a 1.5-cm-o.d. Pyrex tube which is attached to the 1.5-cm-o.d. Pyrex tube at the bottom of the housing before an experiment. A carborundum glass-cutting saw is used to cut these tubes to ensure a flush fit. The silver mesh supports with the attached Pyrex tubes were prepared in the steps indicated in Fig. 7 as follows:

- Silver foil, 6 mils thick, was cut into rectangles, stacked, and clamped.
- A guide hole was drilled, and this was followed by a high-speed drilling to size.
- The rectangles were cut roughly to size, clamped through their hole with the die shown in Fig. 7a, and the excess silver trimmed around the die to form a ring as shown in Fig. 7b. The ring had a 1.5-cm-o.d. and a 1.25-cm-i.d. to conform to the end of the Pyrex tube that acts as a holder.

- Pyrex tubes, 1.5-cm-o.d., were cut with a glass saw into 1.5-cm lengths, as shown in Fig. 7c.
- Silver electroformed mesh, 2000 LPI, Ruling No. 2001, from Buckbee Mears Co., St. Paul, Minnesota, was cut into 2- by 2-cm squares with a scissors and with the aid of Teflon-tipped tweezers in a draught-free room.
- The surface of the silver foil rings was abraded and coated with a thin layer of freshly prepared silver epoxy, Eccobond 56C with Catalyst 11, Emerson and Cuming, Inc., Canton, Massachusetts.
- The electroformed mesh was rested on the coated silver ring, rough side toward the ring, and gently forced into the silver epoxy until epoxy came through the holes in the mesh. These parts were oven cured at 66°C for 4 hr. In this way, flat electroformed mesh surfaces could be prepared.
- Freshly mixed epoxy, Epon 828 with Curing Agent Z, Shell Chemical Co., New York, N. Y., was placed on the silver ring on the side opposite the mesh and on the end of the Pyrex cylinder. The two parts were joined and left overnight for a room-temperature cure. The seal was then oven cured at 66°C for 12 hr, and then at 110°C for 1 hr. This seal was thickened by adding more epoxy and repeating the given curing cycle. During the sealing, care was taken to prevent the applied epoxy from contacting and running into the silver mesh. The finished support is shown in Fig. 7d.
- In a few cases, expanded silver mesh, 4/0, 5 mils thick, was sealed to the external face of the finished support with silver epoxy around the edge to strengthen the support.

In the background of Fig. 7 are shown the glass vials, each individually scribed with coded marks, and silver powder (spheres) which were used in the experiments for building up the working electrode on the electroformed support.

Before an experiment, the electrode support shown in Fig. 7 was attached to the housing, and this assembly was attached to the hydrogen reference cell as shown in Figs. 8 and 9. Saunders S-22 Teflon Thread Sealant, Saunders Corporation,

Los Angeles, California, was used in this assembly. This 1/2-in.-wide TFE Teflon tape, shown in Fig. 8, is prepared according to U.S. Patent No. 3,002,770 and contains only unsintered TFE Teflon powder which has been extruded under pressure and calendered. The tape can be tightly wrapped around surfaces with finger pressure or by working with a spatula to seal to itself with enough strength for many laboratory operations.

A silver strip was spot welded to the end of the tab leading to the support, and this lead was coated with the Teflon tape as shown in Fig. 8. The cut surfaces of the housing and the Pyrex tube of the support were mated while the housing was clamped with its bottom end facing up. This joint was sealed with the Teflon tape, and the tab was wrapped to the housing. The working electrode was then clamped to the stand with its bottom end in a down position, and the reference cell was wrapped to the working electrode housing in two places as shown in Fig. 9. The tip of the Luggin capillary was placed about 0.7 mm from the electroformed mesh about 2 mm in from the rim. Care was required to prevent rupture of the mesh by the tip during this assembly. In Fig. 8, the neoprene rubber connections and the Teflon tape used in the assembly are shown on the stand. Two rings of Teflon tape were placed around the ground glass joint as shown in Figs. 8 and 9 to enable a good seal without the use of lubricant and to prevent the "freezing" of this joint. It was found necessary to construct the upper portion of the 3-mm-o.d. Pyrex plunger tube in the bellows with a solid Pyrex rod to impart the extra strength needed there.

3.2.4 Properties of Working Electrode Materials

The two important materials which constitute the electrode are the silver electroformed mesh, 2000 LPI, Ruling No. 2001, Buckbee Mears Co., St. Paul, Minnesota, and the silver spheres, Valley Metallurgical Processing Co., Haskell, New Jersey. These are the materials of (1) the bed support and the sphere bed which is a thin silver membrane with square holes, all about the same size and uniformly distributed, and (2) the sphere bed, composed of spheres which are all about the same size and which always

fall into a loose packing of about the same density. The accuracy of the analyses of the behavior of the electrode is largely contingent upon the accuracy of the characterization of these materials. In separate studies, characterizations of these materials were made.

In Figs. 10 through 16 are shown typical Polaroid photographs taken with the microscope used in measurements of the dimensions of the materials. The focal plane was adjusted to accommodate the measurements of most of the diameters or the side of the squares so that some portions of the photographs appear to be blurred. For example, the spheres shown in Figs. 13 through 16 are sharp only around most of the perimeters, and some particles appear to be joined because of the lack of proper focus for the perimeter of each particle and for the upper regions of every particle. Adjustments of the focal plane could be made to show that this "joining" is an illusion due to optical distortion or piling up of particles. The photographs serve to show the typical regularity of patterns encountred with these materials and to indicate the manner in which the microscope studies were made. Transmitted and reflected light were used in preparing the photomicrographs, and with the same settings the photomicrographs were taken of a calibrated reticle containing 200 divisions in 2 mm (i.e., 10μ per division). Diffraction patterns, present at the highest magnifications, are believed to cause negligible error. Approximately 240 random measurements were made of the diameters for each sphere fraction used and of the squares in the electroformed mesh. The results for the measurements with spheres are given in Table 1.

Table 1
RESULTS OF MICROSCOPIC MEASUREMENTS OF SPHERE DIAMETERS

Average Diameter (μ)	Average Deviation (μ)	Average Deviation (%)
13.65	2.36	17.3
37.65	4.21	12.3
54.31	3.78	6.96
86.49	8.04	9.3
156.1	12.8	8.2

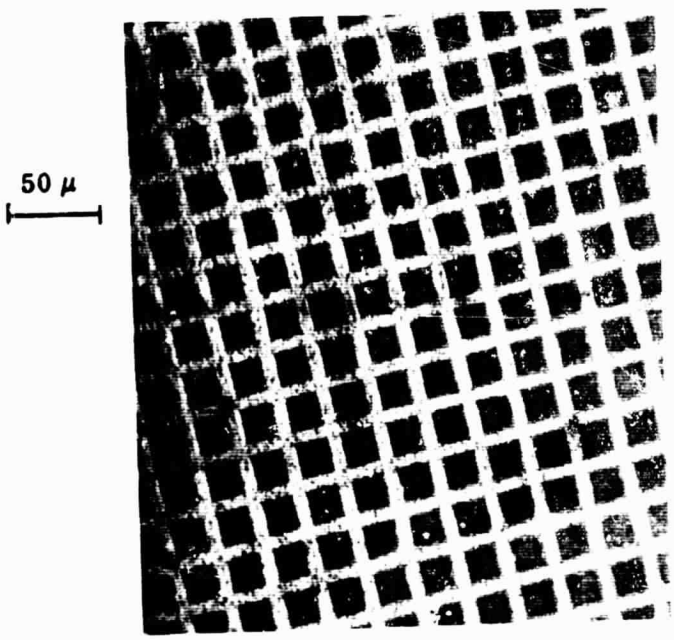

Fig. 10 Silver Electroformed Mesh, 1000 LPI, Smooth Side

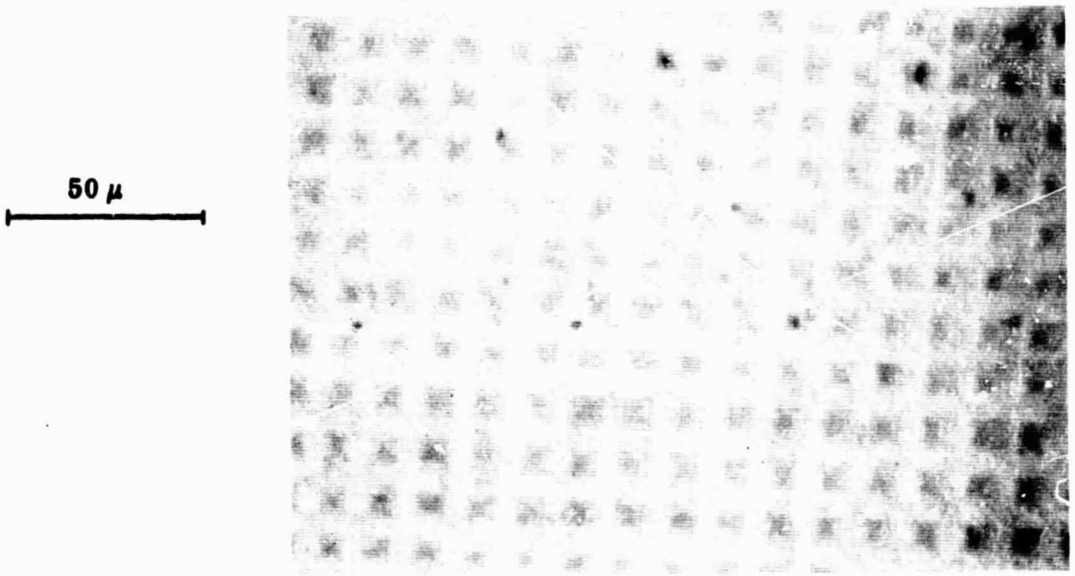

Fig.11 Silver Electroformed Mesh, 2000 LPI, Smooth Side

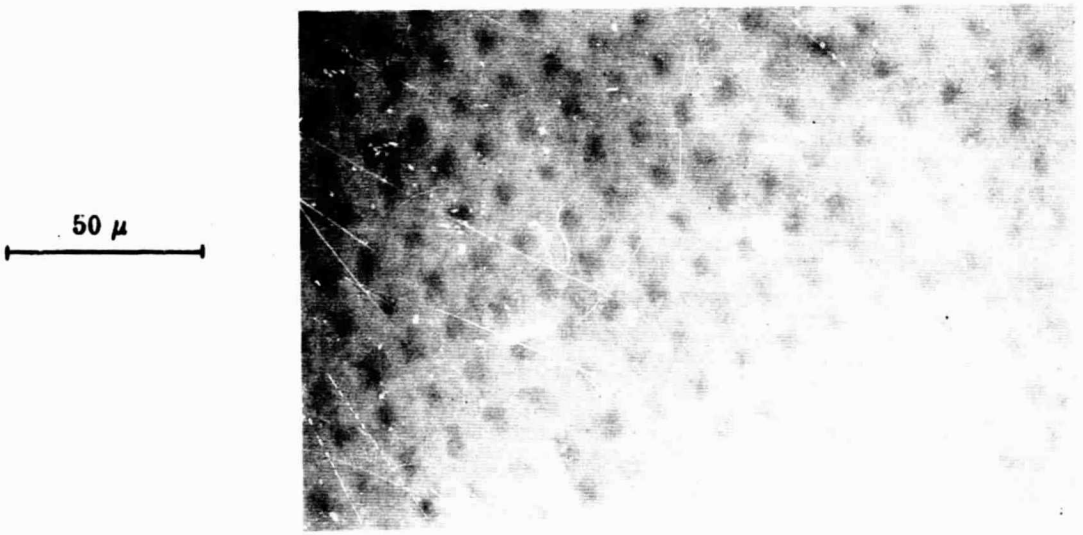

Fig. 12 Silver Electroformed Mesh, 2000 LPI, Rough Side

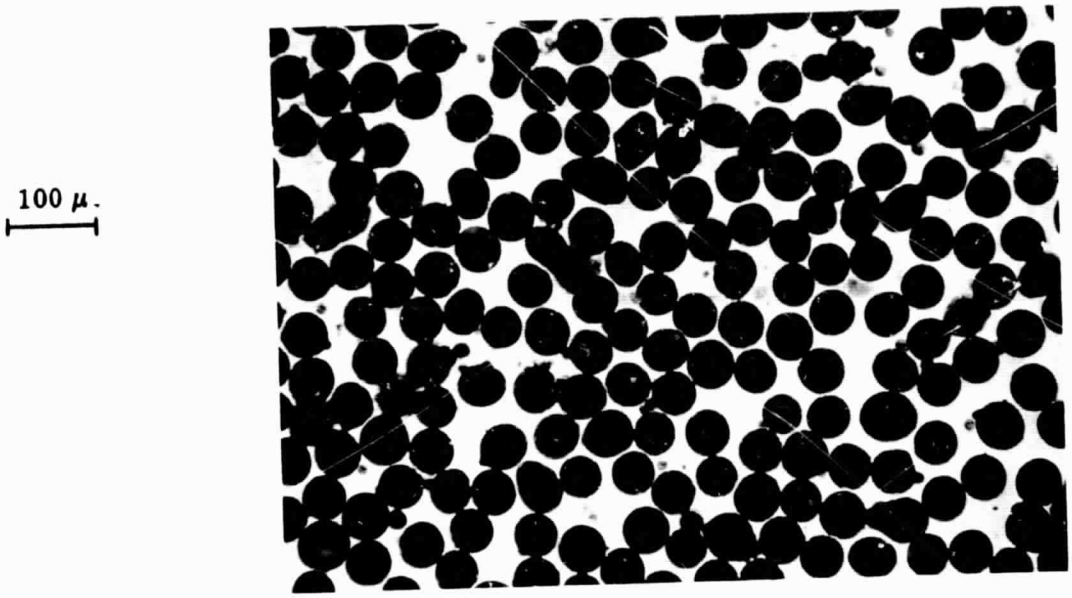

Fig. 13 Silver Spheres, 48-μ Average Diameter

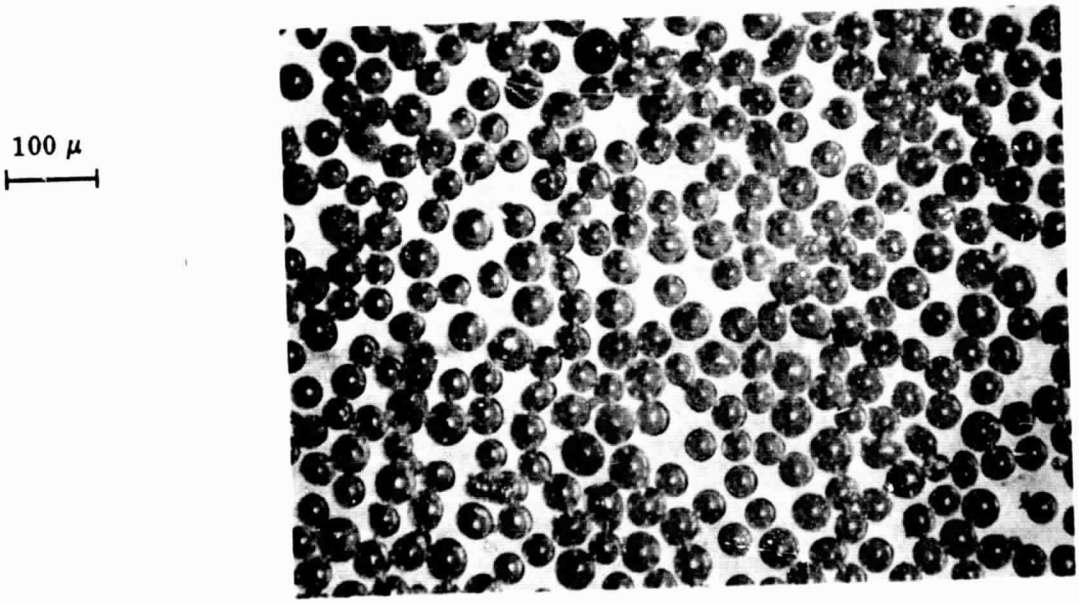

Fig. 14 Silver Spheres, 38-μ Average Diameter

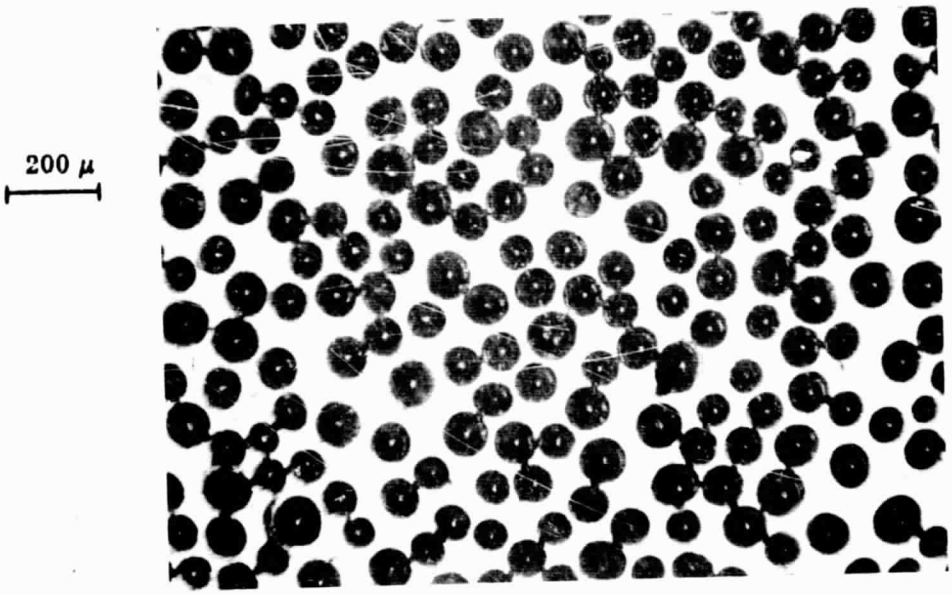

Fig. 15 Silver Spheres, 86-μ Average Diameter

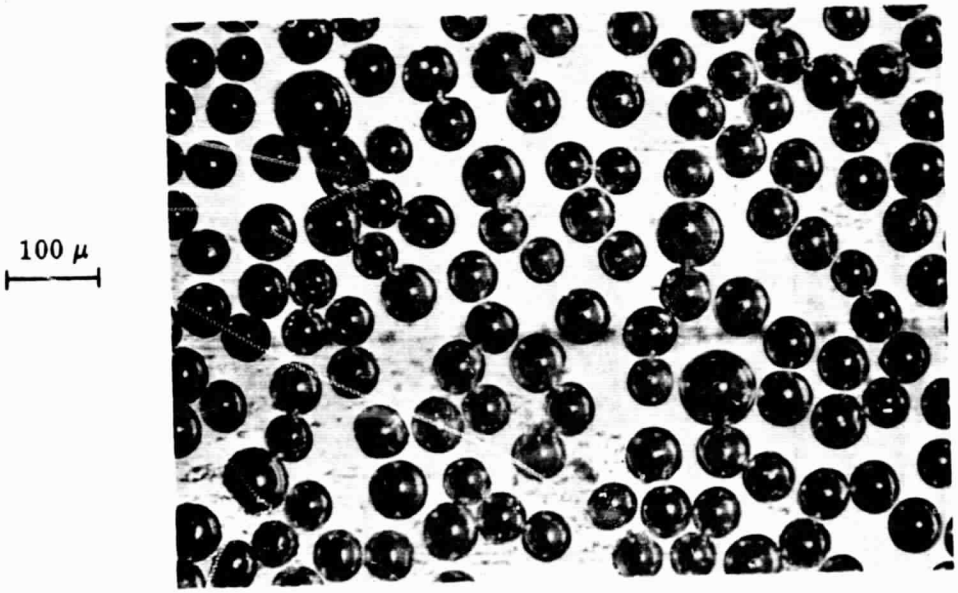

Fig. 16 Silver Spheres, 54-μ Average Diameter

The electroformed mesh used in most of this work was 4.2 μ thick, and a small amount of this material used in the catalyst distribution studies (Section 4) was thinner, about 3.0 μ. This difference was observed because of the variation in properties of the mesh from one piece to the next, each 4.5 by 4.5 in., when this material is purchased. Thickness was determined from photomicrographs of cross sections of the mesh, e.g., Fig. 17. The electroformed meshes have a smooth and a rough side (e.g., see Figs. 11 and 12), and the smooth-side square is generally larger than the rough-side square so that the hole may resemble a truncated pyramid. For most of the present studies, the side of the square on the rough side was 4.4 μ, the space between the squares on the rough side was 8.0 μ, and the side of the square on the smooth side was 6.7 μ. The average deviation from these average values is ± 6 percent, and the calculated transmission is 14.7 percent. The 2000 LPI electroformed mesh in Figs. 11 and 12 did not photograph well, so a photograph of a 1000 LPI mesh, Fig. 10, is included to show the typical uniformity of these electroformed structures. In these Polaroid photographs, occasional deviations from the regular patterns and shapes could be seen, but these were shown to account for less than a few percent of the total spheres or holes in the electrode. The observed regularity is remarkable in view of the estimated 8.2×10^5 square holes and the more than 10^8 spheres that are estimated to be present in one typical working electrode.

The ohmic resistance of the 2000 LPI silver electroformed mesh and the mesh-to-silver ring seal was determined with an impedance bridge, Type 1650-A, General Radio Company, Concord, Massachusetts. Specimens of the electroformed mesh were sealed with the silver epoxy on a circuit board to silver foil, and then the specimens were subjected to typical curing temperature cycle. By using different lengths of the same mesh between bonds, and from the known resistance of the leads, the resistance of the epoxy bond and mesh could be found. The ohmic resistance from side to side of a 1 by 1 cm piece of electroformed mesh is 0.013 ohms, and the contact resistance for the silver epoxy bond between the 2000 LPI mesh and a silver foil 0.12 cm wide and 1.00 cm long is 1.79×10^{-4} ohms. These resistances detract negligibly from the performance of the working electrode. During the experiments in 13.5 M KOH at

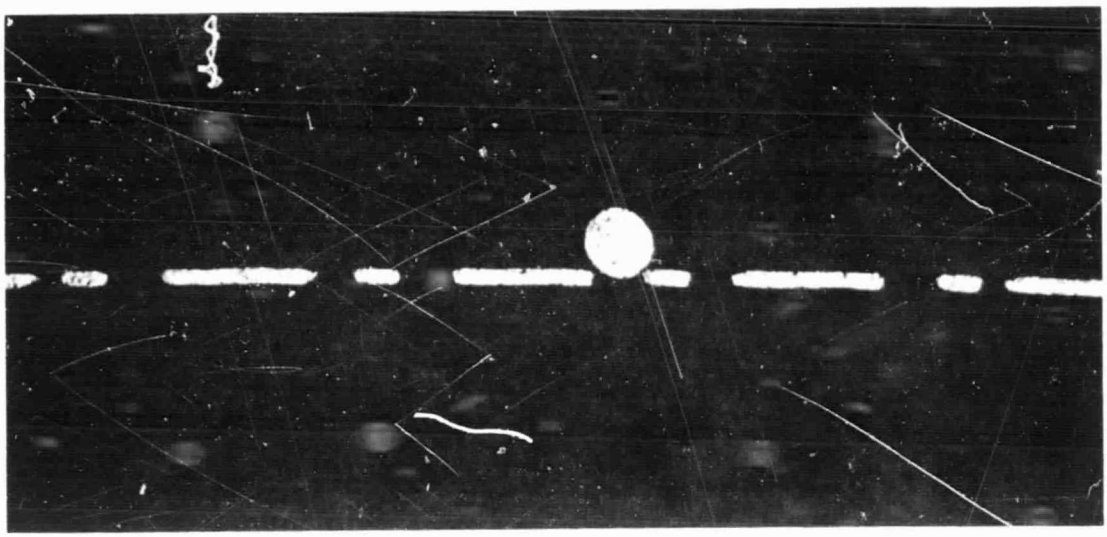

Fig. 17 Cross Section of Silver Sphere on Electroformed Mesh, 1000×

95°C, no attack was observed on the silver epoxy bond or on the Epon 828, Curing Agent Z material at the Pyrex-to-silver seal.

The pressure which causes bubbling from the electroformed mesh into 13.5 M KOH at 95°C was determined to be 76 and 53 cm of water head for the rough side (small opening) of the 2000 LPI mesh toward the oxygen gas and toward the electrolyte, respectively. This observation and the fact that the small openings present a more uniform structure to the spheres prompted the decision to conduct all experiments with the small opening toward the oxygen. The presence of fine silver spheres, 14μ in diameter, was found to increase the bubble pressure to values greater than 105 cm of water, the limit of measurement with the apparatus. This was caused by a partial flooding of the fine spheres at low subjected differential pressures. In Fig. 17 is shown a photomicrograph of a single sphere in contact with the mesh, which is approximately 3μ thick in this case. The extent of entry into the square hole by the $\sim$13μ sphere is shown, and contact of spheres with the intrinsic meniscus is seen to be possible for the smaller spheres if the differential pressure is sufficiently small.

Density and conductivity measurements of the purchased silver spheres were made by dropping the powder consisting of the spheres into a glass cuvette, 1.03 by 1.10 by 10 cm. The opposite sides of the cuvette contained freshly polished silver foils, 1.03 cm apart and 1.10 cm wide, and a depth of 0.5 to 1.0 cm was formed. The weight and volume of the powder were measured. Before these measurements and before each experiment, the powder was pretreated by boiling in 3 to 4 portions of concentrated ammonia for 1 hr, decanting each heated portion, washing in 4 portions of triply distilled water, rinsing in 3 portions of methanol, and air drying at 110°C for 1 hr. This pretreatment lowered the specific resistance, probably by the removal of an oxide film, but the specific resistance of the 14-μ spheres remained high. It was later determined that the spheres became bonded together in the electrode during operation as a cathode and that the specific resistance decreased to immeasurably small values (e.g., see section 4.12). With the exception of these 14-μ spheres the

specific resistances were low enough to be negligible before the experiments were conducted. The results of the conductivity and density measurements are given in Table 2. Included is the diameter of the largest sphere that can fit three spheres of the considered average sphere size which are in mutual contact. Repeated measurements of the loosely packed density of the spheres resulted in values deviating less than ±5 percent from the average value in Table 2.

Table 2

SOME PROPERTIES OF THE TESTED POWDER CONSISTING OF SILVER SPHERES

Average Diameter (μ)	Density (g/cm^3)	Fractional Void Volume	Specific Resistance (ohm-cm)	Smallest Spheres Fitting Through Pore, 0.155 D (μ)
156	6.23	0.407	0.41	24.2
86	6.25	0.405	5.3	13.4
54	6.23	0.407	0.39	8.41
38	6.22	0.408	8.3	5.83
14	5.59	0.468	50	2.11

The uniformity of the built-up thickness of the working electrode was also examined. After some experiments with the built-up electrode, the silver sphere bed was carefully removed by rupturing the membrane and the thickness of the bed was examined for uniformity. In another test of this uniformity, the entire electrode was encased in epoxy, after an experiment, and a photomicrograph was made of a section through the electrode. These examinations revealed that the overall thickness remained to within ± 2 percent of the average value and that the desired thicknesses were obtained to within about 10 percent with the assumption of the densities given in Table 2. In Fig. 18 is shown a cross section of an electrode having 54- and 14-μ spheres. The desired thicknesses were 1700 μ for the overall thickness and 400 μ for the fine layer. The observed overall and fine layer thicknesses were 1750 and 450 μ, respectively. A photomicrograph of the 156-μ spheres is shown in Fig. 19. Here, all the spheres were kept in the same plane by a special technique, and they appear

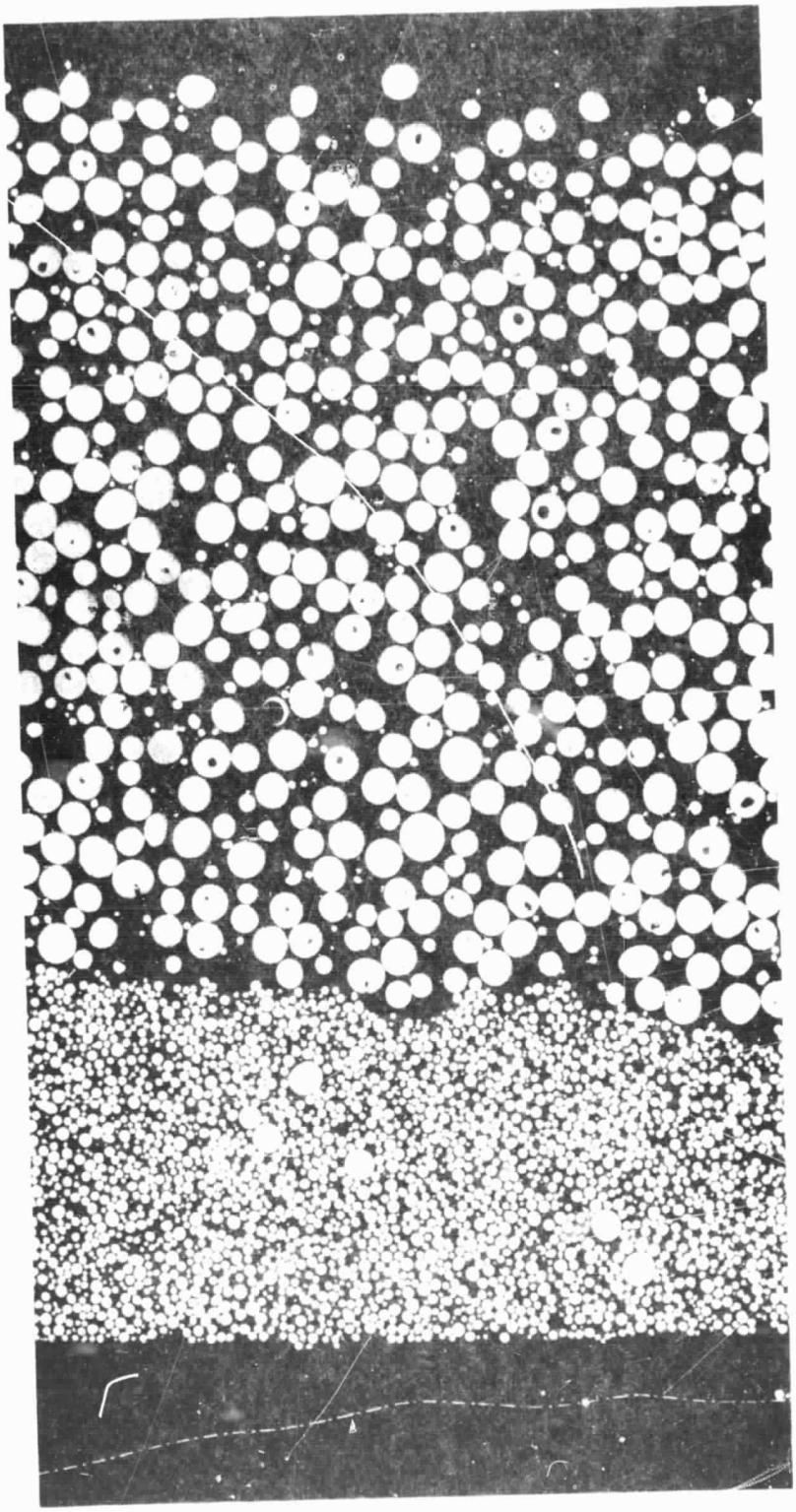

Fig. 18 Cross Section of Double-Porosity Electrode. 100×.
Fine Layer, 14-μ Spheres; Coarse Layer, 54-μ Spheres

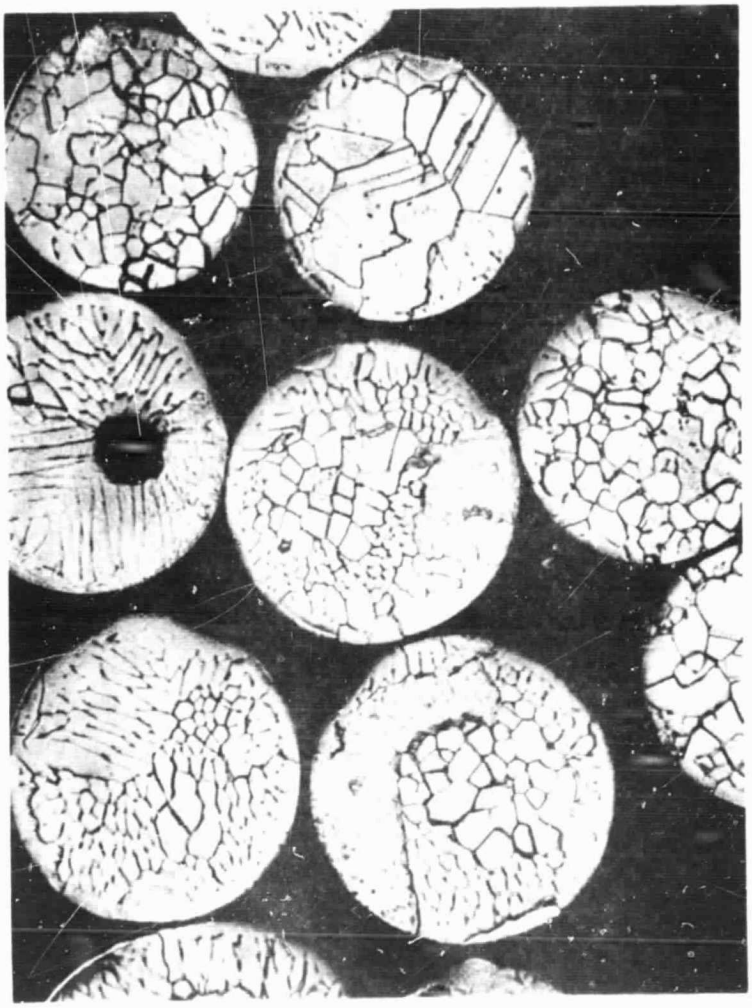

Fig. 19 Cross Section of Silver Spheres, 156-μ Average Diameter. 250×

to have the same diameter. In Fig. 18, with a random distribution, the spheres are sectioned at different locations through the spheres so that the spheres should not appear to be the same size. In Fig. 18, the fine electroformed mesh can be seen below the porous structure, where it became separated during the epoxy impregnation required for the metallurgical mounting.

The smallest spheres, 14 μ in diameter, could not be purchased in a narrow fraction, and they were separated from a 10- to 20-μ range by elutriation with nitrogen.

3.2.5 The Reference Electrode

In Figs. 6, 8, and 9, the arrangement of the utilized hydrogen reference electrode and cell are shown. A hydrogen stream of about 0.5 cc min^{-1} was passed over an immersed platinized platinum electrode which was in the same electrolyte as the working electrode to assure concentration and temperature uniformity. After immersion in the electrolyte, the reference cell was slowly filled with the bulk electrolyte through the Luggin capillary at the bottom of the cell by the hydrostatic pressure of the surrounding electrolyte. The cell was isolated from the bulk electrolyte with the exception of the capillary tube by the walls of the Pyrex reference cell which were partly wrapped with Teflon tape to minimize electrolyte contact with the Pyrex. The platinum foil of the electrode was platinized before each experiment (Ref. 14), washed in triply distilled water, and then introduced into the reference cell, as shown in Fig. 6. The platinum foil of the electrode was spot welded to a platinum wire sealed to the inside of a hollow Pyrex tube, and the wire led to the external electrical connection, as shown in Fig. 9.

3.2.6 Pressure and Flow Regulation

The oxygen pressure was kept constant at the gas side of the working electrode by employing a column of water with an inserted outlet tube as shown in Figs. 3 and 5. Bubbling from the immersed outlet tube was maintained and the depth of this

tube in the water column could be varied from 0 to 105 cm of water. The depth of immersion of the working electrode in the 13.5 M KOH was 7.0 cm, and this corresponds to approximately 10 cm of water head. This pressure must be subtracted from the applied oxygen pressure to obtain the differential pressure across the electrode. A needle valve at the oxygen tank and a throttling needle valve, Nuclear Products Co., Cleveland, Ohio, at the outlet tube leading to the flowmeter were used to adjust the oxygen pressure and flow. A calibrated displacement flowmeter was used at the oxygen outlet to indicate the flow which was maintained at 15 cc min^{-1} during the experiments.

The nitrogen and hydrogen flows were adjusted with needle valves at the tanks. All gases were standard items of purchase by the laboratory and were used without further purification. The gases were bubbled through water wash bottles before use to roughly indicate flow rates.

3.2.7 Counter Electrode

The counter electrode consisted of a platinum sheet, 4 by 5 by 0.1 cm, which rested on the bottom of the polypropylene bottle. Electrical connection to the counter-electrode was made from the top of the bottle by a platinum wire inserted in a Teflon sleeve. Oxygen gas which developed at the counter electrode did not appear to affect the results, even at the highest current, 100 mA.

3.2.8 Monitoring the Electrode Response

Monitoring of the electrode response was according to the circuit shown in Fig. 4. The applied current, cathodic at the mesh, was held galvanostatically with an Electronics Measurement, Inc., Eatontown, N. J., constant current power supply. A Model MR Sargent recorder, E. H. Sargent & Co., Chicago, Ill., and a model 500 Greibach ammeter, Greibach Instruments Corp., New Rochelle, N. Y., were used to monitor the potentials and currents. In addition, a Model 2700 Rubicon potentiometer, Rubicon Instruments, Philadelphia, Pa., served to check the values of the Sargent recorder.

3.2.9 Solutions

The 13.5 M KOH solution used in these experiments was prepared in 7-liter quantities with reagent-grade potassium hydroxide which contains 2.0 percent potassium carbonate. Triply distilled water was used, the last two stages from quartz vessels. The solution was stored in a polyethylene bottle before use, and titrations were made to assure a KOH concentration of 13.5 ± 0.1 M. The 13.5 M KOH solution in the electrolyte cell was changed after three experiments or after a 1-week residence in the cell, depending on which occurred first. In the cell, nitrogen was bubbled from a fine Teflon tube at the bottom for at least 12 hr prior to an experiment.

3.3 PROCEDURE

The procedures for the general assembly of the apparatus, cell, working, and reference electrodes are given in the preceding sections. The general conduct of an experiment is given here, together with some catalysis treatments of the silver spheres used in a few special experiments.

3.3.1 Performing an Experiment

At the start of an experiment the oxygen valve at the tank was opened, the oxygen throttling valve was closed, and the connections of the oxygen lines were made to the electrode housing shown in Fig. 9. The electrode housing, together with the reference cell, was lowered a few centimeters into the electrolyte until 35 cm of water head of applied oxygen pressure developed, usually within a few minutes. This procedure kept the gas-side cavity of the working electrode free of bulk electrolyte, and the intrinsic meniscus remained positioned at the mesh. The housing was then lowered and clamped into position so that the housing tube was vertical and the mesh was 7.0 cm below the electrolyte level (e.g., see Fig. 5). The oxygen flow past the electrode was adjusted to 15 cc min^{-1}. The hydrogen was turned on, and the line was purged and then connected to the reference cell. The reference electrode was

platinized and added to the reference cell. The thermostating bath was then filled with water, the heating system and stirrer were turned on, the makeup water bottle was attached, and the polypropylene spheres were added to the water to reduce evaporation.

A period of 3 to 4 hr was then required before the rest potential was finally attained. The operating temperature was attained in less than 1 hr, but the slow attainment of a rest potential could not be hastened with applied cathodic or anodic current pulses. The rest potential was usually 1035 mV versus the hydrogen reference electrode, although values of 980 to 1055 were sometimes obtained. At room temperature in 6.9 M KOH, the rest potential is obtained more quickly, within 30 min. During this waiting period, a weighing schedule was usually followed to weigh out planned amounts of spheres to be added.

At an applied oxygen pressure of 35 cm of water, the electrode was built up, and the scheduled experiments were conducted with variations in applied oxygen pressure and current. After each addition of spheres to the trap door, at least 15 min were allowed for temperature attainment by the spheres. After each addition of the spheres to the mesh and after each current or applied pressure change, the potential was observed on the Sargent MR recorder until the potential reached a steady value. This attainment of a steady potential took from 10 min to 1 to 2 hr, depending on the type of change (e.g., see section 4.13). A potential was considered to have a steady state value when no detectable change occurred in a 6-min period. The limit of detection was ± 1 mV.

3.3.2 Catalysis Treatments

Platinum metal was added to silver or nickel spheres by chemical displacement by treating these metals with a chloroplatinic acid solution. A 100-ml quantity of this solution was prepared to a concentration equivalent to 9.66 mg of platinum metal per milliliter. This concentration was determined gravimetrically by precipitating platinum metal with hydrazine from a known volume of solution. The silver and nickel spheres were treated with the platinum solution before they were added to

the electrode bed. The silver spheres were treated according to the following procedure:

- Wash spheres 4 times in concentrated aqueous ammonia.
- Rinse spheres in triply distilled water 6 times.
- Add 50 ml of triply distilled water to a 2-g portion of spheres.
- Dilute the required volume of the standardized chloroplatinic acid solution with 50 ml of water, and add this solution gradually to the agitated slurry of spheres.
- Bring solution to a boil, decant, add triply distilled water, boil, and decant.
- Wash spheres with 2 portions of triply distilled water.
- Wash spheres with 4 portions of concentrated aqueous ammonia with heating.
- Wash spheres in about 10 portions of triply distilled water.
- Dry spheres in air at 110°C for 2 hr.

The specific resistance of the 156-μ silver spheres treated in this way was lowered from 0.41 ohm-cm for the untreated spheres to values less than 0.25 ohm-cm.

Nickel spheres having an average diameter of approximately 156 μ, corresponding to a -80 + 100 sieve fraction, were obtained from Federal-Mogul Division of Federal-Mogul-Bower Bearings, Inc., Ann Arbor, Mich. The nickel spheres were treated in the following way:

- Wash in 3 portions of acetone.
- Wash in 4 portions of triply distilled water.
- Add 30 ml of 1 part concentrated nitric acid diluted with 2 parts of water to 2.4 g of nickel spheres. Stir for 3 min.
- Decant acid wash with 4 portions of triply distilled water.
- Add 50 ml of triply distilled water.
- Dilute the required volume of the standardized chloroplatinic acid solution with 50 ml of water, and add this solution gradually to the agitated slurry of spheres.
- Bring solution to a boil with constant agitation, decant, add triply distilled water, boil, and decant.

- Wash spheres with 4 portions of triply distilled water.
- Dry spheres in air at 110°C for 2 hr.

The specific resistance of nickel spheres, 156 μ in diameter, which were treated with nitric acid according to steps 1 through 4 above and which were dried was 1.3×10^5 ohm cm. After treatment with chloroplatinic acid, the specific resistance was reduced, depending on the platinum loading for a 1300-μ-thick layer in the 1.25 cm^2 electrode. For a 10, 3, 1, and 0.3 mg platinum loading, the specific resistances were 1.9, 7.0, 10.9, and 308 ohm-cm, respectively. It was decided to use the nickel sphere bed having the lowest specific resistance in the experiment (Section 4). The density and fractional void volumes of the nickel sphere bed were 4.66 g cm^{-3} and 0.476, respectively.

Gold plating of the 156-μ silver spheres was accomplished by resting the spheres on a horizontal gold cathode which was constantly vibrated with a tool normally used to inscribe metals. A cyanide-free proprietary bath was used which advertises a dense, pure gold deposit. From the coulombs passed and the area of the spheres, it is estimated that a 1-μ-thick layer of gold was deposited. The specific resistance of the gold-plated silver spheres was 0.05 ohm-cm. The surface of the spheres appeared to be continuous and unchanged after use in an oxygen cathode.

Teflon loading of platinized silver spheres was done by adding dry, fine Teflon TFE powder to a 1-g quantity of the spheres and dispersing the Teflon powder throughout the spheres by gently shaking the mixture in a small glass bottle. For further dilution of the Teflon, a small quantity of this mixture was then added to a fresh quantity of platinized silver spheres. The presence of Teflon in the sphere mixture was detected by measuring the specific resistance. For a Teflon loading of 17 mg of Teflon for a 1300-μ-thick bed in the 1.25 cm^2 electrode, the specific resistance was in excess of 10^6 ohm-cm. For a Teflon loading of 4.4×10^{-3} mg in the same volume of platinized, 156-μ silver spheres, the specific resistance was 1.14 ohm-cm, still greater than for the un-Teflonized spheres, 0.25 ohm-cm. Teflon TFE powder with an advertised 1-μ average particle size was used, TL-120 from Liquid Nitrogen Processing Corporation, Malvern, Pa.

Section 4
EXPERIMENTAL RESULTS AND DISCUSSION

The principal advantage of the described apparatus is its capability of quickly building up a number of different electrodes with predetermined structures, catalyst, or pore size distribution. This eliminates timely and tedious fabrications and tests with fuel cell stations, and it enables a consistent evaluation by a self-comparison of results. The hazard is in collection of an overwhelming amount of data in an unsystematic fashion which can suffocate interpretation. Without an accurate knowledge of the effect of the variables, it appears best to proceed with a few probe experiments which could furnish the basis of subsequent experiments. In this section, an attempt is made to give the results and some discussion for "probe" experiments, and in a few cases, at least, it is believed that the results lead to a reasonably clear understanding of these variables, e.g., as with differential pressure and effective pore diameter.

Measurements were made galvanostatically with the system at steady state, i.e., with no change in potential (± 1 mV) in a minimum of 6 min, at 95°C in 13.5 M KOH. Between measurements of potential, changes were made in applied current, differential pressure across the bed, sphere size, and bed thickness. The effect of bed thickness was examined for 14-, 38-, 54-, 87-, and 156-μ-diameter spheres in single-porosity electrodes, and the effect of differential pressure was examined for 156-μ-diameter spheres in single-porosity electrodes and in double-porosity electrodes with 14- and 38-μ-diameter spheres in the fine layer and with the fine layer on the liquid side. Differential pressure was varied from a minimum of 5 to about 100 cm of water. Other experiments were conducted in which the effect was determined of platinum, chemically deposited on silver and nickel spheres; of Teflon loading with 1-μ Teflon particles; and of gold used as an oxygen catalyst. In this section, electrode potentials are referred to the hydrogen reference electrode in the same solution. Cathodic currents are referred to the facial area of the electrode at 1.25 cm^2.

4.1 PRELIMINARY EXPERIMENTS

4.1.1 Comparison With Past Work

To assure the proper relation to previously conducted work (Refs. 12 and 13), some results were obtained with the present apparatus under the same conditions of the past work, i.e., in 6.9 M KOH at 21.8°C and 57 cm of water differential pressure. The main difference of the present apparatus is that it has a 2000 LPI silver mesh instead of the 1000 LPI mesh previously used. In addition, the present electrode housing is constructed differently so that the oxygen flows horizontally past the electrode at a distance of 1.5 cm with less impingement on the electrode. The near accord in the current-potential curves of the past and present apparatus, shown in Figs. 20 and 21, is considered good enough for meaningful comparisons in the future. With a 3000-μ-thick layer of 156-μ spheres, there is no appreciable difference in performance, as shown in Fig. 21. No further experiments were done at 21.8°C and in 6.9 M KOH.

4.1.2 Pressure Variation With Electroformed Meshes

In Fig. 22 are given typical plots obtained from measurements of the oxygen electrode potential at different applied cathodic currents. Data are given for three electroformed meshes available from the Buckbee Mears Co: 2000, 1500, and 1000 LPI. Open-circuit potentials were usually at 1035 mV with these silver meshes. Added to Fig. 22 is the current-potential curve obtained with an electroformed mesh at room temperature and in 6.9 M KOH. It can be seen that improvement in performance results in raising the temperature to 95°C and in increasing the concentration to 13.5 M KOH. These performances with the electroformed meshes are surprising if it is considered that the facial area of the circular electrode is only 1.25 cm^2 and that the electrode thickness is only a few microns. Some of the determined and calculated physical parameters of the meshes are given in Table 3. The estimated area available for supermeniscus film formation is less than 2 cm^2.

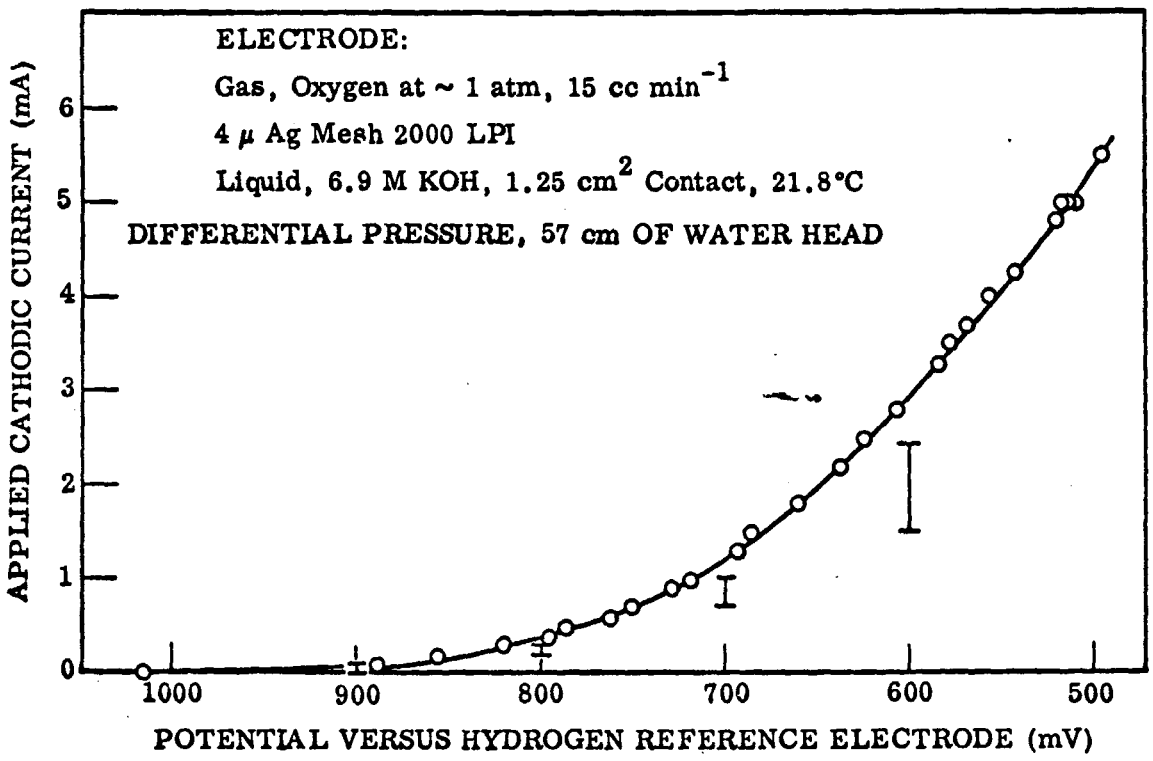

Fig. 20 2000 LPI Silver Electroformed Mesh as an Oxygen Electrode. Wide lines represent results under NOw-64-0597-f with 1000 silver mesh

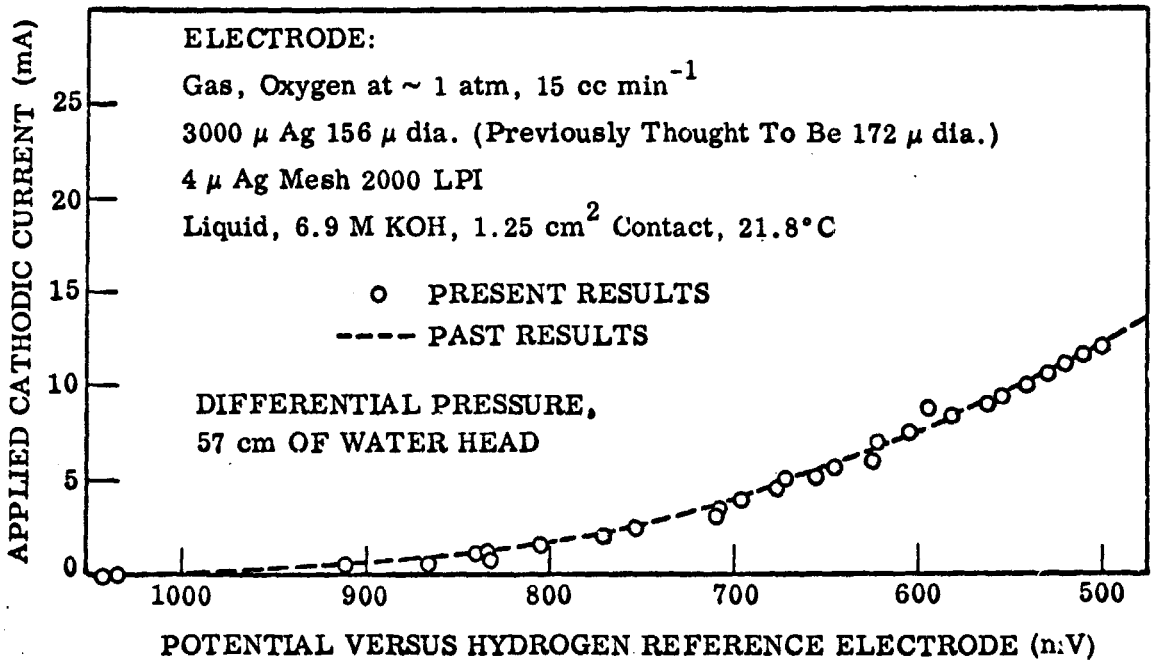

Fig. 21 Comparison of Past and Present Results With Silver Sphere Bed Oxygen Electrode

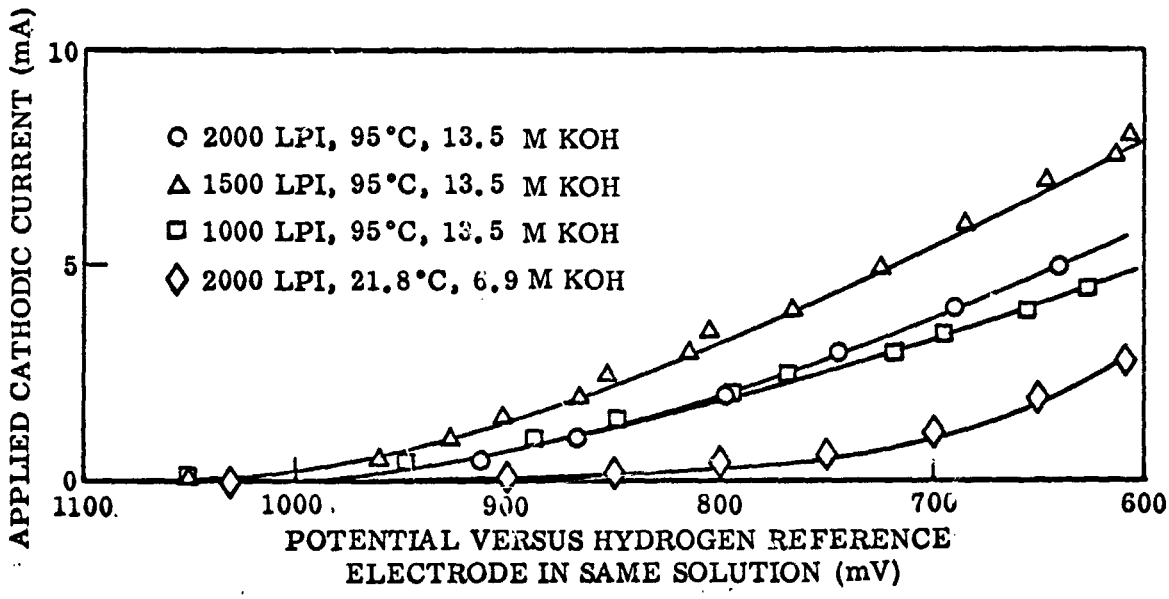

Fig. 22 Typical Behavior of Silver Electroformed Meshes as Oxygen Electrodes Under Cathodic Load. Oxygen Differential Pressure, 25 cm of Water for Results at 95°C, and 57 cm for Results at 21.8°C

Table 3

ESTIMATED PROPERTIES OF THE THREE SILVER ELECTROFORMED MESHES

Estimated or Determined Physical Parameter	Identifying Silver Mesh Number		
	2000 LPI	1500 LPI	1000 LPI
Facial Area of Circle (cm^2)	1.246	1.246	1.246
Side of Square Hole on Gas Side (μ)	4.36	7.14	14.5
Mesh Thickness (μ)	4.15	4.83	5.75
Area of Planar Surface of Gas Side Subtracting Square Hole Openings (cm^2)	1.092	1.018	0.859
Area on Sides of Square Holes (cm^2)	0.750	0.794	0.733
Total Area Available to Supermeniscus Film Assuming Intrinsic Meniscus at Liquid Side (cm^2)	1.84	1.81	1.59
Number of Holes in Electrode	8.2×10^5	4.5×10^5	1.9×10^5
Perimeter Length at Liquid Side (cm)	2600	1700	840
Supermeniscus Film Length Assuming Positioning of Intrinsic Meniscus at Liquid Side (μ)	8.15	9.60	11.30
Current Obtained at 0.4 V Polarization (mA)	5	6.5	4.5
Bubbling Pressure (cm of H_2O)	76	60	57

The only physical parameter in Table 3 which is in direct accord with the observed behavior is the area on the sides of the square hole in the electroformed mesh. The 1500 LPI electrode with the most hole area gives the best performance, and so forth. It is possible that the 1500 LPI mesh, with approximately the same total area available for film formation as the 2000 LPI mesh, actually has more film area available because of partial capillary flooding of the holes in the 2000 LPI mesh; e.g., compare the experimentally determined bubble pressures given in Table 3. No definite conclusions on this difference in performances for the three meshes are made at present, however, and only the magnitude is noted of the possible contribution by the mesh to the performance of an unflooded, built-up electrode structure.

In Fig. 23, the effect of pressure variation is shown. The cathodic current was maintained at 2.0 mA as the oxygen pressure applied to the gas side was decreased. The performance changed only slightly, by less than about 30 mV, until the flooding pressure was approached, i.e., 2.5 cm of water head. As the differential pressure across the electrode approached zero, flooding started and the performance was lost as the electrode became submerged in the electrolyte. This is normal behavior, since the overall process then becomes diffusion limited, i.e., limited by oxygen diffusion through bulk electrolyte. This behavior may be considered as evidence that reducible impurities are not present in the electrolyte whose performance at the cathode is observed instead of that of oxygen. Oxygen is thus shown to be needed to sustain the higher performances of the electrode, as shown in Fig. 22, and this effective exclusion of oxygen by flooding causes extremely poor performance, e.g., typically found to be less than 100 μA at 0.5 V. If the electroformed mesh should become flooded in the operation of a built-up double-porosity electrode, for example, it may be assumed that the electroformed mesh contributes negligibly to electrode performance. This deterioration in oxygen electrode performance with total flooding was also observed with the built-up electrodes.

The information shown in Fig. 23 serves as evidence that assures the experimeter that the intrinsic meniscus is positioned in the holes or near the liquid side of all the holes. If large changes in potential had occurred with small pressure variations at the higher differential pressures, a nonuniformity in the hole sizes would be suspected. The opposite is observed. There is little change in potential over the range of 2.5 to 25 cm of water differential pressures. Also, if the intrinsic meniscus were not fixed in or at the liquid side of the holes, but at the gas side of the holes, small pressure reductions would cause a substantial change of the area available to the supermeniscus film, and a large loss in performance would be expected, e.g., as with differential pressures less than 2.5 cm of water. From the given potential dependence in Fig. 23 and from the known geometry of the mesh, it is natural to assume that the intrinsic meniscus resides in the square hole near the liquid side at 25 cm of water head, moves closer to the gas side when the pressure is reduced to 2.5 cm of water head, and starts to cover the gas side of the mesh for pressures below 2.5 cm of water head.

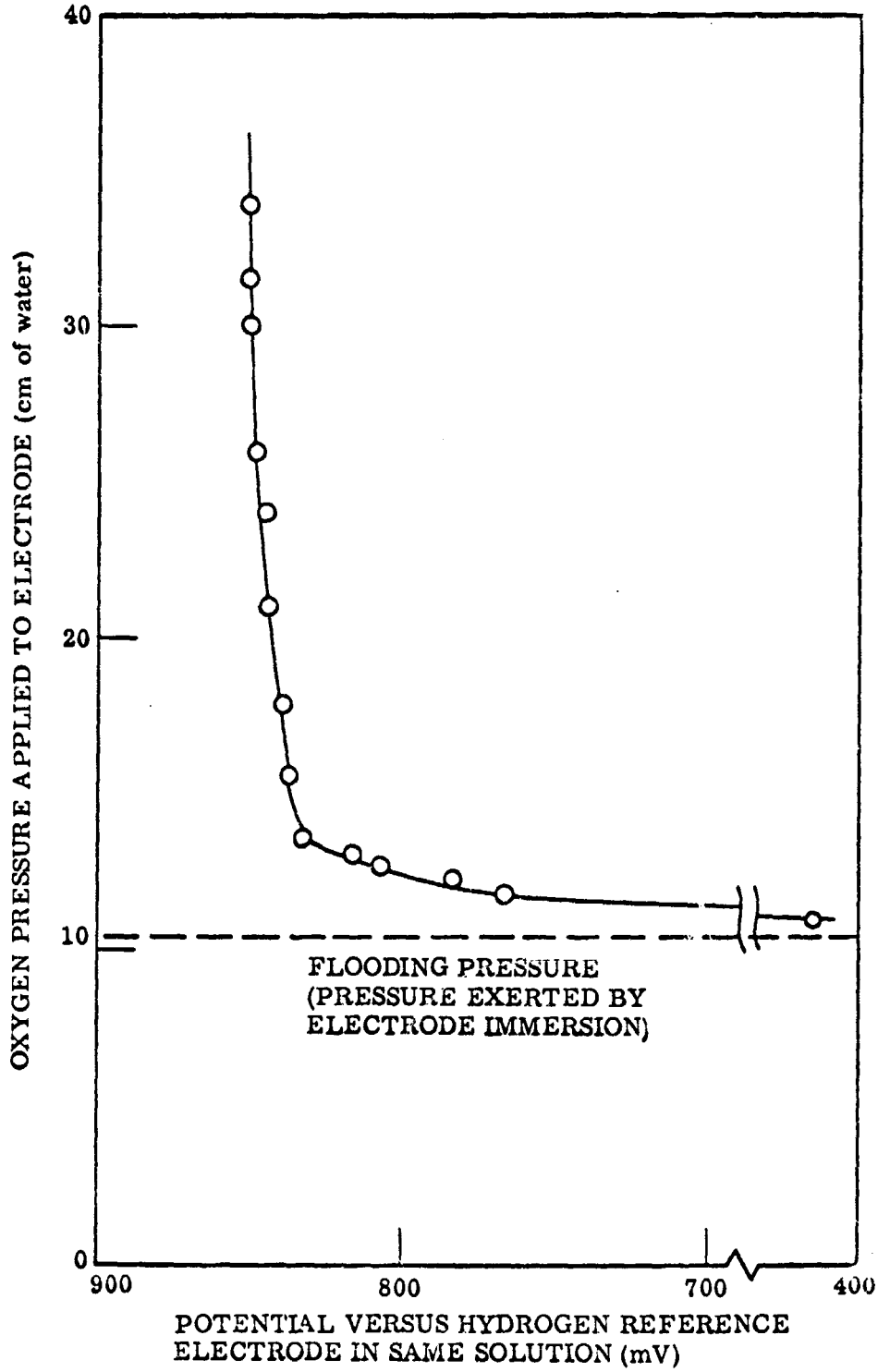

Fig. 23 Effect of Reducing Applied Oxygen Pressure on Oxygen Electrode Performance. 2000 LPI Silver Mesh, 2 mA

When the pressure was increased to its highest value – about 24 cm of water head – at any time from a lower pressure at which flooding did not occur, the original potential versus the hydrogen reference cell was again obtained. This occurred by a direct and monotonic approach to the original potential with the passage of time within 3 to 4 min, and no overshoot was observed. If, however, the electrode was permitted to flood for a few minutes before the pressure was again increased to 24 cm of water head, the potential quickly obtained a value closer to the oxygen open-circuit potential, and then it approached the original value of the potential from the opposite direction, as shown in Fig. 24. This may be due to the formation of intermediate species at the electrode during the severe polarization (Ref. 15), or it may be due to the improvement in performance caused by a very slight thickening of the supermeniscus film. A small amount of film thickening, not large enough to cause oxygen diffusion limitations, should lower the resistance to transport from the regions in the film, where electrochemical reaction occurs, to the bulk electrolyte region (Ref. 16), and assure effective film continuity around the edge of the square holes.

4.1.3 Flow-by Variation

With the given system, no effect was observed when oxygen flow was varied from 2 to 50 cc min^{-1} through the electrode housing. The oxygen passes by the dead-ended chamber containing the electroformed mesh and built-up electrode, about 1.5 cm above the mesh, and does not appreciably disturb the gas in this chamber. Gas phase transport of oxygen from the oxygen stream to the mesh in this chamber can be shown to be rapid and not limiting for the overall transport and electrochemical processes during electrode operation by considerations of Fick's first law.

4.2 EFFECT OF DIFFERENTIAL PRESSURE

In studies of gas electrode behavior at various differential pressures, recently reported results have indicated that the value of the differential oxygen pressure across the electrode and the history of subjection to this differential pressure are more important

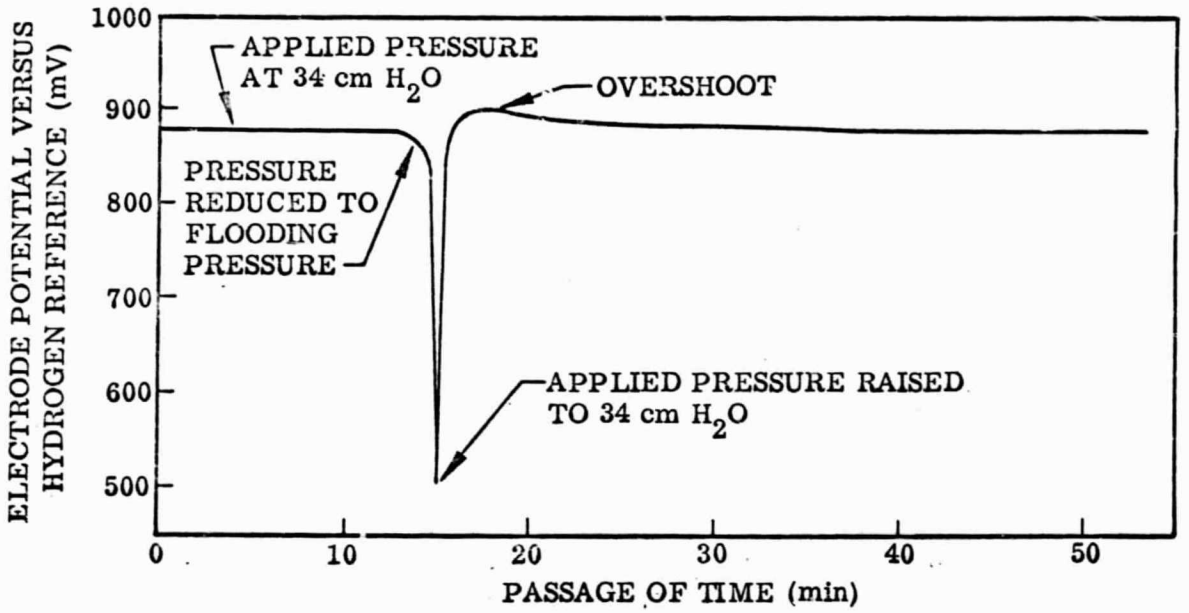

Fig. 24 Appearance of an Overshoot After Flooding 1000 LPI Silver Mesh. 1 mA Cathodic Current

in evaluations of electrode performance than indicated by first considerations of bubble pressure tests alone (Refs. 17 through 22). It was observed that a hysteresis occurs in the current-pressure curve and that an optimum differential pressures exists, i.e., a differential pressure at which the performance of the electrode is maximized. Although these effects may not always be observed in "practical" electrodes, which have a wide pore size distribution or roughened surfaces on the pore walls, they provide a key to understanding the operation of a gas electrode when simple systems are used, for both wet-proofed and double-porosity structures, and they are intimately connected with the role of structure in influencing electrode performance. The variation of differential pressure and the interpretation of the effects of this variation are thus included as a part of the tests on built-up electrodes.

A single-porosity electrode was built up to 1700-μ thickness with the 156-μ-diameter silver spheres at 25 cm of water differential pressure (subtracting 1.0 cm of water from the applied oxygen pressure for the depth of electrode immersion). The differential pressure was first reduced in steps to 5 cm of water and then increased to about 80 cm of water. At 5 cm of water in the absence of spheres, flooding of the gas side of the mesh would be minimal (Fig. 23). In the presence of spheres, however, flooding could occur at the mesh and in the sphere bed, depending on the capillary forces exerted by the sphere bed and the extent of flooding of the sphere bed, i.e., via a supermeniscus film extending from the bulk electrolyte (Section 5). The intrinsic meniscus may not have contacted the bottoms of the spheres which happened to rest on a square hole of the mesh, at least at open circuit (Ref. 23). A simple formula can be derived which relates sphere radius R and the side of the square L to the depth h which the sphere extends into the square hole of the mesh:

$$h = R - \left(R^2 - \frac{L^2}{4}\right)^{1/2}$$

For the 156-μ spheres and 2000 LPI mesh, h is 0.03 μ which may be compared with the mesh thickness, 4.15 μ. Nevertheless, spheres still may contact electrolyte through a supermeniscus film (Section 5).

At each differential pressure, a current-potential curve was obtained so that a series of such curves was available for analysis. In Fig. 25 is shown a typical current-potential curve taken near the optimum pressure after the pressure was increased.

Isopotential plots were then made, from the series of current-potential plots, of current versus pressure as shown in Figs. 26 and 27 to assist interpretations of the effect of differential pressure. The hysteresis effect which occurs with decreasing and increasing differential pressure can be clearly seen in Figs. 26 and 27. In Fig. 27, this effect is shown for a working electrode potential of 500 mV for both decreasing and increasing pressure. There is an optimum differential pressure which does not change as the applied current (or potential) is changed, but which is shifted together with the entire curve depending on whether the differential pressure has previously been decreased or increased (i.e., depending on whether the electrolyte has been infiltrating the sphere bed or has been draining from the sphere bed). The current peak at the optimum pressure was reproducible for increasing pressure, about 50 ± 2 mA cm^{-2} at 42 cm of water, but varied between 25 and 45 mA cm^{-2} for the initially obtained decreasing pressure curve at 500 mV. The values of the optimum pressures for both decreasing and increasing pressure were reproducible to within the limits of the experiment, ± 1 cm of water. Current densities were about 27 mA cm^{-2} at 500 mV when the electrodes were first built up at 25 cm of water differential pressure with the 156-μ spheres (Fig. 26).

The behavior described appears to be related to the characteristic hysteresis of liquid holdup in a porous medium as a function of differential pressure across the medium; i.e., porous beds require a higher differential pressure to attain a given saturation during forced drainage than during liquid infiltration (Ref. 4). The shift in the optimum differential pressure shown in Fig. 27 suggests that this optimum is connected with a certain electrolyte content in the porous bed. If electrolyte films on the spheres are present in the absence of penetration of electrolyte into the bed, the greatest film area and the most favorable gas transport condition through the film exists with minimum liquid penetration. However, the resistance to ionic transport in these

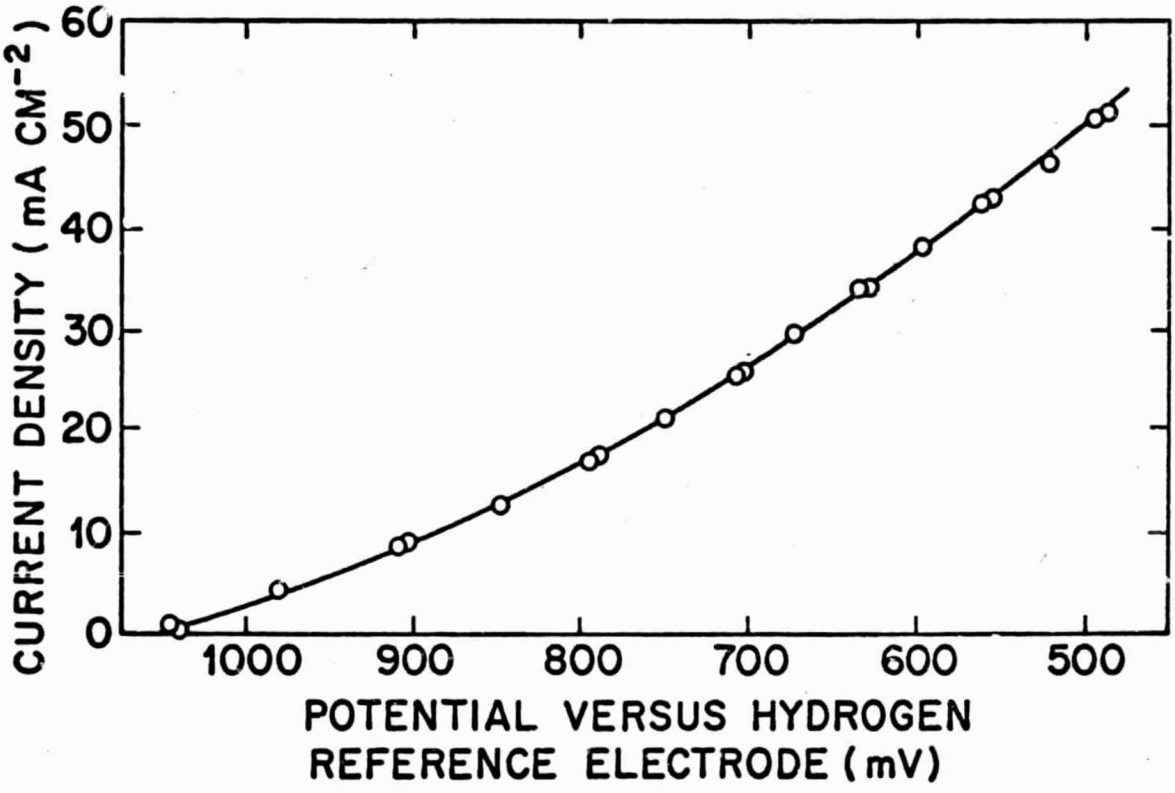

Fig. 25 Typical Current-Potential Relation Obtained for One Set of Conditions: Single-Porosity Bed of 156-μ Silver Spheres, 1700 μ Thick, at Differential Oxygen Pressure of 40 cm of Water After Differential Oxygen Pressure Increased From 5 cm of Water

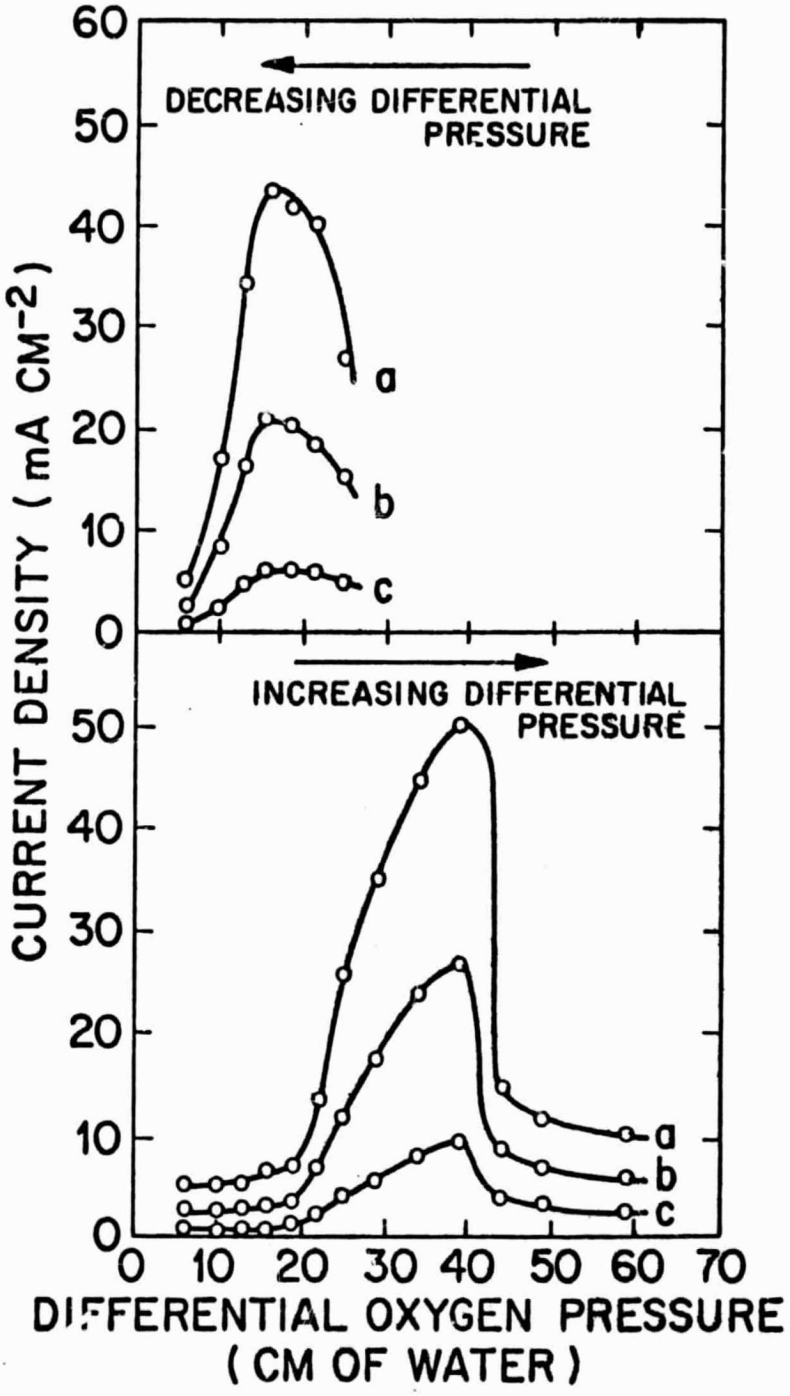

Fig. 26 Effect of Differential Pressure Variation on Silver Sphere Bed Electrode. Single-Porosity Bed of 156-μ Silver Spheres, 1700 μ Thick, at Three Potentials Versus Hydrogen Reference Electrode: a. 500, b. 700, c. 900 mV

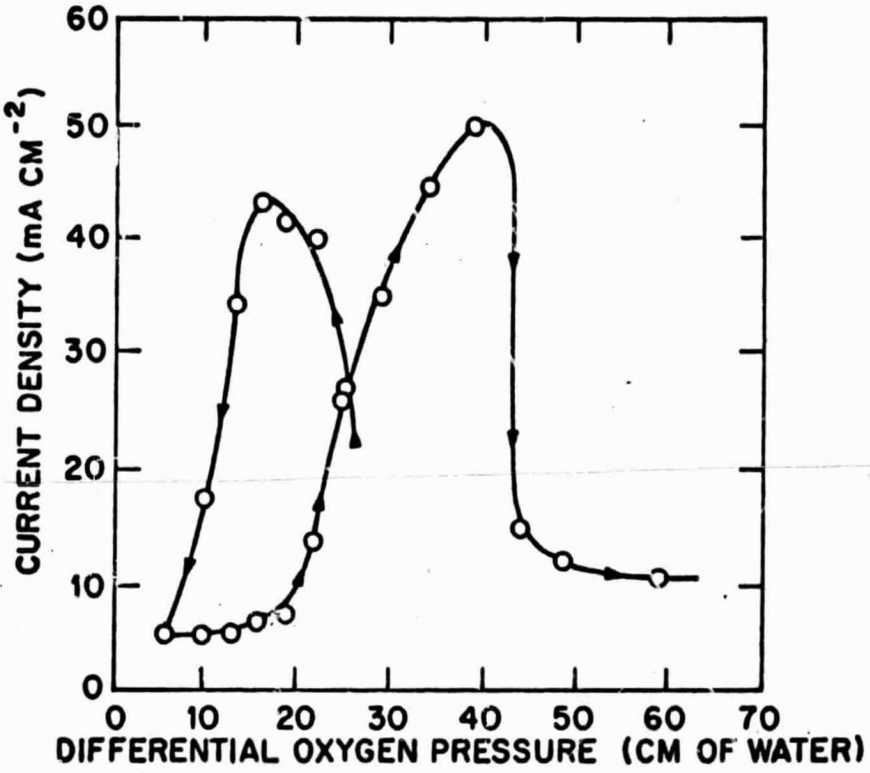

Fig. 27 Hysteresis When Differential Pressure Is Changed. Single-Porosity Bed of 156-μ Silver Spheres, 1700 μ Thick, at 500 mV Versus Hydrogen Reference Electrode

thin films renders them ineffective at any significant distance from the bulk electrolyte. If liquid that penetrates the bed forms continuous paths or filaments connecting regions of film to the bulk electrolyte, the penetration of this liquid can be expected to enhance electrode performance. However, if liquid penetrates in an amount or in a configuration to eliminate major fractions of the film surface, then this penetration degrades performance.

The appearance of an optimum can then be explained as follows: At pressures below the optimum value, excessive flooding of the bed's film areas occurs. At pressures above the optimum value, the filaments of electrolyte facilitating ionic transport are either ruptured or forced from the sphere bed (e.g., see Section 5 and the Appendix). At the optimum pressure, small interconnected threads of bulk electrolyte, which may be only thickened film regions, supply good ionic conductivity to small areas of supermeniscus film throughout the electrode. In this case, the first lengths of the supermeniscus films throughout the electrode are considered to supply more current than a film of longer length but of approximately the same area. Theoretical treatments used to estimate current distribution in the supermeniscus film have shown that the local current density is much higher in the first portions of the film next to bulk electrolyte than in the later portions (e.g., Ref. 16).

The above explanation appears to be the only one that fits the observations so well, and it will be elaborated in Section 5. Workers in Sweden (Refs. 21 and 24) observed that the conductivity of the supermeniscus film or electrolyte conductivity in the electrode started to increase at approximately the same pressure as the optimum pressure as the pressure is decreased. This further corroborates the above explanation. Furthermore, the observation of increases and decreases in performance with changes in pressure when the sphere bed is not flooded and when the electrode is not bubbling supports the view expressed by Lindstrom that liquid flow through the developed film can take place after a pressure change (Ref. 21).

It is concluded that the high performance of film-type oxygen cathodes depends on the formation of continuous networks of gas and liquid in the porous medium. Disruption

of either network, by excessive flooding or by rupture of liquid filaments at low flooding levels, generally will cause a deterioration in electrode performance. Moreover, differential pressure history as well as the differential pressure measurement must be considered in evaluation of electrode performance because of the hysteresis effect in internal liquid configurations. These concepts will be applied throughout Section 4 and will be treated theoretically in Section 5.

Finally, from Fig. 26, it can be seen that the optimum differential pressure is more critical in a uniform sphere bed at higher current drains and polarizations than at smaller values. At the higher values, given shifts in the applied oxygen pressure cause severe changes in performance. At lower values of current and polarization, performance also deteriorates with shifts from the optimum pressure, but deterioration is relatively less. This observation is in keeping with the greater demands of mass transport within the structure which are present at higher current drains.

4.3 EFFECT OF ELECTRODE THICKNESS

The effect of electrode thickness was determined for the 156-μ-diameter silver spheres at 25 cm of water head differential pressure for electrodes built up at this differential pressure without previous pressure change. Results are presented in Figs. 28 and 29. The data for Fig. 28 were collected with the current maintained at 15.0 mA after the first addition of spheres, and for Fig. 29, current-potential curves were obtained after each addition of spheres to enable the given current-thickness plot of isopotential curves. In both cases, the electrode thickness for which further increases in thickness have little or no change (i.e., the optimum electrode thickness) is approximately 1300 μ. Increased electrode performance due to the increase in available film area was noted until the optimum thickness was attained.

This behavior is similar to that of the prior work in 6.9 M KOH at 21.8°C and 57 cm of water differential pressure except that the optimum electrode thickness for the

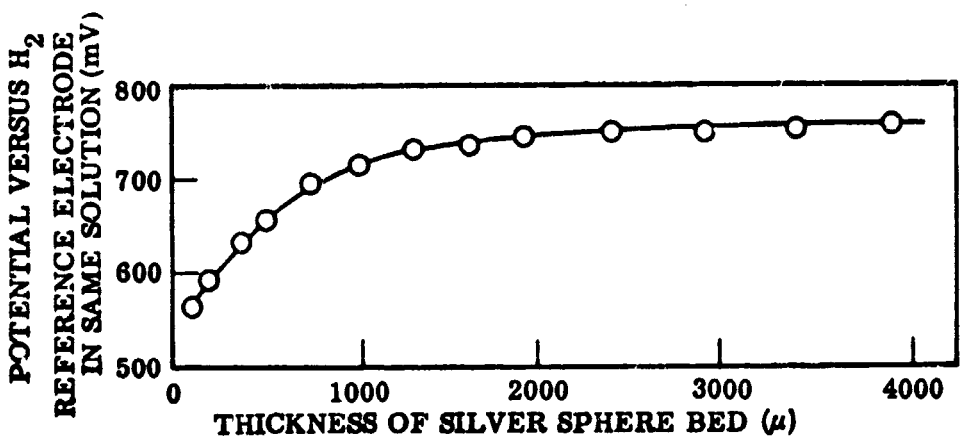

Fig. 28 Improvement in Electrode Performance as Electrode Thickness Is Increased. 156-μ Silver Spheres; Oxygen Differential Pressure, 25 cm Water; Cathodic Current, 15.0 mA (Held Constant)

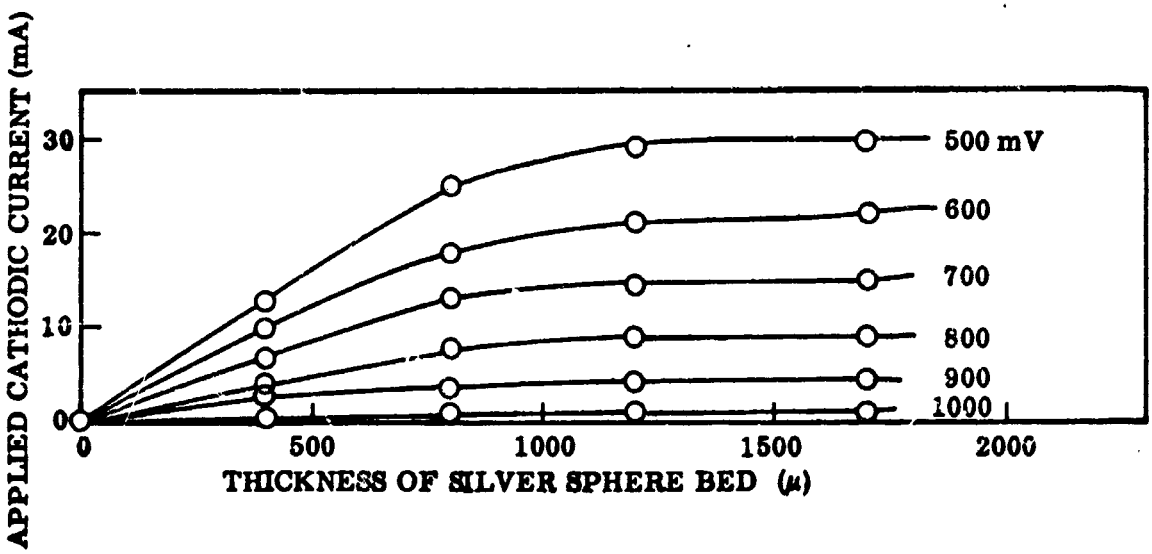

Fig. 29 Effect of Thickness Increase of 156-μ Silver Sphere Bed. Oxygen Differential Pressure, 25 cm of Water

same spheres* was then determined to be about 400 μ (Ref. 12). In the comparison of the present apparatus with the past apparatus described in section 4.1, this optimum thickness was again found to be approximately 400 to 500 μ in the 6.9 M KOH. There are three apparent differences between the two studies: temperature, concentration, and differential pressure. However, the surface tensions of the two solutions are quite close, about 90 and 89 dynes cm^{-1} for 13.5 M KOH, 95°C, and 6.9 M KOH, 20°C, respectively (see Ref. 25 and Section 5). If the predominating, acting difference in the two experiments is the differential pressure, then the observed behaviors can be explained. At high differential pressures in excess of the optimum differential pressure, more of the bulk liquid filaments (or film thickened regions) are forced from the porous structure than at lower differential pressures in excess of the optimum differential pressure. This would result in a greater restriction of ionic transport so that the portion of the film more removed from the bulk electrolyte is less effective. The effective film length (optimum electrode thickness) should be shorter at the higher differential pressure, as observed. In addition, the supermeniscus film should be thinner at higher applied pressures after liquid filament rupture if more of the isolated liquid bodies retained at sphere-to-sphere contacts are forced from the porous mass. The principal limitation of the supermeniscus film for the sphere beds again appears to be its relatively poor ionic conductivity, as concluded in section 4.2.

In reexaminations of the data in the previously reported work (Ref. 12), it can be found that the optimum electrode thickness actually increased as the sphere size was made smaller, from about 400 to 700 μ as the sphere size was reduced from 156 to 54 μ. An explanation for this effect now appears at hand. For smaller spheres, the infiltration pressures for liquids is higher and there should be more bulk liquid filaments or film thickened regions in the porous structure. The effective film length for the smaller spheres should thus be longer because of improved ionic transport as observed. We may assume that the optimum differential pressure for the 156-μ

*The more careful measurements of the average sphere diameter in the present work indicate that the average diameter is 156 μ and not 172 μ as previously reported (Ref. 12).

spheres is the same at 21.8°C in 6.9 M KOH as at 95°C in 13.5 M KOH because of the similarity in surface tensions, i.e., 16 cm of water pressure for the initial buildup (Fig. 26). The optimum differential pressure for 54-μ spheres should be (156/54) 16 or 46 cm of water pressure (see Section 5), which is still less than the utilized 57 cm of water pressure of the past work. The past results at room temperature were thus collected at differential pressures higher than the optimum pressure, and this reexamination tends to confirm the conclusions of the previous paragraph.

The data of Fig. 29 are of interest because the influence of operating current density or polarization on practical considerations of the optimum electrode thickness can be surmised. While the optimum electrode thickness is not changed with the electrode potential, the effect of making the electrode thinner than optimum is less as the electrode potential is increased (or as polarization is decreased). Thus, for very small current densities, the electrode may be as thin as 400 μ without appreciably affecting performance. For high current densities, the electrode should be at least 1200 μ thick for the 156-μ spheres to obtain maximum possible performance.

4.4 EFFECT OF SPHERE SIZE AND PORE DIAMETER

The effect of sphere size and pore diameter on optimum electrode thickness was included in the previous section for differential pressures greater than the optimum differential pressure. It was concluded that an increase in differential pressure would then cause a decrease in the optimum electrode thickness, possibly with some loss in performance. In this section, the results are given for electrodes built up and maintained at 25 cm of water differential pressure for silver spheres with average diameters of 86, 54, 38 and 14 μ. For a sphere 86 μ in diameter, the optimum differential pressure should be, by comparison with the 156-μ spheres, (156/86) 16 or 29 cm of water. The effect is thus determined of decreasing sphere size or effective pore diameter for structures subjected to a differential pressure which is less than the optimum differential pressure. The effective pore diameter in this study is proportional to the average sphere diameter, and the two terms are used interchangeably.

The more important results are shown in Figs. 30 through 35. Several features are outstanding in this differential pressure region which is lower than the optimum differential pressure. Performances now decrease, with few exceptions, as the sphere size is decreased and as electrode thickness is increased beyond a certain thickness while pressure is held constant. This behavior is in contrast to that for differential pressures above the optimum differential pressure previously determined and described (Ref. 12) (sections 4.2 and 4.3). The performances, while poor, afford interesting conclusions on the influence of sphere diameter.

The current-thickness curves of Fig. 29 for the 156-μ spheres may be compared with those of Fig. 30 for the 86-, 54-, and 37-μ spheres at 500 mV. Performances are found to decrease as sphere diameter is decreased, evidently owing to the onset of infiltration of bulk electrolyte which becomes more pronounced as sphere diameter is decreased. The increase in specific surface area with decreasing particle size no longer causes a general improvement in performance because relatively more area is lost by partial flooding and film thickening.

In Figs. 30 and 31, another effect is shown for the 54- and 38-μ spheres. As electrode thickness is increased, increased performance is noted until a certain thickness is attained. Thereafter, increases in electrode thickness cause a decrease in performance until little or no effect is observed with further thickness increase. In general, the described behavior can be explained by the flooding of some pores and isolated regions in the electrode, with the consequent blockage of reaction sites to gaseous oxygen, and by the excessive thickening of the film. As the pores are made smaller, the fraction of the surface flooded should increase, and if the electrode is made thicker while it is in a partially flooded condition, the probability of an overall blockage of reaction sites is increased (Ref. 26). The shape of the pores in the sphere bed is actually irregular, and the pores are wide at some locations and narrow at others. For very thin electrodes having only a few layers of spheres, if the electrode is partially flooded, the parts of the pores that are wide can retain relatively good access to oxygen from the gas side of the electrode even though the parts of the pores that

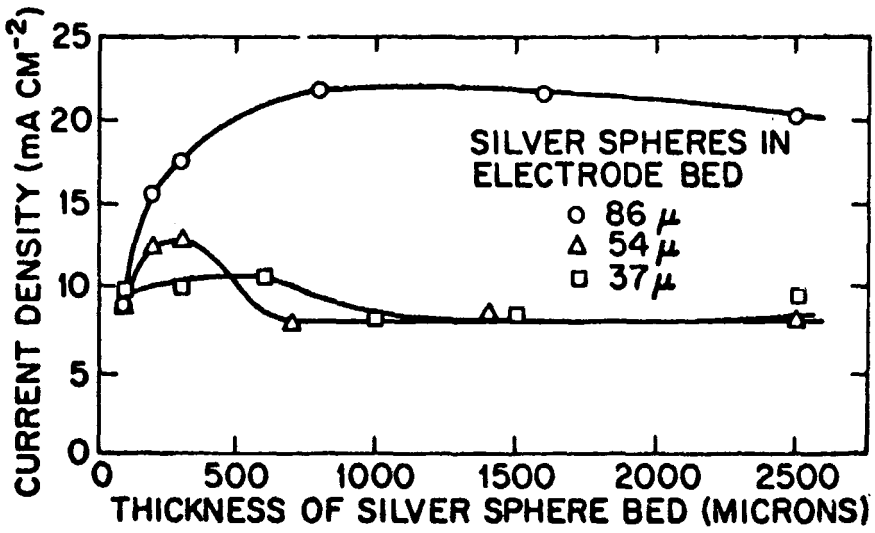

Fig. 30 Effect of Electrode Thickness on Current Density for Various Sphere Sizes. Oxygen Differential Pressure, 25 cm of Water; 500 mV Versus Hydrogen Reference Electrode

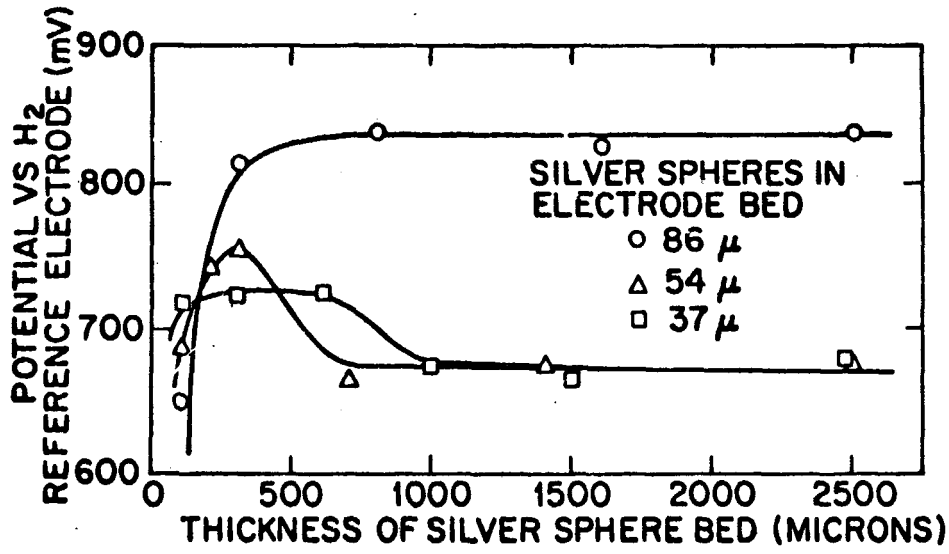

Fig. 31 Effect of Electrode Thickness on Electrode Potential for Various Sphere Sizes. Oxygen Differential Pressure, 25 cm of Water; Cathodic Current Density, 4.2 mA cm^{-2}

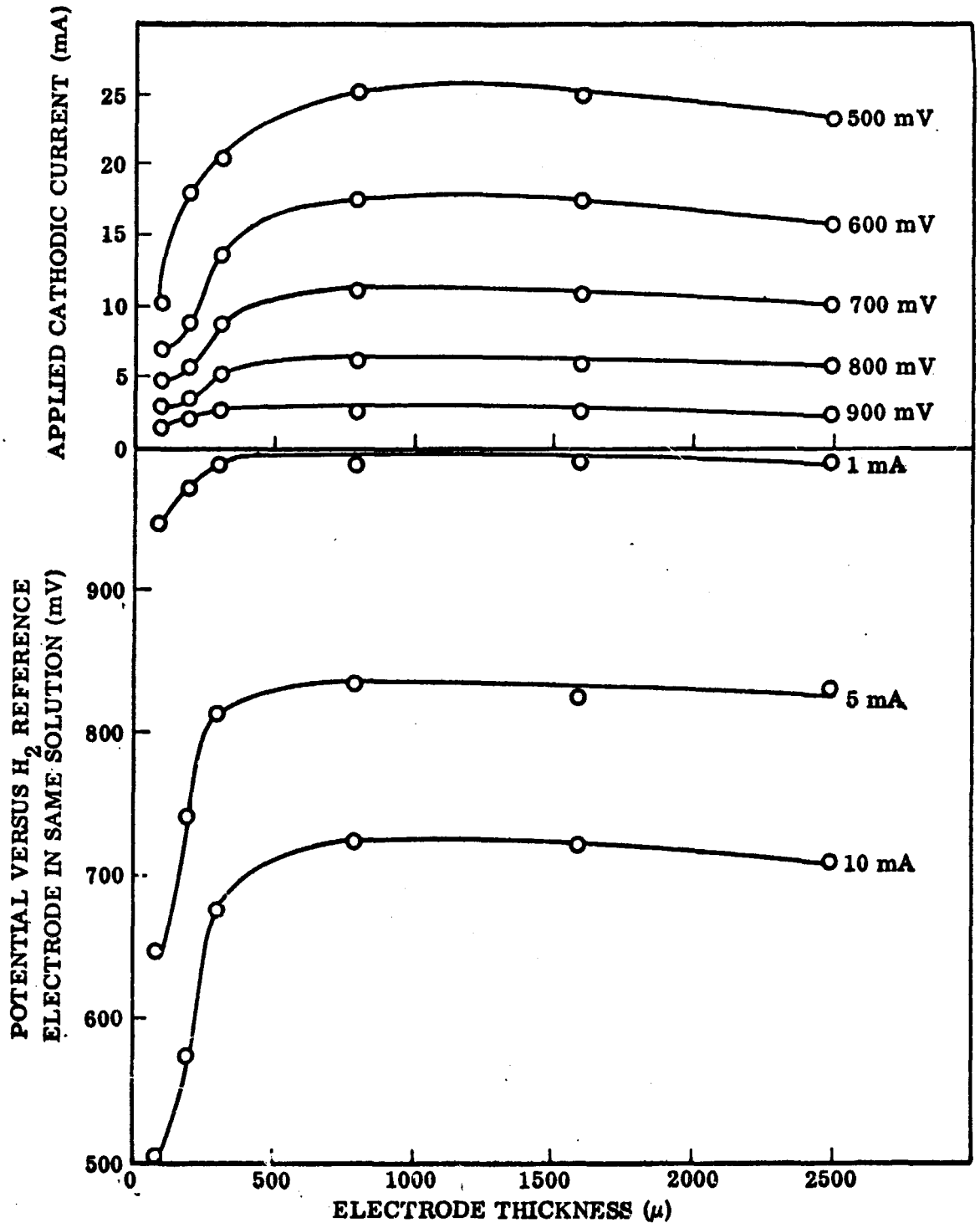

Fig. 32 Isopotential and Constant Current Curves for Different Thicknesses of 86-μ Sphere Bed. Oxygen Differential Pressure, 25 cm of Water

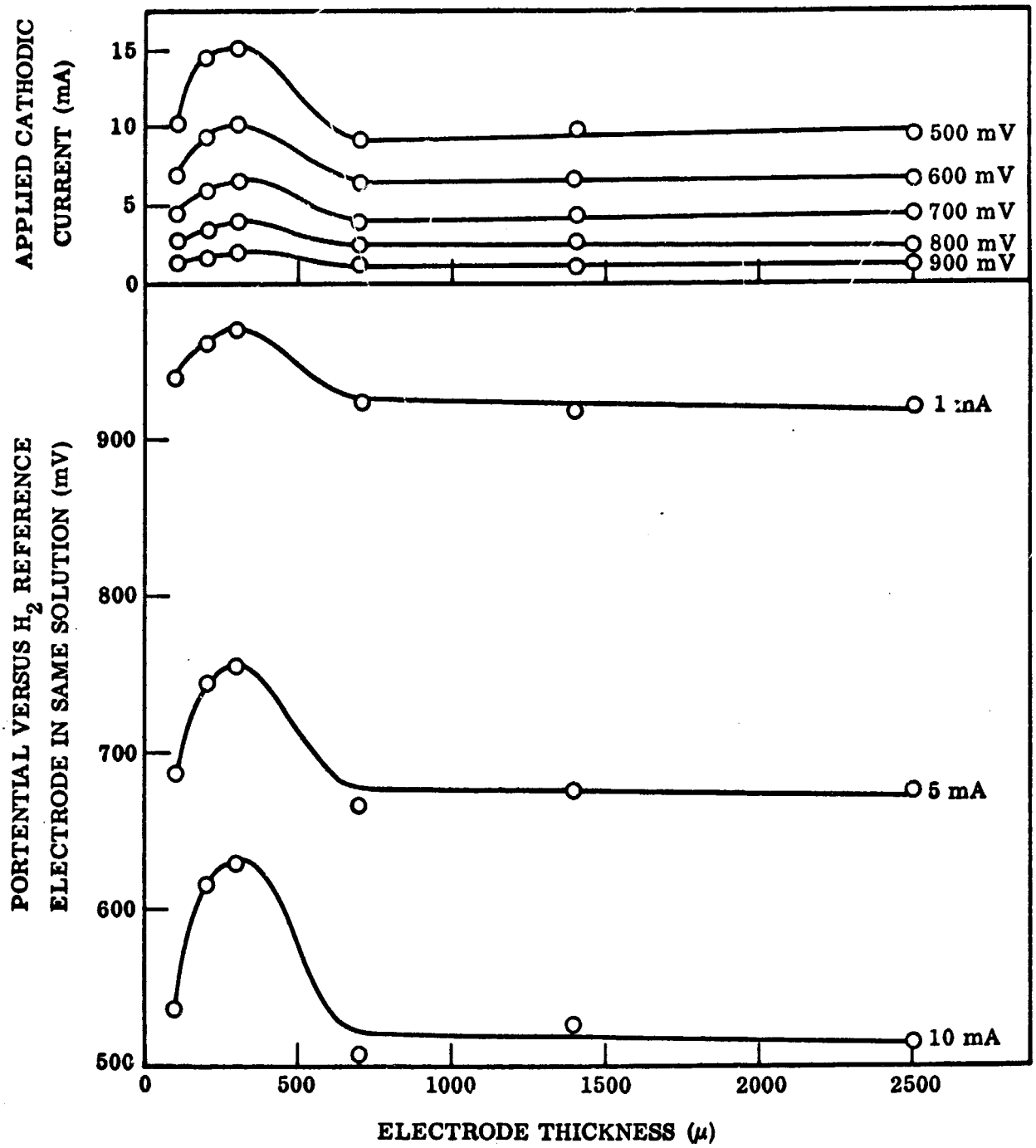

Fig. 33 Isopotential and Constant Current Curves for Different Thicknesses of 54-μ Sphere Bed. Oxygen Differential Pressure, 25 cm of Water

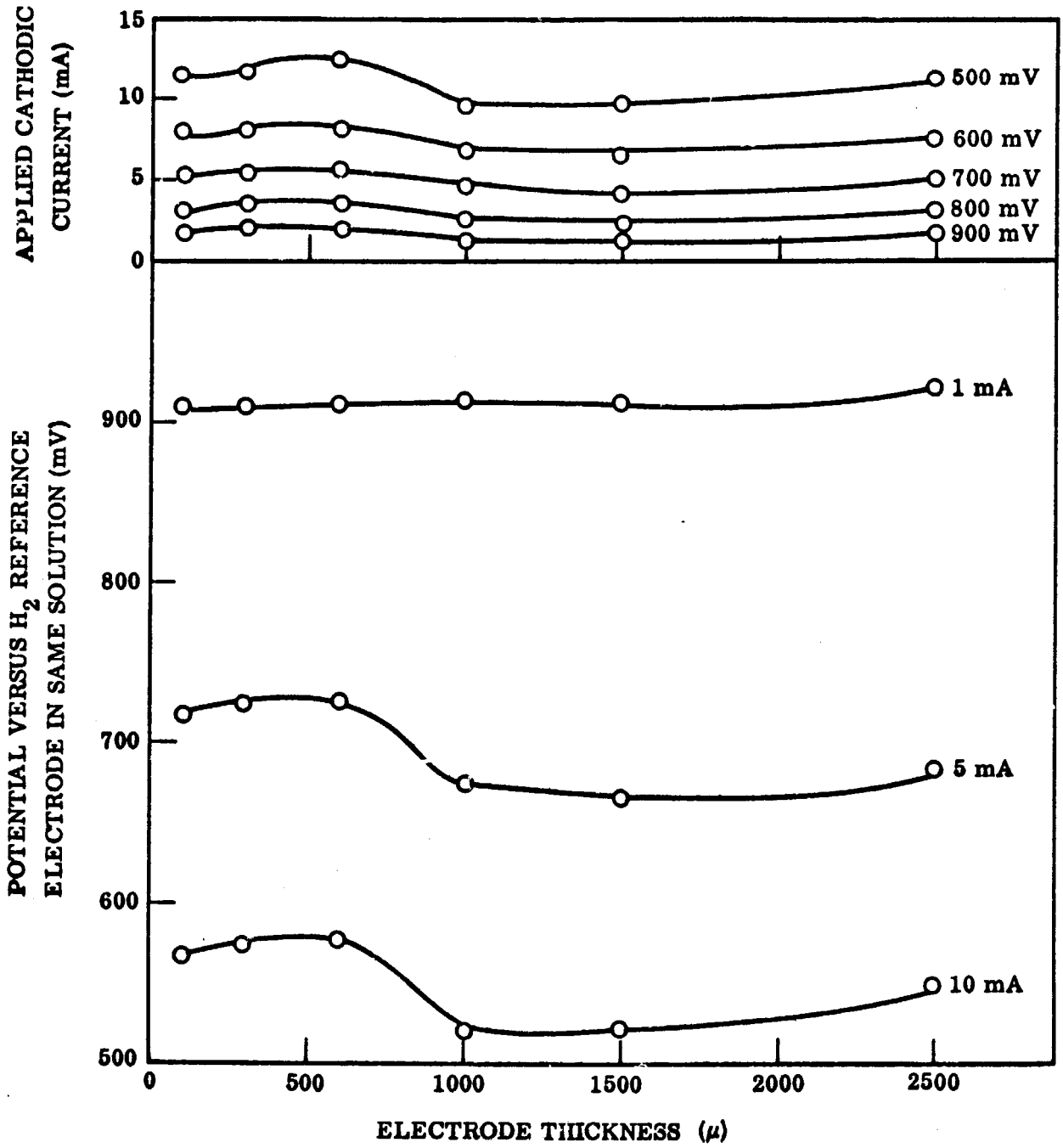

Fig. 34 Isopotential and Constant Current Curves for Different Thicknesses of 37-μ Sphere Bed. Oxygen Differential Pressure, 25 cm of Water

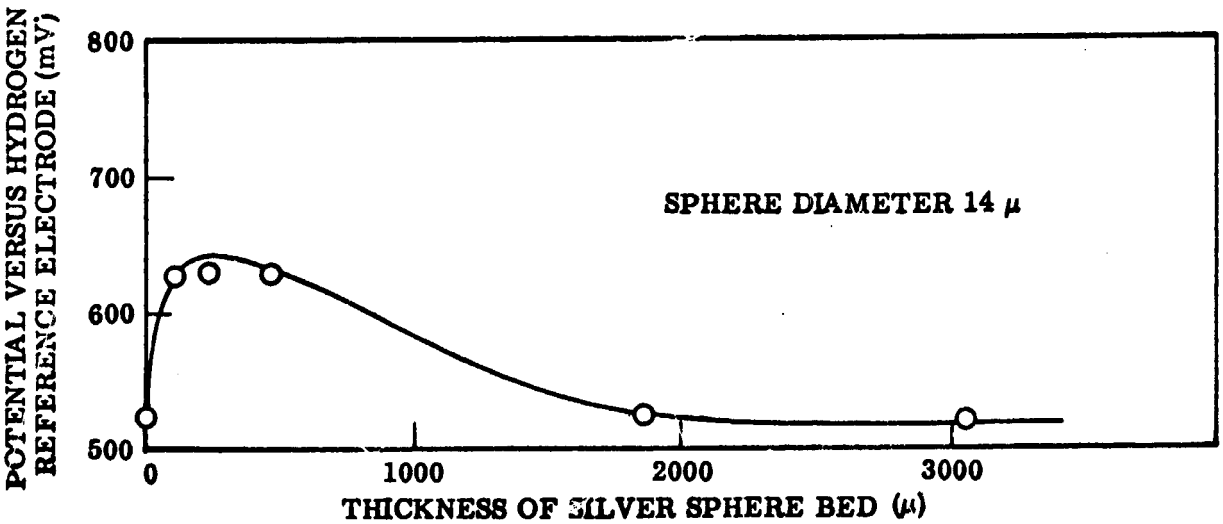

Fig. 35 Constant Current Curve for Different Thicknesses of 14-μ Silver Sphere Bed. Oxygen Differential Pressure, 25 cm of Water; Cathodic Current, 6.0 mA

are narrow are flooded. As electrode thickness is increased by some small amount, performance improves as long as the oxygen gas has relatively good access to the reaction sites on the unflooded portions of the spheres. As electrode thickness is further increased, diffusion of oxygen gas through the pores becomes increasingly difficult because the gaseous diffusion path is increased and because this path becomes more tortuous around the flooded parts of the pores.

This situation is compounded by the probability of pore blockage. For example, if some fraction of the pore volume is flooded in each layer, it can be seen that the probability of blockage of the unflooded pores in each layer by flooded pores is greatly increased by the addition of another layer after only a few layers are built up. This blockage is particularly insidious because after a small amount of the oxygen gas is consumed from the blocked pore, the electrolyte film becomes too thick for further active removal of oxygen and consequent participation in electrode performance, and the remaining gas acts to further decrease ionic conductivity.

Under these conditions, the reaction can be expected to be concentrated in a region toward the gas side of the electrode, and increases in thickness beyond some length serve only to increase transport distance along electrolyte paths through the partially flooded electrode and thus to decrease performance. Ultimately, a situation arises in which the reaction zone is located somewhere between the gas and liquid side of the electrode where ionic and gas-phase diffusive "resistances" are balanced. This effect is similar to the one reported by Maget and Roethlein (Ref. 27). As electrode thickness is increased still further, leveling off in performance is finally noted, and this may occur because the increased ionic resistance then has less influence on performance after the performance has declined and when the attainable current densities have become small.

In Figs. 32 through 34, more detailed information is given for the analyses of the effect of sphere size on electrode performance in this differential pressure regime. It can be seen from these data that electrode performance actually does improve as the sphere size is made smaller, provided that the electrode is very thin. Under these conditions, the electrode is not thick enough for the overall blockage of sites to be important, and the transport paths along the electrolyte have not yet become

very long and tortuous. Thus, the 500-mV curve for the 86-μ spheres in Fig. 32 shows better performance than the same curve for 156-μ spheres in Fig. 29 for thicknesses up to 800 μ. The 10-mA curve for 54-μ spheres in Fig. 33 shows better performance than the same curve for 86-μ spheres in Fig. 32 for thicknesses up to 250 μ, and this same 10-mA curve is better for 38-μ spheres, Fig. 34, up to a thickness of 120 μ compared with the 54-μ spheres. In Fig. 31, these effects for very thin electrodes at 4.2 mA cm^{-2} are given for direct comparison of the three sphere sizes: 86, 54, and 38 μ. At 1 mA (0.8 mA cm^{-2}) these effects occur in regions of electrode thickness too small to be detected (Figs. 32, 33, and 34); i.e., maximum performance is approached more quickly when electrode thickness is increased if the current density is low (section 4.3).

Some general comments may be made for this pressure regime. For very thin electrodes at high polarizations, an electrode should have very fine particles to give the best performance. For thick electrodes, the particles should be larger at all polarizations. For low current densities, once a certain unknown minimum electrode thickness is established, performance is insensitive to changes in electrode thickness and is improved by using larger spheres. For high current densities, the largest sphere in this pressure regime should be used, i.e., that which corresponds to the optimum differential pressure for the considered differential pressure.

The general change in the given curves as sphere size is made smaller in this pressure regime may be expected to correspond approximately to the change for a given sphere size as the differential pressure is decreased below the optimum differential pressure, with the exception of the effects described above for thin electrodes. Thus, increases in differential pressure for a given sphere size should cause a gradual disappearance of the observed performance peak in the given plots with electrode thickness, Figs. 30 through 35, and a gradual increase in the optimum electrode thickness should be observed until the optimum differential pressure is attained. This would correspond to the freeing of surface area from a flooded condition. Increases in differential pressure beyond the optimum differential pressure should then cause a decrease in optimum electrode thickness without the appearance of a performance maximum.

4.5 DOUBLE-POROSITY STRUCTURES

Double-porosity electrodes were built up at 25 cm of differential pressure with 400-μ fine layers having either 14- or 38-μ silver spheres. The coarse layers were 1300 μ thick and consisted of 156-μ silver spheres at the gas side. The total electrode thickness was 1700 μ. The differential pressure was reduced to 5 cm of water and then increased to $\geq$ 60 cm of water, and current-potential plots were determined after each pressure change.

The more important results of these experiments are given in Fig. 36, where the results of a single-porosity electrode, 1700 μ thick with 156-μ spheres, are included for comparison. A peak is observed as differential pressure is decreased and as better contact with bulk electrolyte is established throughout the sphere bed. As differential pressure is increased, another peak is observed at the onset of expulsion of the continuous electrolyte network from the sphere bed. The differential pressures at the peaks after the pressure decrease and after the pressure increase are approximately equal for the three electrodes, as expected if the 156-μ sphere beds provide the surfaces for electrochemical reaction in each electrode. The peaks obtained as differential pressure is increased are generally broader and higher than the first peaks, and this is attributed to the better liquid contact, which helps the formation of liquid filaments and films in the sphere bed after the electrode has been subjected to a lower differential pressure. The second peaks are broadest and highest for the double-porosity electrodes, and the 14/156 electrode has a broader and higher peak than the 38/156 electrode. An increase in the maximum current density to 63 mA cm^2 at 500 mV was observed with the 14/156 electrode. This type of behavior is anticipated if the finer, 14-μ sphere layer is better able to draw liquid to the interface between the coarse and fine layer.

The results of Fig. 36 may be used to show that a double-porosity electrode does more than prevent bubbling or flooding. The fine layer may serve to provide intimate liquid contact with the coarse layer. A synergistic effect occurs which assists the performance of the electrode. This effect is also apparent at higher differential

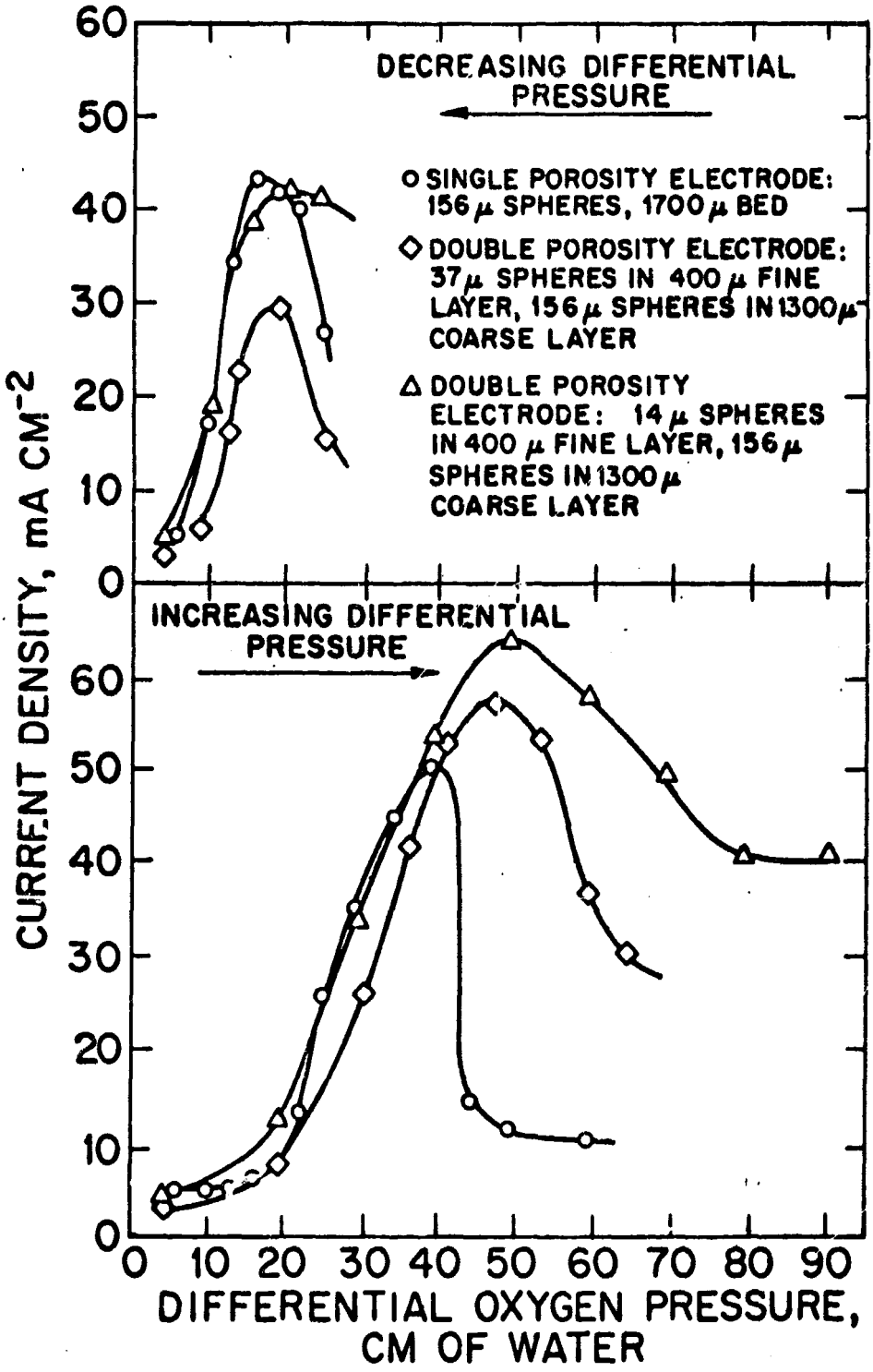

Fig. 36 Comparison of Single- and Double-Porosity Electrodes as Differential Pressure Is Changed. Silver Sphere Beds With Total Thickness at 1700 μ at Potential of 500 mV Versus Hydrogen Reference Electrode

pressures after the peak is passed and leveling in the curves is observed. Some performance contribution from the fine layer should then occur at the higher pressures when oxygen gas enters the fine pores.

The contribution to performance of the fine layer in a double-porosity electrode or, for example, in a fine middle layer in a graded triple-porosity structure with successively finer layers toward the electrolyte should become important as the optimum differential pressure of that layer is approached. The attainable current for a given potential should then be, to a reasonable approximation, the sum of currents derived from each layer considered separately at the differential pressure of the system. The optimum differential pressure for each layer of spheres should be inversely proportional to the average sphere diameter of each layer (Section 5).

In one set of experiments, a double-porosity electrode having a 400-μ fine layer of 14-μ silver spheres and a 1300-μ coarse layer of 54-μ silver spheres was built up and operated. The optimum differential pressure was estimated from the data for the 156-μ spheres given in Fig. 26 to be (156/54) 42 or 121 cm of water for the 54-μ sphere layer. In Fig. 37 are shown the results of a pressure increase for this electrode to 90 cm of water differential pressure (100 cm total). The coarse layer of this double-porosity electrode did not contribute to performance appreciably until the differential pressure reached 60 cm of water. Then a sharp improvement in performance was observed as pressure was increased further, and the performance of the electrode appeared to approach but not attain an optimum value for differential pressures up to 90 cm of water, the limit imposed by the maximum height of the water column used in the experiment. The current at 90 cm of water, 155 mA (125 mA cm^{-2}) at 0.5 V, surpassed the highest current attained with the 156-μ spheres, 78 mA (63 mA cm^{-2}) at 0.5 V, in the 14/156 double-porosity electrode of Fig. 36. These limited data at least demonstrated the anticipated sense of the shift and the improvement in performance that can be expected with the higher specific surface area for the 54-μ spheres. A cross section of this electrode is shown in Fig. 18.

If a coarse layer is placed on the electroformed mesh, it might be expected to isolate a subsequently placed fine layer from electrolyte flow through the coarser bed. The

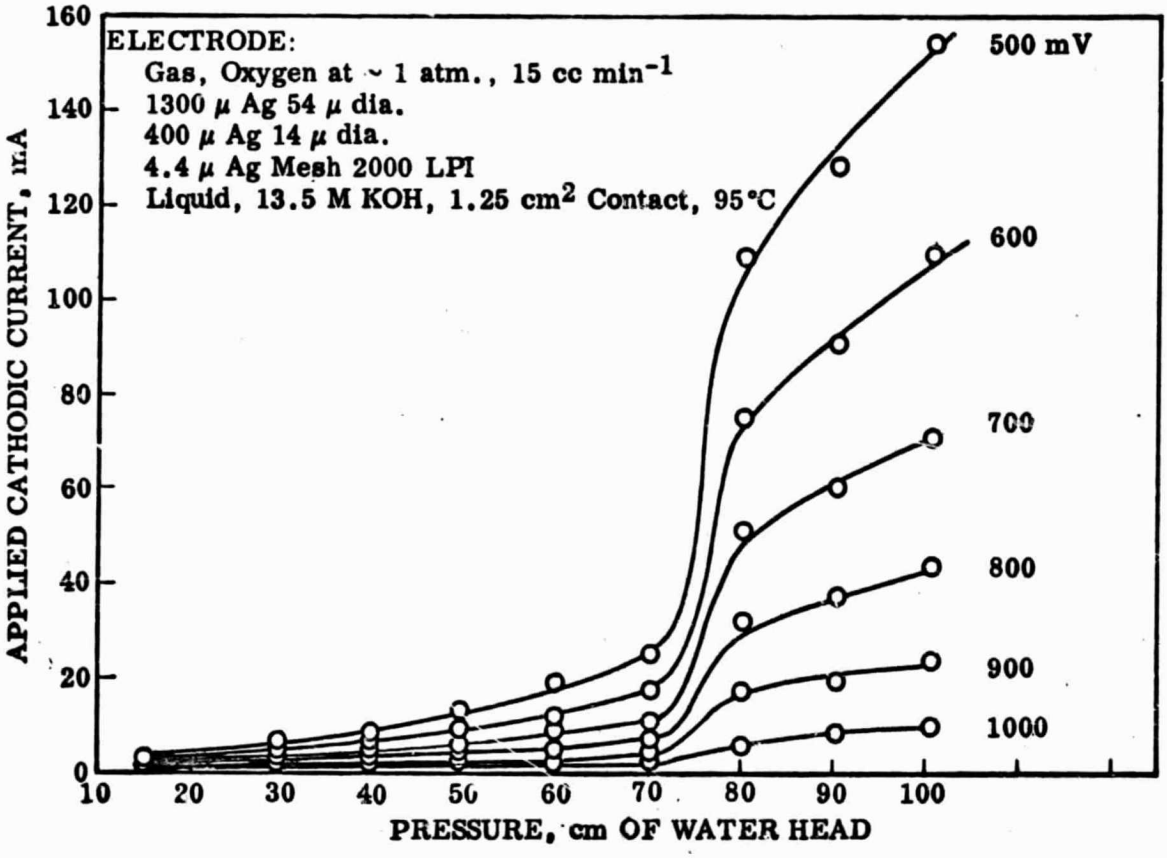

Fig. 37 Effect of Pressure Variation for Double-Porosity Electrode With Two Fine Layers (Increasing Pressure)

fine layer would then only be in contact with the thin film from the coarse layer and relatively large pores and spheres of the coarse layer, and the advantages of a higher specific surface area might be achieved without local flooding at differential pressures lower than the optimum for the fine layer. This concept was tested, and the results are given in Fig. 38 and Table 4. A coarse layer of 156-μ silver spheres was placed toward the electrolyte on the mesh, and a fine layer of 54-μ spheres was placed at the gas side on top of the coarse layer. The differential pressure was maintained at 25 cm of water head throughout the experiments so that the differential pressure for the 156-μ spheres was more than the optimum, 16 cm of water, and less than the optimum for the 54-μ spheres, which is about (156/54)16, or 46 cm of water. Electrodes were built up to a total thickness of 2000 μ with 325-, 550-, and 775-μ coarse layers. Little or no improvement in performance was noted when the thickness was increased to more than 1000 μ, and a slight improvement occurred as thicker coarse layers were used (Table 4 and Fig. 38). The performance of the "inverted double-porosity" electrode was improved over that of the single-porosity 156-μ electrode, e.g., about 40 instead of 30 mA cm^{-2} at 0.5 V under the same conditions (Figs. 29 and 38). However, the improvement was increased as the coarse layer was made thicker for the three thicknesses studied (Table 4).

Table 4

BEHAVIOR OF INVERTED DOUBLE-POROSITY ELECTRODE FOR DIFFERENT COARSE LAYER THICKNESSES

(Cathodic Current, 14.0 mA)[(a)]

Potential Versus Hydrogen Reference in Same Solution (mV)	Thickness of Coarse Layer of 156-μ Spheres (μ)	Thickness of Fine Layer of 54 μ Spheres (μ)	Overall Thickness (μ)
750	325	675	1000
760	550	450	1000
772	775	225	1000

(a) Above data reported for constant current (14 mA) during electrode buildup.

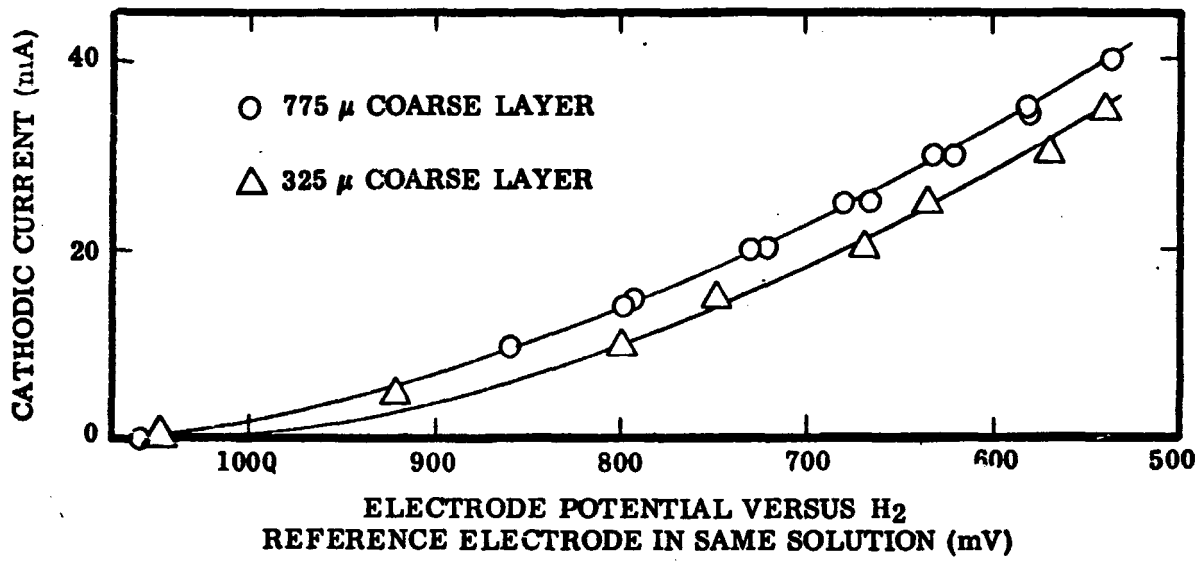

Fig. 38 Performance of Built-Up Inverted Double-Porosity Electrodes. Coarse Layer, 156-μ Spheres Next to Electrolyte; Fine Layer, 54-μ Spheres (Steady-State Data After Current Variations, ~2000-μ Electrode Thickness)

For the electrode with a 550-μ coarse layer, a serious loss in performance took place 5 min after the thickness was increased from 1400 to 2000 μ. Potential dropped rapidly to 500 mV and continued to decrease to 400 mV over a 10-min period at 14.0 mA. This behavior supports the belief that a basic instability exists with these systems because flow through the film in the coarse layer is possible. Lindstrom gives a discussion on electrolyte flow through thin films on the walls of porous gas electrodes (Ref. 21), and Muller has experimentally demonstrated this flow by his optical observations of the movement and growth of supermeniscus films on flat silver surfaces (Ref. 28). The inverted double-porosity system should eventually fail as differential pressure is increased because of the loss of effective liquid films in the coarse layer which supply ionic conducting paths for the fine layer.

4.6 TRIPLE-POROSITY STRUCTURES

Two structures were prepared containing three layers of silver spheres, each layer consisting of spheres of a different size. The first structure was prepared by building up with increasingly coarse layers towards the electrolyte, and the second structure had exactly the same thickness for each layer but with the order reversed:

Structure I:	Oxygen gas
	250 μ of 14 μ spheres
	700 μ of 54 μ spheres
	300 μ of 156 μ spheres
	4.4 μ of mesh
	13.5 M KOH
Structure II:	Oxygen gas
	300 μ of 156 μ spheres
	700 μ of 54 μ spheres
	250 μ of 14 μ spheres
	4.4 μ of mesh
	13.5 M KOH

The differential pressure was held at 25 cm of water, below optimum for the 14- and 54-μ spheres and above optimum for the 156-μ spheres. The current-potential curves of these two triple-porosity curves were about the same (Fig. 39), and the electrode performances were better than those of the single-porosity 54- or 14-μ sphere beds and poorer than the performance of a 156-μ sphere bed under the same conditions and with the same total thickness. Evidently, a type of "averaging" tended to take place. In Fig. 40 is shown the potential at 15.4 mA after each layer is added, and this behavior is of interest. The 156-μ sphere layer improved performance more when it was added on the finer layers with their good wetting contact than when added directly to the mesh. The 54-μ sphere layer improved performance more when added on 156-μ spheres than on 14-μ spheres because the coarser layer, which was not flooded, afforded some isolation from the liquid films present in the flooded 14-μ sphere layer. Finally, the 14-μ sphere layer decreased performance less when added to the spheres because of the relative isolation from the bulk liquid at the mesh which tended to decrease the extent of flooding. In each case, before optimum thickness was attained, performance was improved or deteriorated depending on whether the addition caused the added layer to approach or depart from its condition at the optimum differential pressure, respectively. The optimum differential pressure of each layer governed the final results, at least qualitatively.

The final attainment of identical performance for the two cases suggests a hypothesis for multiple-porosity structures; i.e., the performance depends on the sphere sizes in each layer and on the thickness of each layer but not on the particular arrangement of these layers. The final performances of the layered structures are as though the layers were placed perpendicular to rather than parallel to the face of the electrode. Such a law might be reasonable if all the spheres had optimum differential pressures above the operating differential pressure so that current distributions in regions of supermeniscus film could occur only from the filaments of liquid extending throughout the porous mass; i.e., it is assumed that the liquid filaments are well dispersed and large enough to present no resistance to ionic transport and that gravitational effects on the filaments are negligible. If the presence of the fine layers caused the formation

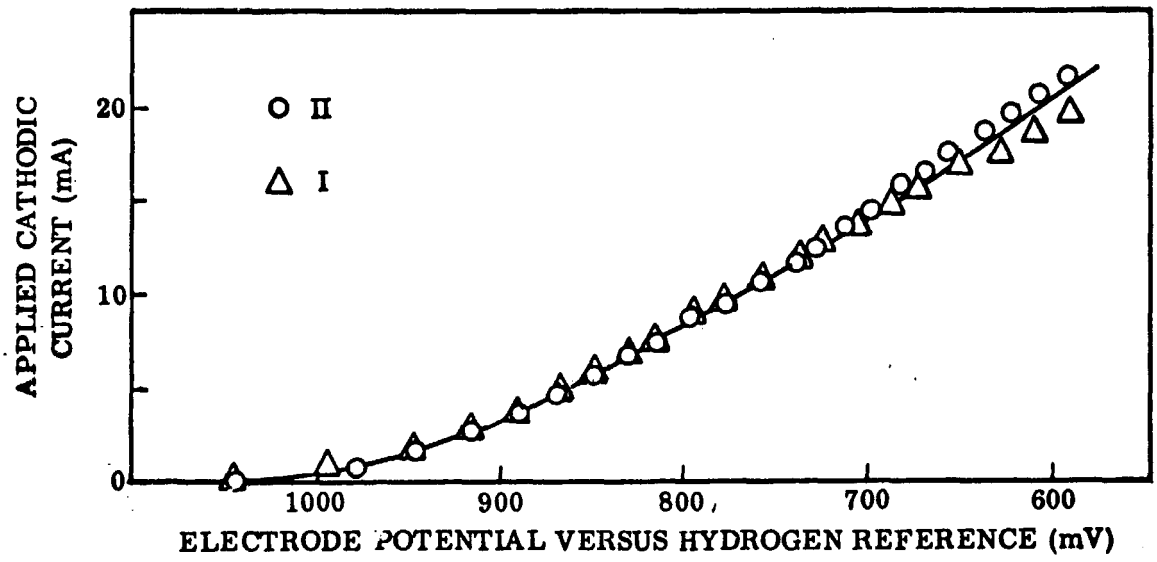

Fig. 39 Performance of Triple-Porosity Electrode Structures. Structure I With Coarse Side Toward Electrolyte; Structure II With Fine Side Toward Electrolyte

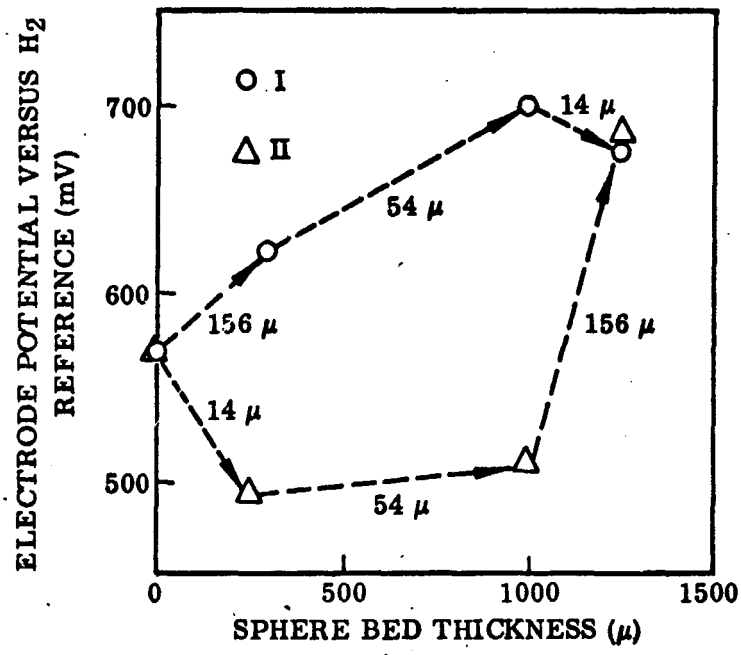

Fig. 40 Change in Electrode Potential After Layers Have Been Added for Triple-Porosity Structure. 15.4 mA Cathodic Current; Silver Sphere Sizes as Indicated

of such idealized filaments in the 156-μ sphere layer, then the results could be explained in terms of the other results of this report. It should be noted, however, that masking of oxygen by excessive flooding at gas-side fine layer would invalidate the above assumptions.

If it is assumed that performance at the optimum differential pressure improves as porosity is made finer or as sphere size is made smaller, i.e., as specific area is increased (Section 7), then broadening of the differential pressure peak to facilitate differential pressure control may best be accomplished by utilizing a graded porosity structure with successively finer porosities toward the electrolyte. As differential pressure is increased, the electrode areas that contribute to electrochemical performance would shift from the coarser layers at the gas side toward the electolyte. As the differential pressure is increased beyond the optimum value for the coarsest layers, their contribution to performance would decrease as that of the finest layers is increased. The design of such an electrode would entail determination of differential pressure – current plots for various thicknesses of each layer under the conditions of contact in the final electrode and would not be an easy task. It should be noted that for a given electrode thickness and a given minimum sphere size for the finest layer, the broadening of the differential pressure peak in this manner would theoretically result in a loss of electrochemical performance when the performance is compared with that of a single-porosity electrode using the given finest layer size. In this case, the addition of coarse layers to the gas side would require that the finest layer be made thinner for a given electrode thickness, and if the given electrode thickness is equal to or less than the optimum thickness of the finest layer, the contribution to the performance by the finest layer would necessarily be decreased. If the given electrode thickness is greater than the optimum thickness of the finest layer and if the finest layer is at its optimum thickness or thicker, the coarse layers would be too far removed from the bulk electrolyte to have an appreciable influence at the optimum pressure for the fine layer. Also, synergistic effects such as those observed with the double-porosity electrodes (section 4.5) then should not appreciably help in improving performance because the optimum pressure of the coarse layer would be exceeded. Most of the electrochemical performance of a given minimum sphere size for a finest layer should be retained, however, in designing for pressure peak broadening by allowing the electrode thickness to be somewhat greater than its optimum value for the finest

layer when this finest layer is present in a single-porosity electrode, i.e., by designing so that the reaction zone at the gas side near the flooded portions of the graded porosity electrode continually moves toward the liquid face of the electrode until the maximum performance is attained when the optimum pressure for the fine layer is attained. The thickness of each coarse layer would be designed so that it contributes to the broadening of the pressure peak to a desired extent. Further, a finer, very thin layer could be added to the liquid side of the electrode adjacent to the working fine layer to prevent bubbling if the electrode's pressure peak is unduly exceeded. By using such an electrode, the total thickness would be more than optimum for the fine layer in a single-porosity electrode although the fine layer would be present at its single-porosity optimum thickness, ohmic resistance losses would occur in the liquid through the flooded layers at pressures lower than optimum, but approximately the same performance would be obtained at the optimum pressure for the working fine layer as for a single-porosity electrode having this fine layer.

4.7 EFFECT OF PLATINUM LOADING ON SILVER SPHERES

Smooth platinum and smooth silver surfaces are probably approximately equivalent as catalysts in the reduction of oxygen in aqueous KOH solutions (Ref. 12). The coating of the silver spheres used in this work with smooth platinum should not yield appreciably different results. However, the deposition of platinum on silver by chemical displacement from a chloroplatinic acid solution is known to produce a rough surface; e.g., the surfaces are characteristically black in color. Such deposited surfaces should nevertheless behave as though they are catalytically more active because local current densities would be increased at a given potential by the increased surface area. The imparted roughness should also have some effect on the optimum differential pressure (Section 5); i.e., the roughened surface should behave as if a layer of very small spheres were present on the surface of the large spheres.

For the studied spheres, 156 μ in diameter, beds were 1300 μ thick. This corresponds to 1.009 g or to a surface area on the spheres of 37.0 cm^2 in the 1.246 cm^2 contact area of the electrode, assuming smooth spheres and considering the bed's fractional

void volume of 0.407. The deposition of 10 mg of platinum in this bed would give a thickness of 1, 265 Å if the deposit were not porous. The fact that depositions occurred by chemical displacement for a 10-mg platinum loading is considered as evidence that the deposits were porous. Otherwise, access to the chloroplatinic acid solution and subsequent platinum deposition would be blocked after only a few layers of platinum atoms were formed on the silver surface (~ 1.4 to 14 Å). Thus, the actual platinum thickness should be greater than the calculated thickness. In attempts to place more platinum (30 mg) on the silver, separation of a porous black platinum from the spheres was observed, and tests were not made with loadings of more than 10 mg of platinum per electrode. The unflooding of pores of the deposited porous platinum with its relatively small pores should require higher pressures than for the unflooding of the large pores in the silver sphere bed (section 4.4). Also, the deposited porous platinum should actually have a wide pore size distribution with some pores which are so fine that they could never be unflooded at reasonable differential pressures but with other pores which are larger and which could be unflooded more easily.

Performances were examined of electrodes in which the 156-μ silver spheres in the 1300-μ coarse layer of a double-porosity structure were catalyzed at a platinum loading of 10, 3, 1, and 0 mg per electrode or 8, 2.4, 0.8, and 0 mg cm^{-2} of facial area. The fine layer, on the electrolyte side of the electrode, consisted of a 400-μ-thick bed of uncatalyzed 14-μ silver spheres. The results of these experiments are shown in Figs. 41 through 44. The data for an uncatalyzed double-porosity electrode are included for comparison (Fig. 41).

The performance with the 10-mg platinum loading (Fig. 42) was found to be inferior to that for the uncatalyzed electrode at 0.5 V and at differential pressures of less than 57 cm of water (67 cm of water applied pressure). Under these conditions of relatively large polarizations, the layer of porous platinum with its flooded pores is too thick for the diffusion of oxygen to sustain the higher rates of electrochemical reaction; i.e., diffusion limitations occurred. At differential pressures greater than 57 cm, 0.5 V, the performance of the 10-mg catalyzed electrode was better than that of the

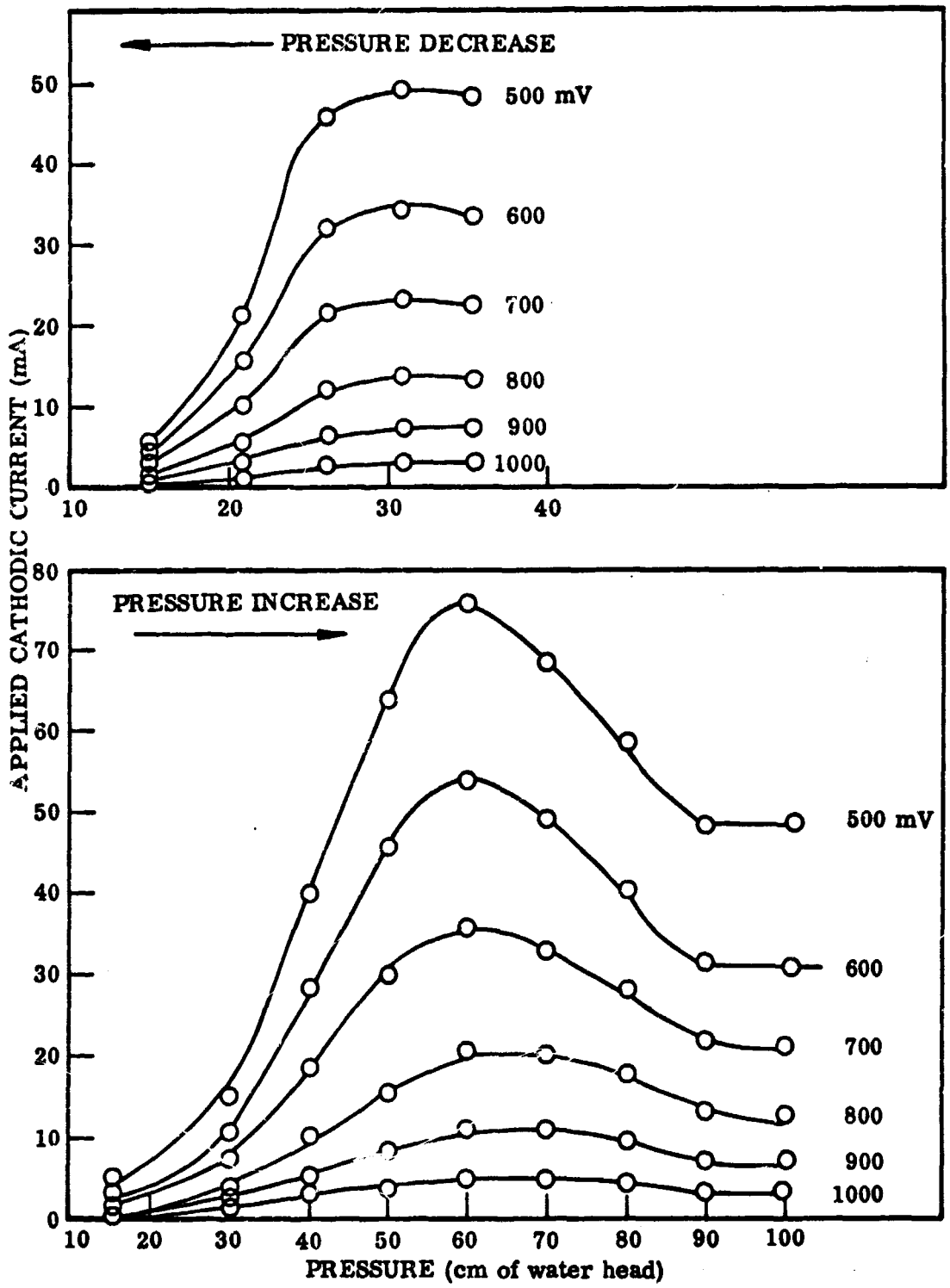

Fig. 41 Silver Sphere Bed With No Platinum in Coarse Layer

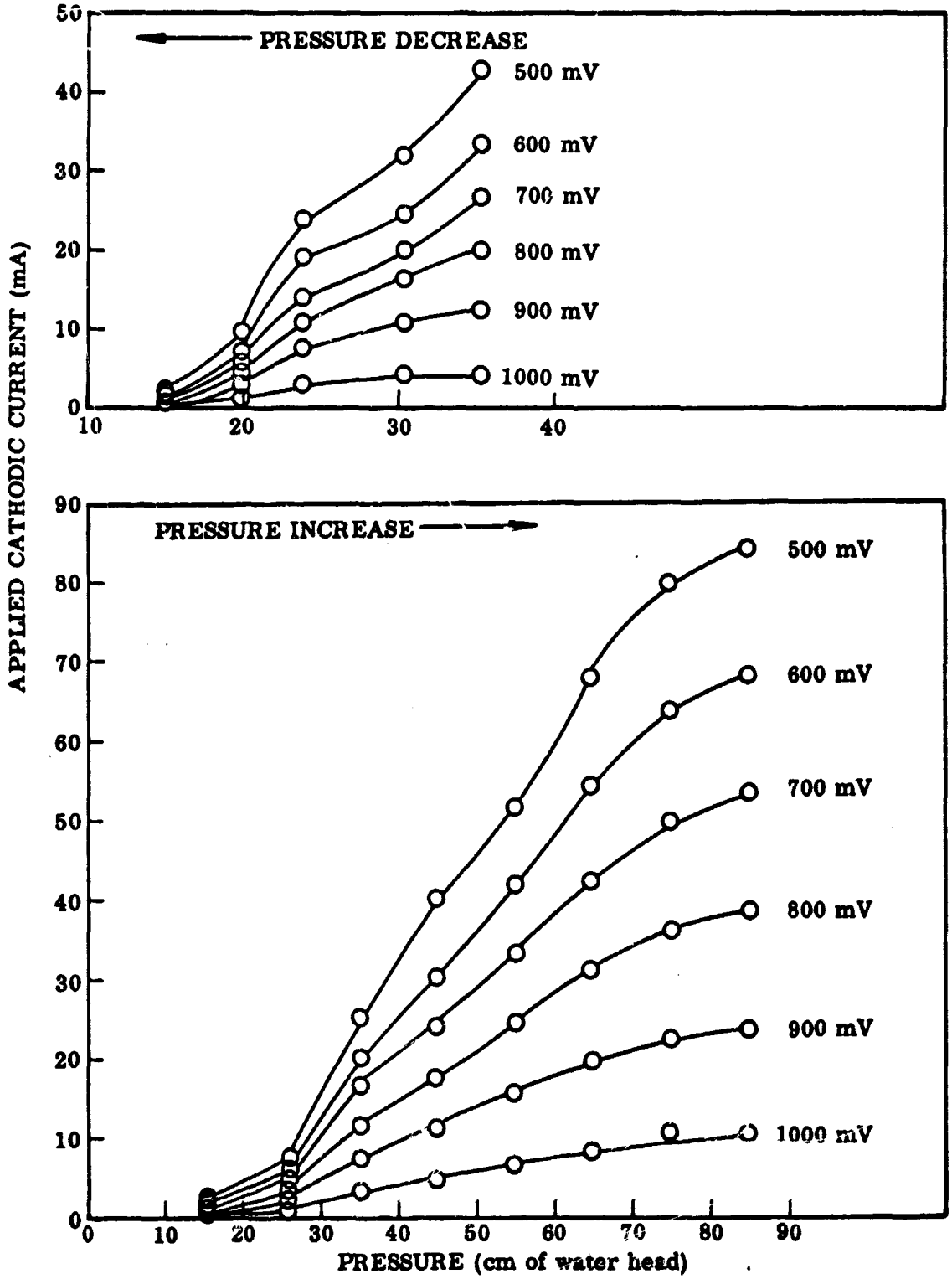

Fig. 42 Silver Sphere Bed With 10 mg of Platinum in Coarse Layer

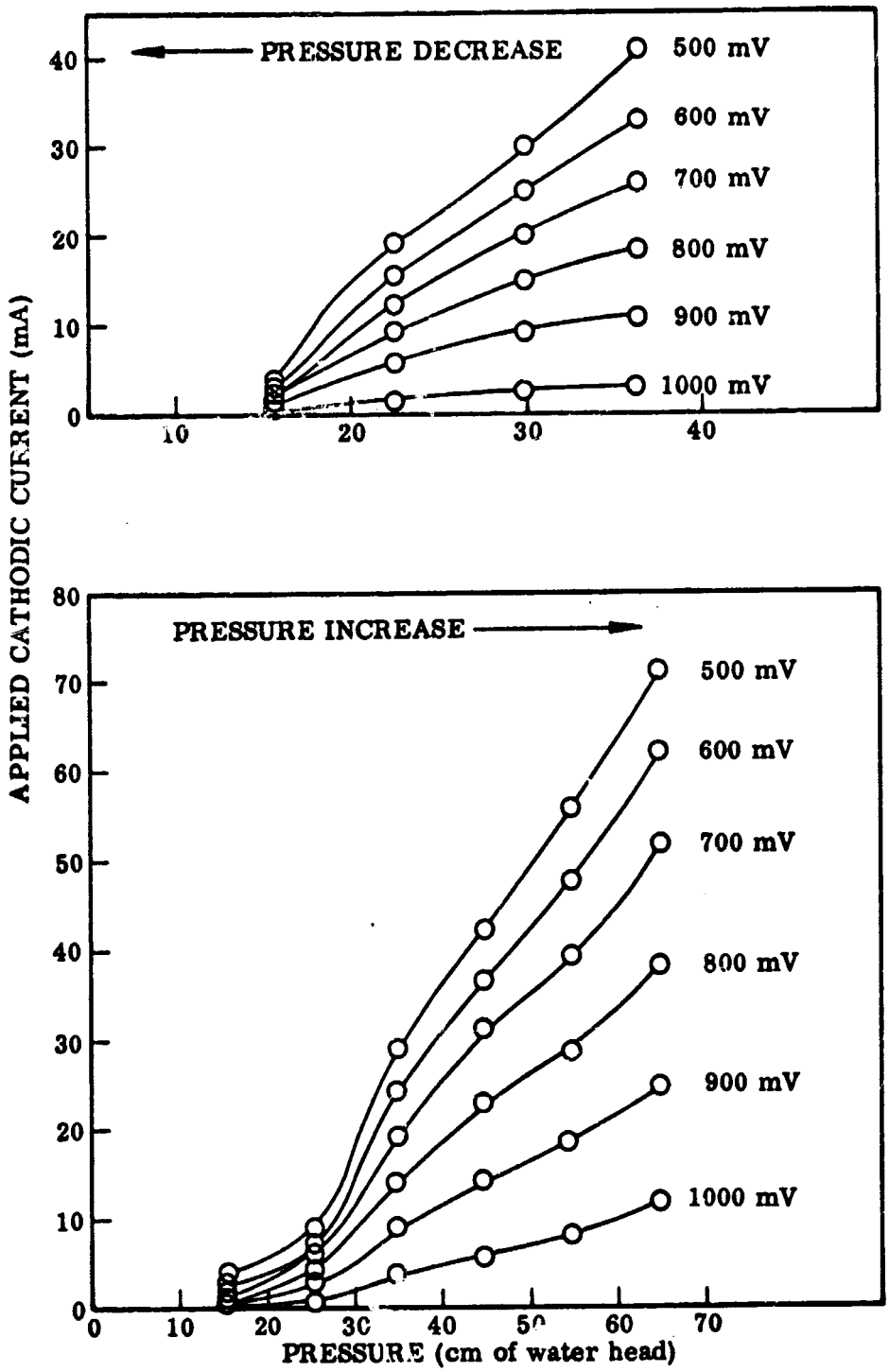

Fig. 43 Silver Sphere Bed With 3 mg of Platinum in Coarse Layer

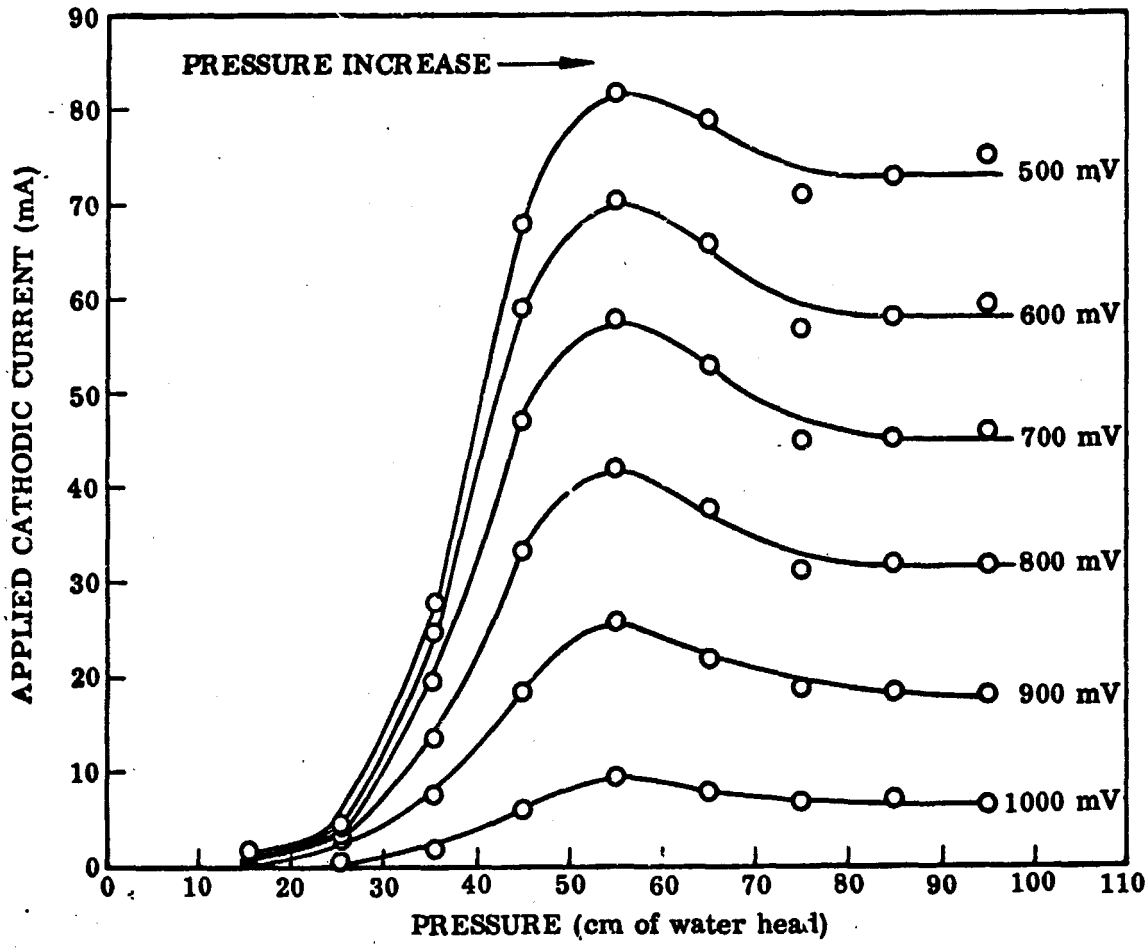

Fig. 44 Silver Sphere Bed With 1 mg of Platinum in Coarse Layer

uncatalyzed electrode because the bulk liquid began to be forced from the pores of the platinum at the higher pressure and performance continued to increase as the pressure was increased. Conversely, the performance of the uncatalyzed electrode decreased because its optimum differential pressure was exceeded and liquid filaments for ionic transport were forced out of the electrode. The optimum differential pressure of the 10-mg platinized electrode was not yet reached because the pores in the black platinum layer on the spheres are smaller than the effective pores between the spheres; i.e., the porous platinum tended to cause uncontrolled flooding at the surface of the large spheres (Section 5).

For low polarizations, e.g., at potentials greater than 700 to 800 mV, the performance of the uncatalyzed electrode (Fig. 41) was poorer than for the 10-mg catalyzed electrode over the entire pressure range studied, up to 85 cm of water (Fig. 42). At the lower rates of oxygen consumption existing at low polarizations, the thickened film in the catalyzed electrode no longer caused diffusion limitation. Rather, the increased surface area of the catalyzed electrode caused it to be superior to the uncatalyzed electrode within the confines of this low polarization region.

The performance of the electrode catalyzed at a 3-mg platinum level (Fig. 43) did not differ appreciably from that with the 10-mg platinum level over the pressure range studied. Only a slight improvement could be seen with the 3-mg loaded electrode. A better than threefold decrease in platinum content did not suffice to effectively change performance, apparently because the flooded porous platinum layer was still thick enough to cause flooding and oxygen diffusion limitations. It can be anticipated that if the platinum layer is made thin enough, eventually the largest pores in the porous platinum could become unblocked and unflooded and increased areas of super-meniscus film both on the platinum and on the silver would become available at pressures lower than the optimum for thick layers (e.g., see section 4.4). Thin layers would then give better performance than thick layers of deposited platinum. However, if the pore sizes and porosity of the deposited platinum are indeed independent of the deposited platinum-layer thickness, then as the pressure is increased to the

optimum for the porous platinum, the electrodes having a thicker layer of the platinum will have the best performance because of their greater surface area, provided the optimum thickness of the layer is not exceeded and provided gross bubbling from the electrode's larger pores does not occur.

When the platinum loading was reduced to 1 mg (Fig. 44), a marked change in performance was noted when compared with the performances of the 10- and 3-mg electrodes. An optimum differential pressure peak appeared and the performance approached that of the uncatalyzed electrode. The platinum content was now so low that film thickening by surface porosity was much less, and peak formation could occur. The 1-mg loaded electrode could be compared with 10- and 3-mg electrodes in much the same way that the uncatalyzed electrode was, and for the same reasons. At differential pressures of less than 61 cm of water, 0.5 V, the 1-mg loaded electrode was better, and the reverse was true for larger differential pressures. At low polarizations, however, the appearance of the differential pressure peak complicated comparison. In general, the performance of the 1-mg loaded electrode was better for differential pressures less than 55 to 63 cm of water because of the appearance of a pressure peak, and poorer for larger differential pressures when liquid filaments could be forced from the less heavily catalyzed electrode. The pressure at which the more heavily catalyzed spheres became more effective could now be seen to decrease from 63 to 55 cm of water as the potential was increased from 700 to 1000 mV because of the decreasing importance of film thickness or oxygen diffusion limitation (Figs. 42 and 44). For the more heavily catalyzed spheres, even though the large pores between the silver spheres could be made free of electrolyte, rupture of the liquid filaments on the surface of the spheres could not occur because of the retention of electrolyte by the porous platinum, and an optimum pressure was not observed in the studied range of pressures.

Comparisons of the 1-mg (0.8 mg cm^{-2}) loaded electrode (Fig. 44) and the uncatalyzed electrode (Fig. 41) show that the uncatalyzed electrode is now inferior at all potentials, 0.5 to 1.0 V, and at all pressures, 15 to 100 cm of water, even after the attainment of

pressures higher than the optimum differential pressure. Maximum current density with the 0.8 mg cm^{-2} loading was 66 mA cm^{-2} at 500 mV. The 1-mg platinum loading imparts a microstructure on the macrostructure of the spheres which broadens the peak and increases its height by increasing the surface area, and perhaps by introducing enough micropores to retain good liquid connections with the bulk electrolyte for ionic transport, without excessive film thickening. The fact that the optimum pressures are about the same for the uncatalyzed and 1-mg loaded electrode indicates that the latter effect is minimal and that the pores of the spheres are providing the governing geometry for the removal of liquid filaments in the sphere bed. It appears, then, that by reduction of platinum loading to a 1-mg level a simulated "catalytic effect" is approached in the observed improvement in performance.

4.8 CATALYST PLACEMENT IN THE ELECTRODE

Experiments were conducted in which a platinized silver sphere layer was placed toward the electrolyte, in the middle, or at the gas side of the reaction bed in the electrode. Silver spheres were used which were 156 μ in diameter and which had about 0.31 mg of platinum in a sphere bed layer 400 μ thick. The platinum content in the 400-μ layer was at the same loading density (milligrams per cubic centimeter) used in the 1-mg platinum loaded electrode (Fig. 43). The fine layer of the electrode was 400 μ thick and consisted of silver spheres 14 μ in diameter. This fine layer rested on the 2000 LPI silver screen which was reinforced at the electrolyte side with a coarse silver screen. The coarse sphere layer consisted of the catalyzed layer together with a layer or layers of uncatalyzed silver spheres of the same diameter, 156 μ, such that the total coarse layer thickness was 1300 μ. The following combinations were used:

Gas
400-μ catalyzed silver spheres, 156 μ in diameter
900-μ uncatalyzed silver spheres, 156 μ in diameter

400-μ uncatalyzed silver spheres, 14 μ in diameter
2000 LPI silver mesh (reinforced), 4 μ thick

Electrolyte

Gas
450-μ uncatalyzed silver spheres, 156 μ in diameter
400-μ catalyzed silver spheres, 156 μ in diameter
450-μ uncatalyzed silver spheres, 156 μ in diameter
400-μ uncatalyzed silver spheres, 14 μ in diameter
2000 LPI silver mesh (reinforced), 4 μ thick

Gas
900-μ uncatalyzed silver spheres, 156 μ in diameter
400-μ catalyzed silver spheres, 156 μ in diameter
400-μ uncatalyzed silver spheres, 14 μ in diameter
2000 LPI silver mesh (reinforced), 4 μ thick

Under the conditions of the experiment and from the previous results, the 14-μ-diameter layer is believed to be flooded. To further assure this flooding, the fine layer was brought to a differential pressure, P, near zero before the coarse layers were added at a P of 35 cm of water head. The P of the electrode was then lowered to 5 cm of water head and the results taken for increasing P.

The results for the three electrodes at 500 mV are shown in Fig. 45. It was found that the performances of the electrodes generally improve as the platinized layer is brought closer to the electrolyte for both low and high polarizations but that improvement was less when the platinized layer was changed from the gas side to the middle than when changed from the middle to the electrolyte side of the 156-μ sphere bed. Performance was greatly improved when the platinized layer was placed directly on the fine sphere bed, and a considerable broadening of the peak can be seen as well as an increase in peak height, Fig. 45. Such an effect would be anticipated if a decrease in local current density took place in the uncatalyzed sphere bed as the distance from

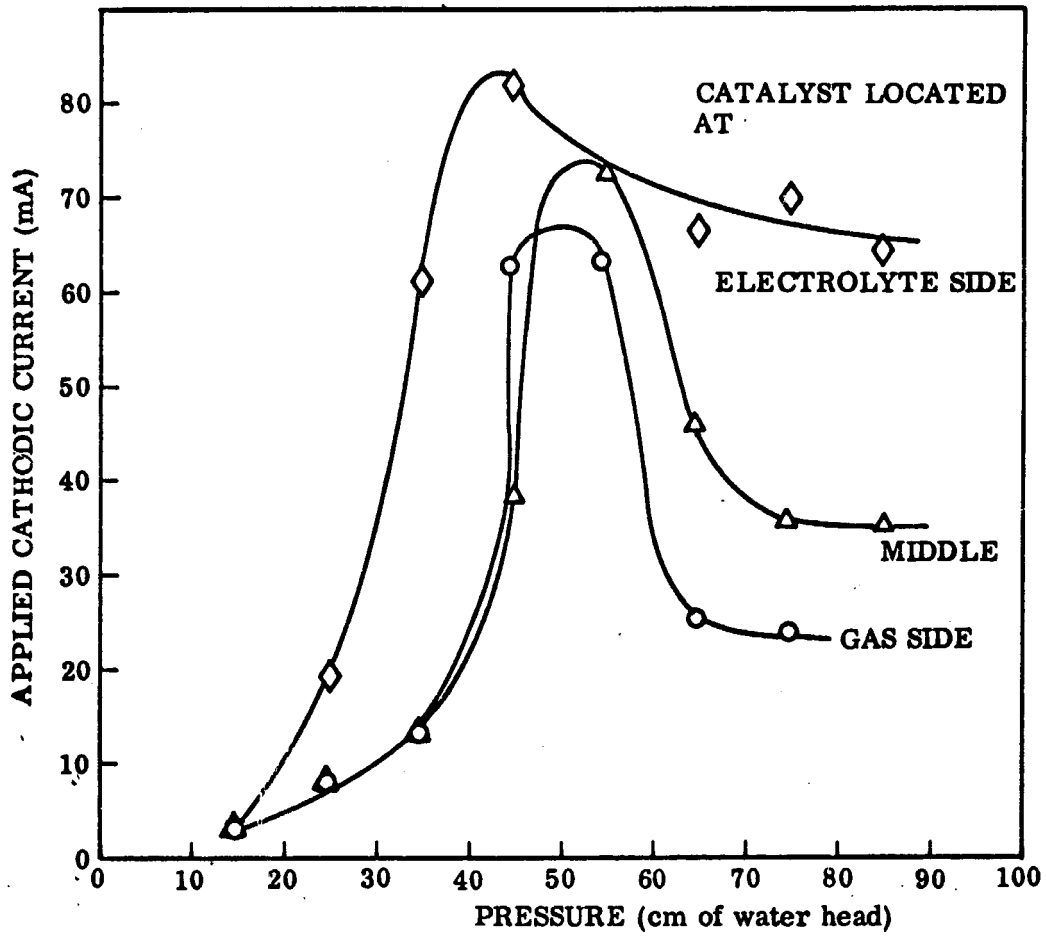

Fig. 45 Comparison of Performances With Three Types of Catalyst Distribution at 500 mV Versus Hydrogen Reference in Same Solution. Silver oxygen electrodes are compared with small amount of platinum catalyst at gas side, middle, and electrolyte side of coarse layer

the coarse/fine interface toward the gas was increased because of the limitations in ionic transport through the liquid filaments and films in the electrode. Further, the performances of the three electrodes are separated more after the optimum pressure is exceeded, when ionic transport limitation is more important than at the optimum pressure. For pressures less than the optimum, the placement of the platinized spheres at the fine, flooded layer also results in a relatively large improvement in performance, whereas the other two electrodes have about the same performance. Apparently, the ion transport limitations are important even in this partially flooded regime when the thickened films or liquid filaments are present. However, the described improvements are found at low current densities (Figs. 46 and 47), which suggests that the optimum electrode thickness has become quite small, on the order of 400 μ in this partially flooded, low-pressure regime (sections 4.3 and 4.4).

In another experiment, the amount of platinum for the same contact area, 1.25 cm^2, was maintained at 3 mg while the thickness of the coarse layer of 156-μ spheres was reduced from 1300 to 433 μ. The results of this experiment are shown in Fig. 48, which should be compared with Fig. 43 which gives data for the same electrode but with 3 mg of platinum in a 1300-μ layer instead of in a 433-μ layer. A decrease in performance occurs with the thinner electrode, probably because of the excessive thickness of the flooded porous platinum (section 4.7) and the lack of attainment of an optimum electrode thickness. The loading density (mg/cm^3) for the 433-μ electrode (Fig. 48) is about twice that of the 1300-μ electrode with 3-mg platinum (Fig. 43) and about the same as the comparable electrode with the 10-mg platinum loading (Fig. 42). The thinner electrode does not perform as well as these other two electrodes in the pressure range studied. Performances are still improving at the highest pressures tested, and comparisons could not be made at an optimum pressure.

4.9 GOLD AS AN OXYGEN CATALYST

Gold-coated silver spheres, 156 μ in diameter, were used in a coarse layer, 1300 μ thick, on top of a 400-μ-thick fine layer of 14-μ silver spheres. The results are given in Fig. 49. In Fig. 50 are given the similar curves for a 50/50 mixture

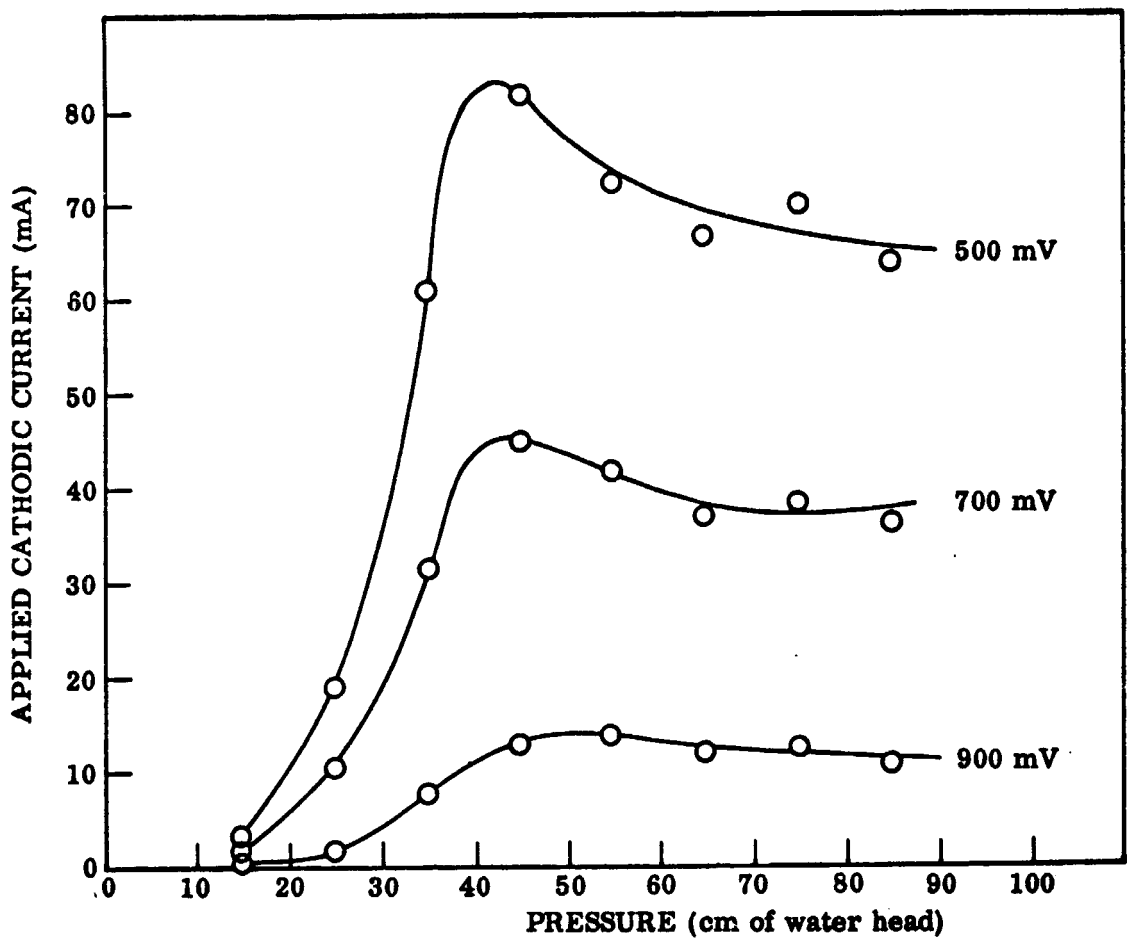

ELECTRODE:

Gas, Oxygen at ~ 1 atm, 15 cc min^{-1}

900 μ Ag 156 μ Diameter

400 μ Ag 156 μ Diameter, 0.31 mg Pt

400 μ Ag 14 μ Diameter

5 μ Ag Mesh 2000 LPI

0.5 mm Ag Mesh ~ 40 LPI

Liquid, 13.5 M KOH, 95°C, 1.25 cm^2 Contact

Fig. 46 Performance of a Silver Oxygen Electrode With Platinum Catalyst at the Electrolyte Side

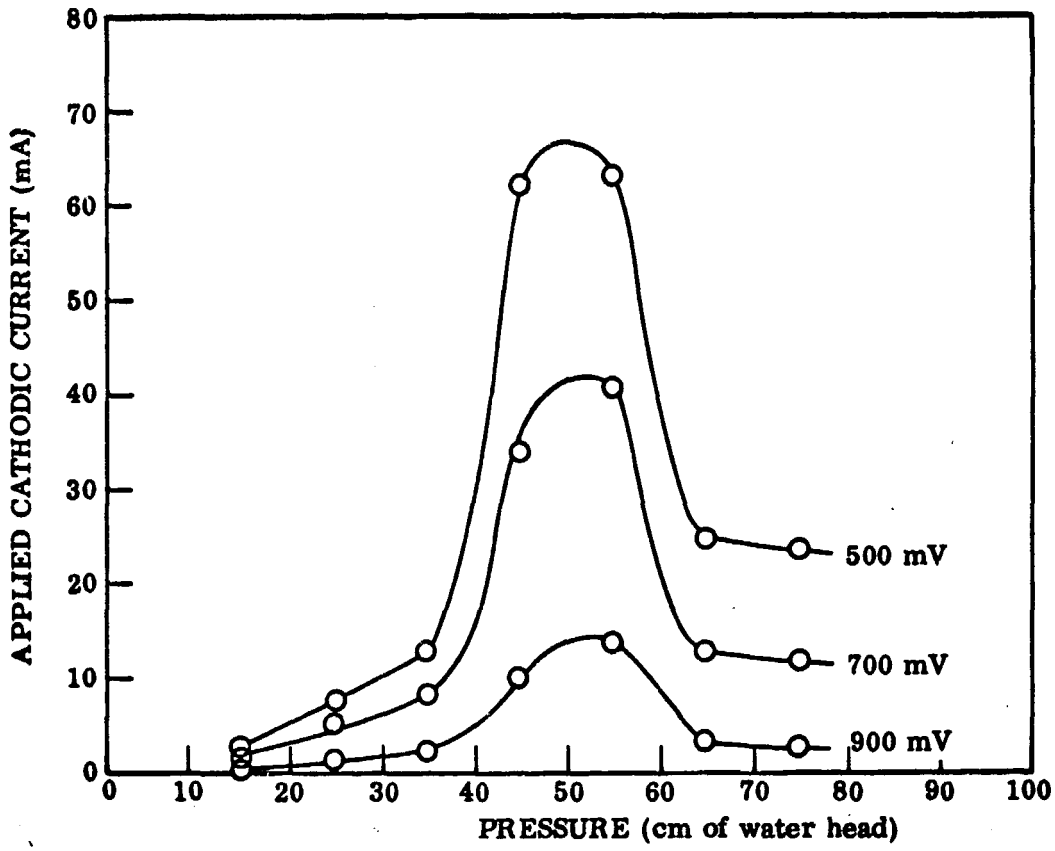

ELECTRODE:

Gas, Oxygen at ~ 1 atm, 15 cc min^{-1}

400 μ Ag 156 μ Diameter, 0.31 mg Pt

900 μ Ag 156 μ Diameter

400 μ Ag 14 μ Diameter

5 μ Ag Mesh 2000 LPI

0.5 mm Ag Mesh ~ 40 LPI

Liquid, 13.5 M KOH, 95°C, 1.25 cm^2 Contact

Fig. 47 Performance of a Silver Oxygen Electrode With Platinum Catalyst Distributed at the Gas Side

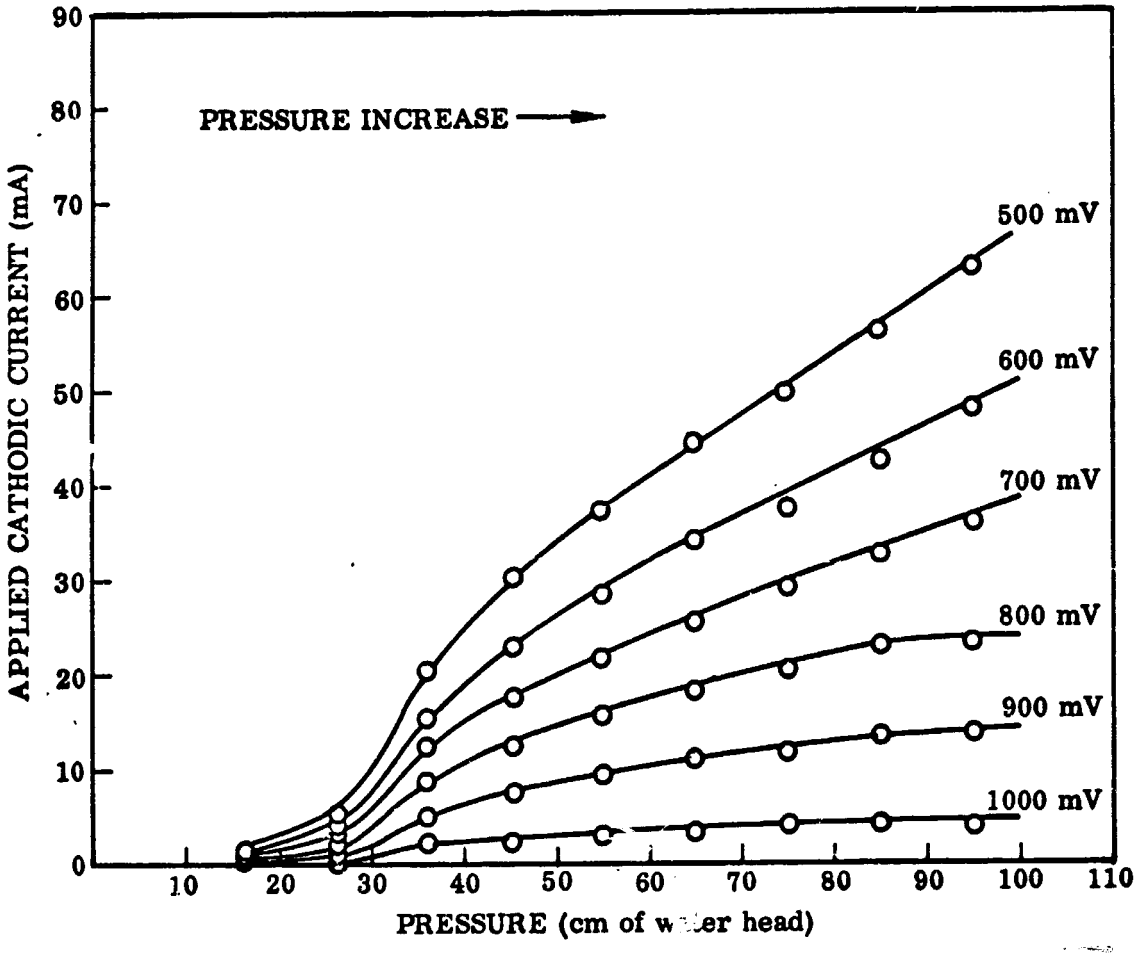

Fig. 48 Silver Sphere Bed With 3 mg of Platinum in Coarse Layer. 400-μ Fine Layer of 14-μ-Diameter Spheres; 433-μ Coarse Layer of 156-μ-Diameter Spheres

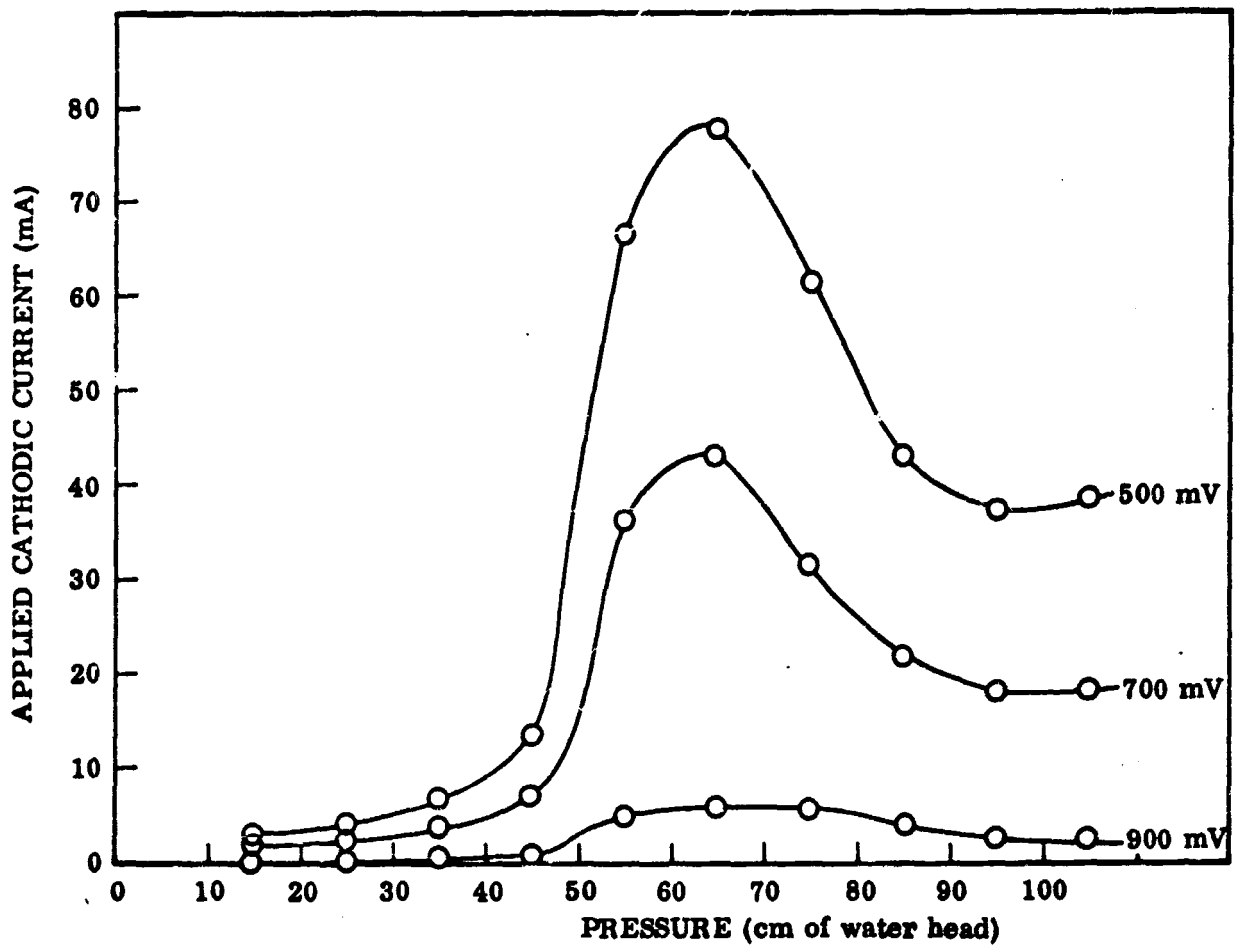

ELECTRODE:

Gas, Oxygen at ~ 1 atm, 15 cc min^{-1}

1300 μ Au 156 μ Diameter, Ag Substrate

400 μ Ag 14 μ Diameter

5 μ Ag Mesh 2000 LPI

0.5 mm Ag Mesh ~ 40 LPI

Liquid, 13.5 M KOH, 1.25 cm^2 Contact, 95°C

Fig. 49 Performance of Oxygen Electrode With Gold as the Principal Catalyst

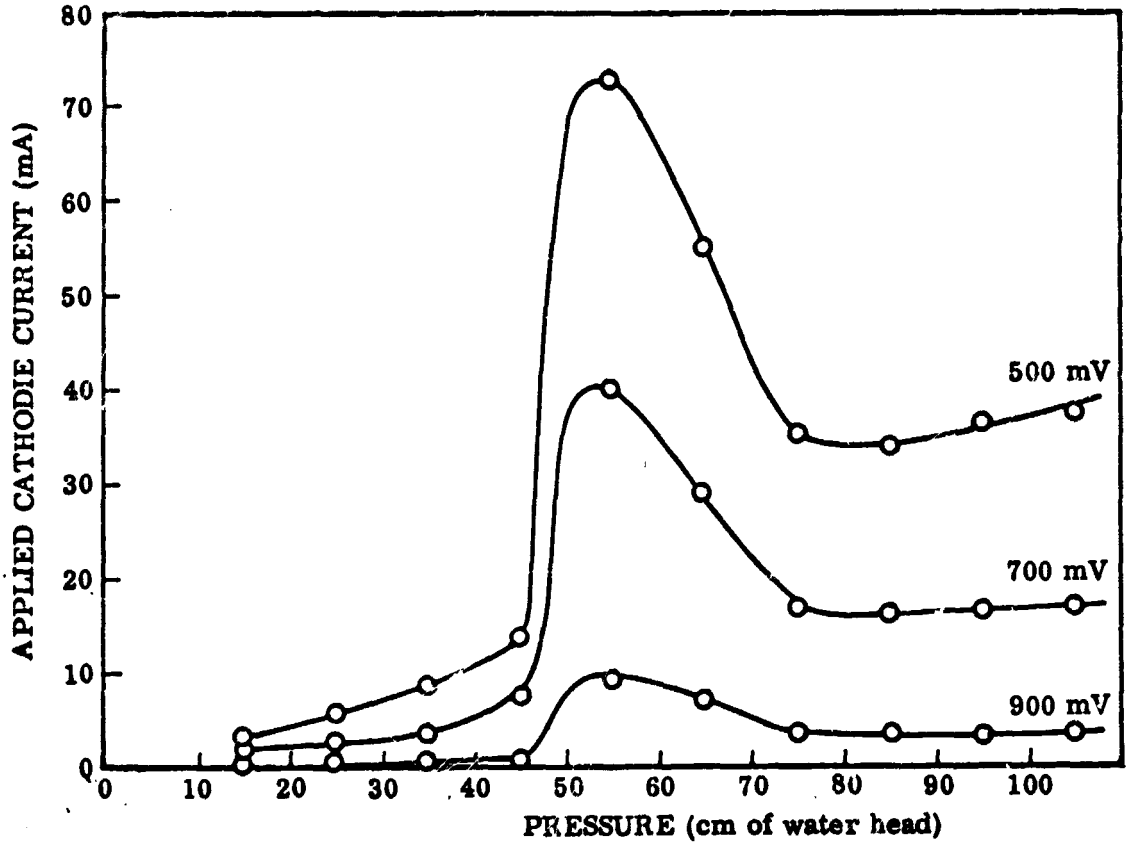

ELECTRODE:

Gas, Oxygen at ~ 1 atm, 15 cc min^{-1}

1300 μ of 50/50 Mix of Au (on Ag Substrate) and Ag Each 156 μ Diameter.

400 μ Ag 14 μ Diameter

5 μ Ag Mesh 2000 LPI

0.5 mm Ag Mesh 40 LPI

Liquid, 13.5 M KOH, 1.25 cm^2 Contact, 95°C

Fig. 50 Performance of Oxygen Electrode With Gold and Silver as the Principal Catalysts

of silver and gold-coated spheres built up to the same thickness and with the same diameter, 156 μ. These results of Figs. 49 and 50 may be compared with the results obtained with the fine layer by itself without a coarse layer present, Fig. 51. The fine layer contributes more to performance as the differential pressure is increased, and eventually its contribution should mask the contribution of the coarse layer, i.e., at differential pressures approaching (156/14) 42 or 457 cm of water. In the utilized range of differential pressure, it is seen that the gold-coated silver spheres contribute about as much as the silver spheres of 156-μ diameter by a comparison of Figs. 49 and 50 and by comparison with the results for a similar all-silver electrode, Fig. 41. The gold coating is believed to be nonporous, from superficial microscopic examinations, and these spheres were not attacked by nitric acid. The use of gold as an oxygen catalyst was suggested by its high specific rate constant in the decomposition of dilute, alkaline hydrogen peroxide solutions (Ref. 29).

4.10 NICKEL AS A SUBSTRATE MATERIAL FOR PLATINUM

The use of platinum catalyst on nickel spheres was found to give performances almost as good as with platinum on silver spheres of the same diameter and with the same platinum loading. Nickel spheres, about 156 μ in diameter, were catalyzed with platinum to a level of 10 mg per 1.2 cm^2 for a 1300-μ-thick bed placed on a 400-μ layer of 14-μ silver spheres. The results are given in Fig. 52 , and a dashed line shows the results with silver spheres with the same platinum loading, thickness, and diameters from Fig. 52 . The platinum-on-silver combination yields better results than the platinum-on-nickel combination, although the results were comparable and hardly distinguishable at lower polarizations, i.e., at 900 mV versus the hydrogen reference electrode.

4.11 THE EFFECT OF TEFLON LOADING

A minimal amount of Teflon TFE powder having 1-μ particles (advertised) of 17 mg was mixed with 1 g of silver spheres, 156 μ in diameter, which had previously been catalyzed with 10 mg of platinum (as outlined in Section 3) and which occupied a

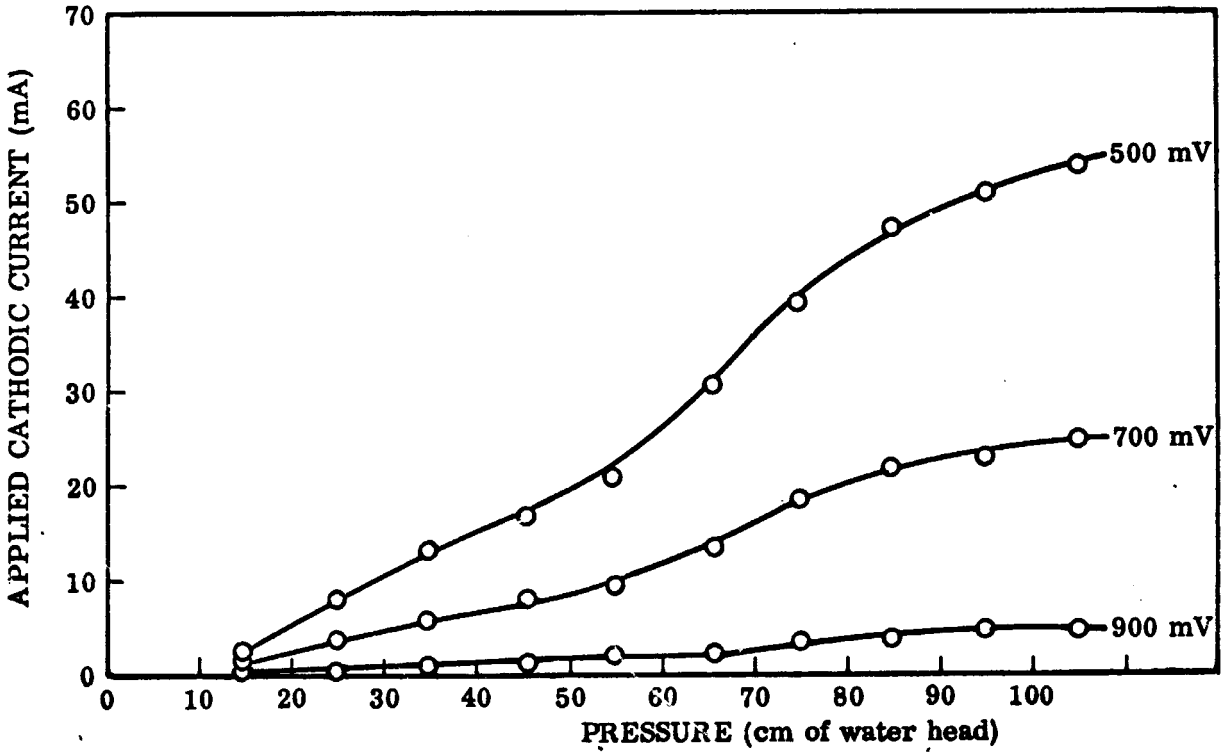

ELECTRODE:

Gas, Oxygen at ~ 1 atm, 15 cc min^{-1}

400 μ Ag 14 μ Diameter

5 μ Ag Mesh 2000 LPI

0.5 mm Ag Mesh 40 LPI

Liquid, 13.5 M KOH, 1.25 cm^2 Contact, 95°C

Fig. 51 Performance of Silver Oxygen Electrode With Only a Fine Layer Present

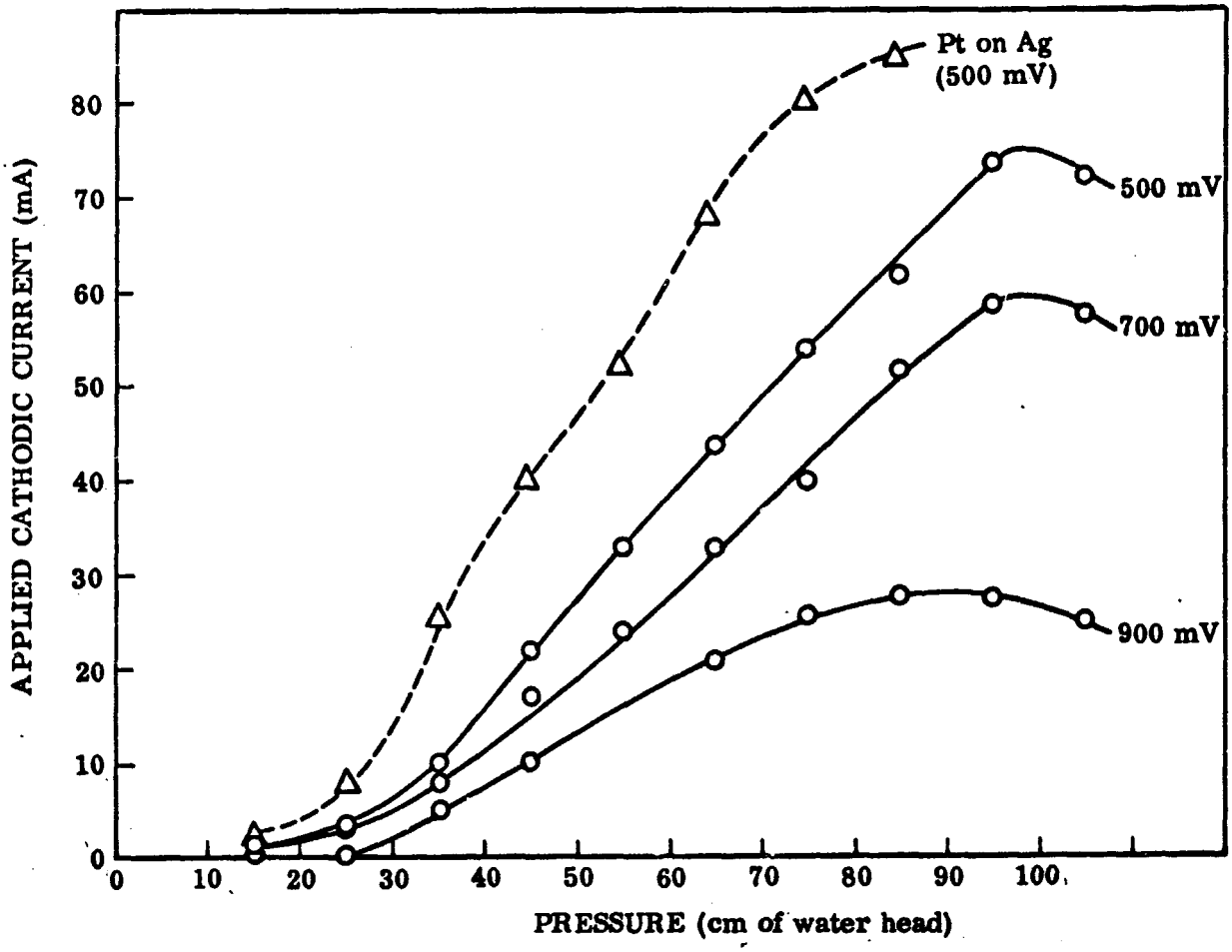

ELECTRODE:

Gas, Oxygen at ~ 1 atm, 15 cc min^{-1}

1300 μ Ni 156 μ Diameter, 10 mg Pt

400 μ Ag 14 μ Diameter

5 μ Ag Mesh 2000 LPI

0.5 mm Ag Mesh ~ 40 LPI

Liquid, 13.5 M KOH, 1.25 cm^2 Contact, 95°C

Fig. 52 Performance of an Oxygen Electrode With a Platinum Catalyzed Nickel Coarse Layer

1300-μ-thick coarse layer in the 1.2 cm^2 of the electrode. A fine layer was used, as previously described (section 4.10). An infinitely high ohmic resistance was found for the coarse layer, and when this electrode was run no appreciable improvement was noticed over the fine layer by itself (compare Figs. 51 and 53). A 17-mg TFE loading had previously been used successfully with black platinum (Ref. 30), but the surface area of the silver spheres was too low for such a loading. Less and less Teflon was mixed with the spheres until the specific resistance was found to be increased only slightly. This corresponded to a loading of 4.4×10^{-3} mg (3.5×10^{-3} mg cm^{-2}) of Teflon for the same number of catalyzed spheres as above or to about eighty 1-μ Teflon particles per silver sphere 156 μ in diameter. The results with this sample are given in Fig. 54. A substantial improvement is seen over the 10-mg (8 mg cm^{-2} of facial area) platinum-loaded spheres without Teflon at the differential pressures tested (Fig. 42); and at 42 cm of water differential pressure the current at 500 mV increased from 58 mA (46 mA cm^{-2}) to 98 mA (79 mA cm^{-2}). Improvement is more pronounced at lower differential pressures in the presence of small amounts of Teflon. The effect of Teflon appears to be to lower the differential pressure required to yield optimum performance. The use of too much Teflon destroyed the activity of the sphere bed by increasing its electrical resistance to prohibitively large values.

These results tend to confirm the recently reported work of Burshtein et al. (Ref. 31), which indicates that electrode performance experiences a maximum as Teflon content in platinum electrodes is increased from 0 to 100 percent. The curves of Burshtein et al. resemble the curves obtained in this work, with the differential pressure axis replaced by a Teflon-content axis, e.g., as in Fig. 50. Teflon content should act in much the same way as differential pressure if the presence of small hydrophobic particles in the electrode causes the formation of supermeniscus film areas adjacent to the particles. The correct placement of Teflon particles and porous Teflon filaments can, in theory, cause a favorable distribution of liquid and gas in an electrode resembling that distribution at the optimum differential pressure described in section 4.2 and treated in Section 5.

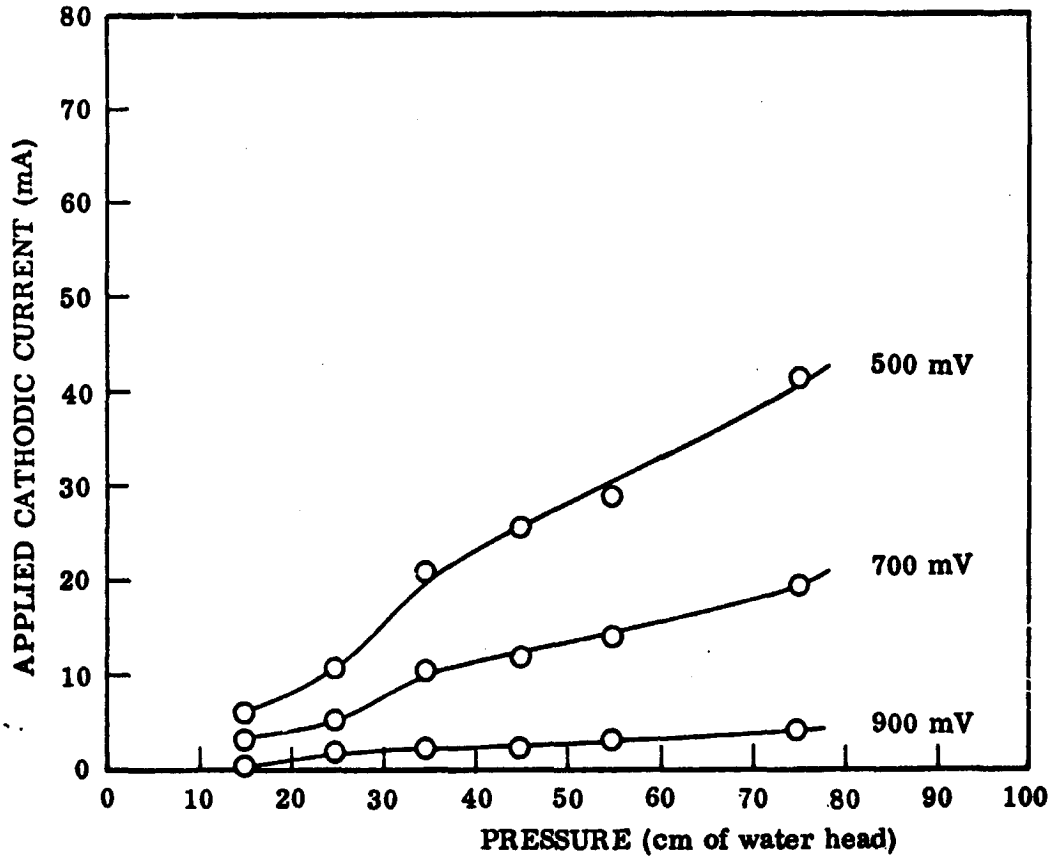

ELECTRODE:

Gas, Oxygen at ~ 1 atm, 15 cc min^{-1}

1300 μ Ag 156 μ Diameter, 10 mg Pt, 17 mg TFE Teflon Powder

400 μ Ag 14 μ Diameter

5 μ Ag Mesh 2000 LPI

0.5 mm Ag Mesh 40 LPI

Liquid, 13.5 M KOH, 1.25 cm^2 Contact, 95°C

Fig. 53 Performance of Platinum Catalyzed Silver Electrode With 17 mg Teflon Powder

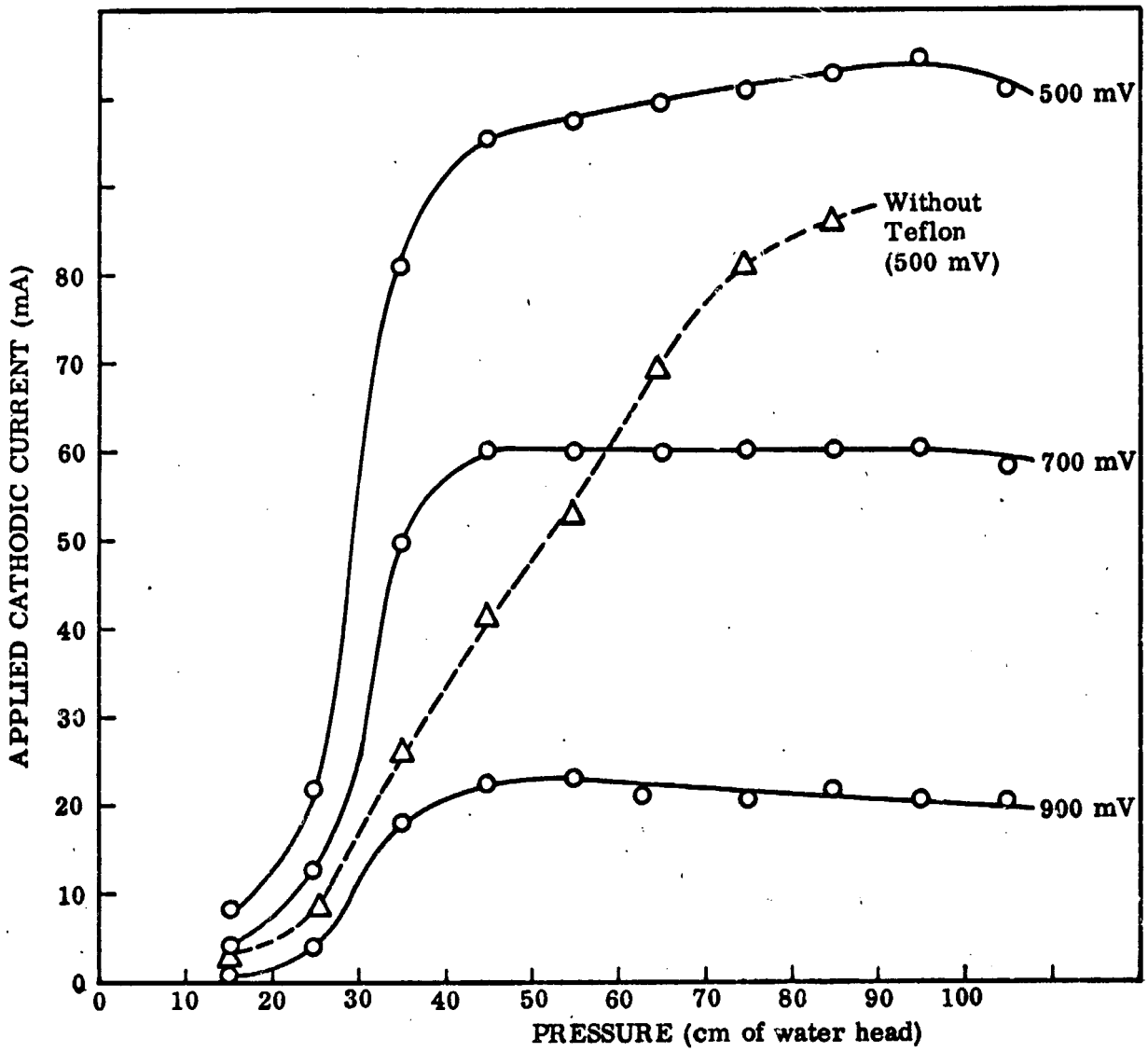

ELECTRODE:

Gas, Oxygen at ~ 1 atm, 15 cc min^{-1}

1300 μ Ag 156 μ Diameter, 10 mg Pt, 4.4×10^{-3} mg TFE Teflon Powder

400 μ Ag 14 μ Diameter

5 μ Ag Mesh 2000 LPI

0.5 mm Ag Mesh 40 LPI

Liquid, 13.5 M KOH, 1.25 cm^2 Contact, 95°C

Fig. 54 Performance of Platinum Catalyzed Silver Electrode With 4×10^{-3} mg Teflon Powder

4.12 BONDING OF SILVER IN THE ELECTRODE

In the described experiments with silver spheres, 86 μ in diameter or less, the silver sphere bed could be removed from the electroformed mesh after an experiment, often as a solid piece. The solidity of the porous mass was more or less retained even after soaking in distilled water, but it could easily be broken up with a glass rod. The electroformed mesh also had a tendency to stick to the sphere bed, but not as much as with the spheres. With the few measurements taken before these structures crumbled, it was found that the specific resistance of the bonded porous mass was very low, approaching that of the silver metal. It was determined that the bonding did not occur at open circuit but only after the electrode had been subjected to cathodic currents while acting as an oxygen electrode.

In Fig. 55 are shown photomicrographs of a cross section taken through a porous mass of the agglomerate of silver spheres. This bonded agglomerate was obtained by permitting a 3000-μ bed of silver spheres, about 38 μ in diameter, to remain for approximately 3 hr at 12 mA cm^{-2} at about 500 mV and 25 cm of water differential pressure without preflooding of the bed. Vacuum impregnation with epoxy, polishing, and etching were performed in such a way that no smearing or overlap of metal was possible. In the plane of sectioning, metal bridges at the sphere-to-sphere contacts were found as shown, and these bridges comprise the structural bonds that hold the porous mass together.

Little is known of this bonding mechanism. It is considered that the bridges may be associated with a continual oxidation of silver by oxygen and a reduction of dissolved Ag_2O (Ref. 32) by the applied cathodic current. Such a process may help surface diffusion of silver (Ref. 33), or it may be the basis for assuming diffusion of Ag_2O into the film-thickened region between the spheres where silver is then deposited. It has also been pointed out (Ref. 34) that if two pieces of metal are brought into atomic contact with one another, they will weld together, regardless of temperature. This does not happen on ordinary contacts between metal surfaces, mainly because

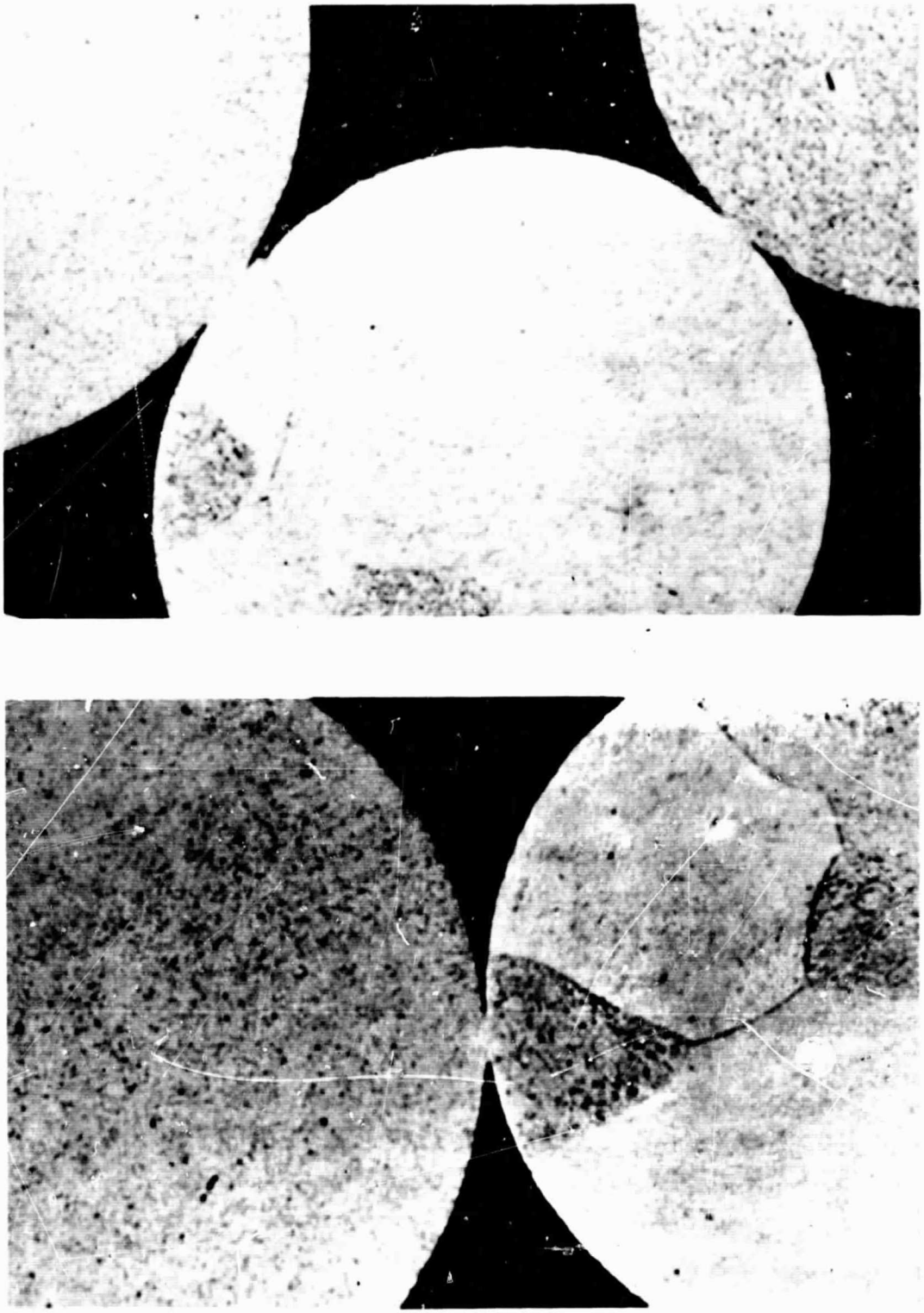

Fig. 55 Evidence for Interconnection of Silver Spheres After Electrode Operation. 3000×

each metal contains a film of oxide or other substance which prevents atomic contact. Perhaps under the conditions with cathodic currents, when freshly formed silver atoms are presented, atomic silver is made more available. This is an alternate explanation, which may be used to explain some of the transient responses that have been observed and which is perhaps more acceptable because silver oxides should be reduced rapidly at the polarized potentials of the working electrode, e.g., at potentials versus the utilized hydrogen reference of less than 1.17 V for Ag_2O (Ref. 35).

4.13 ELECTRODE RESPONSE WITH TIME

It was observed throughout the work with the all-silver electrodes that potential gradually changed in a sense opposite to its original change after the application of a constant current. For example, after a relatively large cathodic current was applied, the potential might fall immediately to 600 mV and then rise to a steady value of 620 mV after 7 min. After the cathodic current was reduced, the potential might rise to 900 mV but then drop to a steady value of 885 mV after 10 min. Such behavior has been observed by others (e.g., Ref. 15). The sense of these changes is in keeping with the suggestion that the removal of residual surface oxides is associated with good catalysis, and that their formation is associated with poor catalysis; i.e., oxygen reduction occurs more rapidly via weak adsorption than by strong adsorption, which is always competitive. The silver bonding described in the previous section would then occur more readily at heavier cathodic currents, as observed, despite the presence of an oxidizing atmosphere because of the potential at the electrode.

Another typical potential response behavior was the slow attainment of a steady state value after a current change for differential pressures below the optimum value, whether or not the electrode was preflooded. Relaxation times were typically 20 to 30 min. The thickened film apparently caused a longer time for equilibration of the system with respect to its transient intermediates. Conversely, at the optimum differential pressure, such potential responses were immediate. The volume of electrolyte in the interconnected network of liquid filaments throughout the electrode

was then minimized, i.e., just before their rupture or expulsion by a slight increase in pressure. However, above the optimum pressures, the potential responses again became sluggish, with relaxation times of about 2 to 5 min. For the slow potential responses noted above, response times were slightly longer when the cathodic current was increased.

4.14 SUMMARY AND CONCLUSIONS

The high performance of film-type oxygen cathodes is shown to depend on the formation of continuous networks of gas and liquid in the porous medium. Disruption of either network, by excessive flooding or by rupture of liquid filaments at low flooding levels, generally will cause a deterioration in electrode performance. In a series of related experiments, the importance of this internal liquid configuration was demonstrated, and it was shown how laboratory electrodes that are designed to be well characterized can be used to provide a well-controlled liquid distribution to yield as much as 50 mA cm^{-2} at 500 mV from an all-silver electrode having only 29.6 cm^2 of internal surface for each square centimeter of electrode-electrolyte contact area.

It was found that differential pressure, optimum electrode thickness, effective pore size, and pore size distribution are mutually dependent and that this dependence is governed by the differential pressure across the system which affects the internal liquid configuration. A number of experimental examples are given which can be explained and related in terms of these dependences. As differential pressure or sphere diameter is decreased, all other conditions being the same, optimum electrode thickness is increased until the onset of severe flooding, when it is decreased.

In other experiments, it was determined that platinized nickel structures were comparable in behavior to platinized silver structures, although slightly poorer; that gold could act as a suitable oxygen catalyst; and that Teflon effectively acts as though it imparts a differential pressure to the electrode. In catalyst distribution tests, it was found that a catalyst is most effective when placed at the electrolyte side of the electrode when the catalyst was platinum deposited on a silver substrate by chemical displacement.

Section 5

PENDULAR-FUNICULAR TRANSITION STATE THEORY

5.1 INTRODUCTION

An interesting series of papers by Haines appeared from 1925 to 1930 (Refs. 1–4). Haines studied the infiltration of soils with liquids and also the infiltration of beds of small spheres with liquids. He was able to show that two states of liquid internal configuration exist in partially flooded porous media, i.e., the pendular and the funicular, as shown in Fig. 56 (Ref. 9).. In the pendular state the liquid in the porous medium is distributed as isolated, pendular bodies in the form of annular rings around the points of contact of the particles. In the funicular state the pendular bodies have become joined, and the liquid forms a continuous network across the porous medium in torturous or funicular paths. The gas phase is also continuous throughout the porous medium in this region. As liquid infiltration is increased, the saturation regime or completely flooded condition is finally attained.

In Fig. 57 (Ref. 3) is shown the beginning of a transition from the pendular to the funicular state for an ideal case of hexagonal closest packing of uniform spheres. The crosses represent sphere-to-sphere contacts, 12 for each sphere, and the shaded areas represent the liquid regions. The dashed lines around the crosses show the maximum contraction of the liquid surface due to the concave curvature of the liquid. The dashed lines forming a circle between three spheres represent the shape of the liquid surface at that position. At the first stage of coalescence, Fig. 57, the liquid bodies just touch each other and the funicular state is being formed. The dry area (supermeniscus film area) of each sphere is divided into eight portions of triangular symmetry and six portions of quadrangular symmetry. At the final stages of coalescence, Fig. 58, flooding occurs simultaneously throughout the bed to enclose bubbles as shown (Ref. 3). This might be considered to form a regime which is pendular with respect to the gas.

PRECEDING PAGE BLANK NOT FILMED.

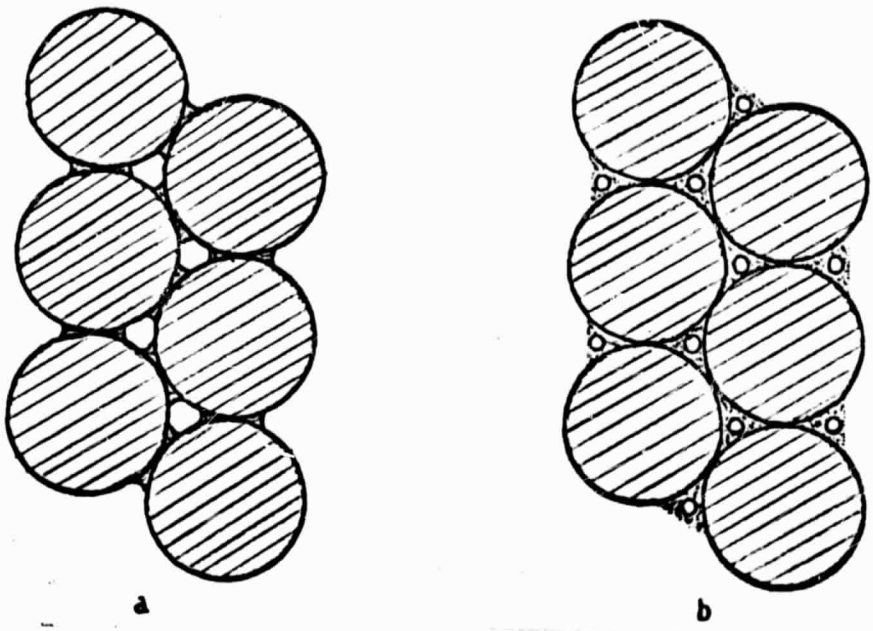

Fig. 56 Drawing of Pendular (a) and Funicular (b) Saturation Regime in the Case of an Idealized Porous Medium Consisting of Packed Spheres

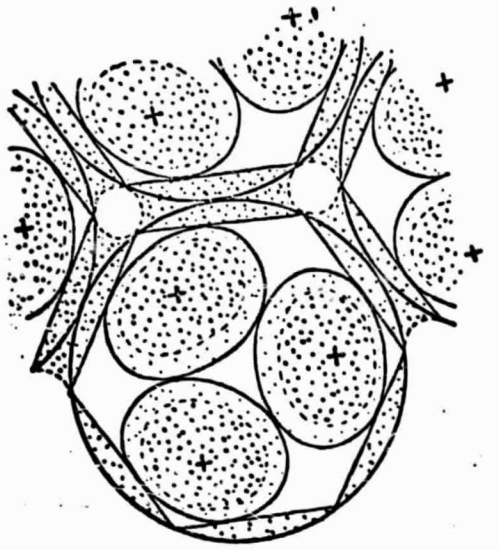

Fig. 57 Distribution of Liquid at First Stage of Coalescence

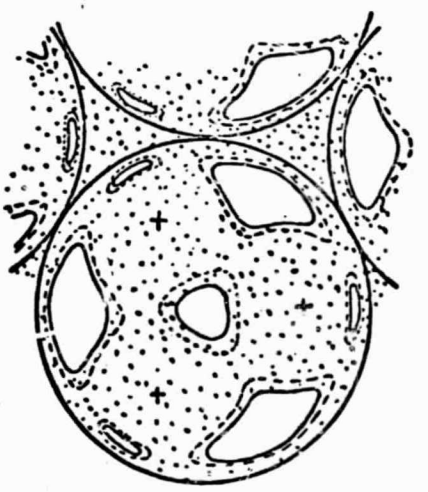

Fig. 58 Distribution of Liquid After Final Stage of Coalescence

In Fig. 59 (Ref. 3) is shown the shape of the gas passage through the bed at the onset of the funicular regime as shown in Fig. 57. Crosses represent sphere-to-sphere contacts as in Fig. 57. The dashed lines now outline the areas where gas contacts the spheres, and the heavy circles are the gas passages between three spheres perpendicular to the plane of the paper. At the lower left, this gas passage is sectioned somewhere above the plane of the paper to show how the shape of the circular gas passage changes. The heavy lines around the crosses now show the contraction of the liquid surface because of the liquid's concave curvature. In section A of Fig. 59, the dashed line is continued as a heavy line to show how the liquid shape is changed as further flooding occurs, and the very heavy line in section A represents the liquid shape at the final stage of coalescence. These configurations are necessarily idealized in a closest packing arrangement to facilitate understanding, and, in practice, for a loose packing arrangement, are distributed throughout the media in a manner which depends on the average number of contacts or nearest neighbors of each sphere.

5.2 THEORY

For a gas electrode, the most favorable liquid configuration for a bed of spheres should be formed with a funicular regime that is only slightly removed from the pendular-funicular transition state, i.e., a configuration closely resembling that shown in Fig. 57. With this configuration, interconnected and continuous funicular liquid paths would be ideally established throughout the sphere bed to assist ion transport to the bulk electrolyte; gas passages would remain open and form a continuous, interlacing network (e.g., Fig. 59) to facilitate gas transport; and isolated patches of supermeniscus film adjacent to funicular liquid could act efficiently because of the short path from the electrochemical reaction site beneath the film to the funicular liquid. Electrode performance should become poorer as a result of a slight flooding because of the loss of supermeniscus film area of this funicular state (differential pressure too low) or as a result of a slight unflooding because of a disruption of the continuous network of liquid throughout the bed to form the pendular regime with its poor ionic conductivity (differential pressure too high). This would require the existence of an optimum differential pressure.

Teflon particles or porous Teflon filaments may also be used to help establish the above described favorable liquid configuration, and some evidence for this hypothesis has been obtained in section 4.11.

With the possibility of movement of liquid through a supermeniscus film (Ref. 21 and section 4.5) which connects isolated pendular liquid bodies throughout a loosely packed sphere bed, the differential pressure required for a pendular-to-funicular transition (decreasing differential pressure) to take place throughout the sphere bed in the pendular state can be estimated. At steady state, this differential pressure should be equal to that for a funicular-to-pendular transition (increasing differential pressure) because of the movement possible through supermeniscus films, and in this transition, pendular bodies can theoretically be formed between two spheres, i.e., where the concave radius of curvature is smallest. Experimental evidence confirms the possibility of movement and growth of supermeniscus films (Ref. 28), and the role of supermeniscus films as paths for liquid electrolyte transport should be quite important.

In Fig. 60 (Ref. 2) is shown an idealized pendular body at the contact of two spheres. The equation of Laplace and Young may be used to relate the differential pressure, P, required to maintain the liquid in a given position in terms of the radii of curvature, r_1 and r_2, and the surface tension, σ:

$$P = \sigma\left(\frac{1}{r_1} - \frac{1}{r_2}\right) \tag{1}$$

From the geometrical considerations of Fig. 60 and the above equation, the following equation can be derived:

$$P = \frac{\sigma}{a}\left[\frac{(1 + \tan\theta)(1 - 2\tan\theta)}{\tan^2\theta}\right] \tag{2}$$

where a is the radius of the spheres. This equation may be placed in the form of a convenient plot, as shown in Fig. 61. Considering three spheres in mutual contact, pendular bodies will be joined when $2\theta = 30$ deg and a pendular-funicular transition

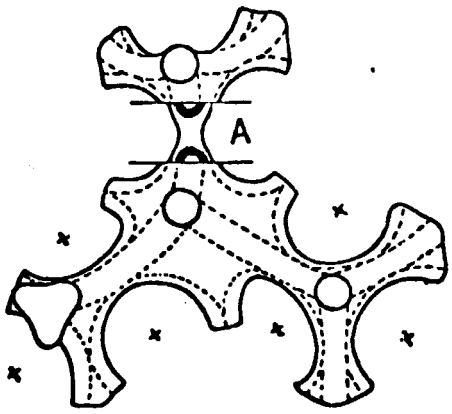

Fig. 59 Perspective Drawing Showing Shape of Continuous Gas Space at First Stage of Coalescence, With Development of Final Stage Shown at One Neck

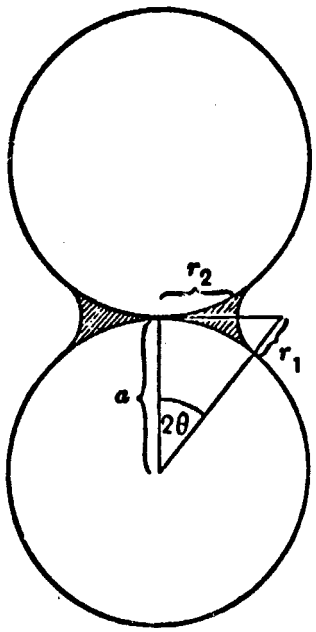

Fig. 60 Diagram Showing Annular Liquid Body Between Two Spheres

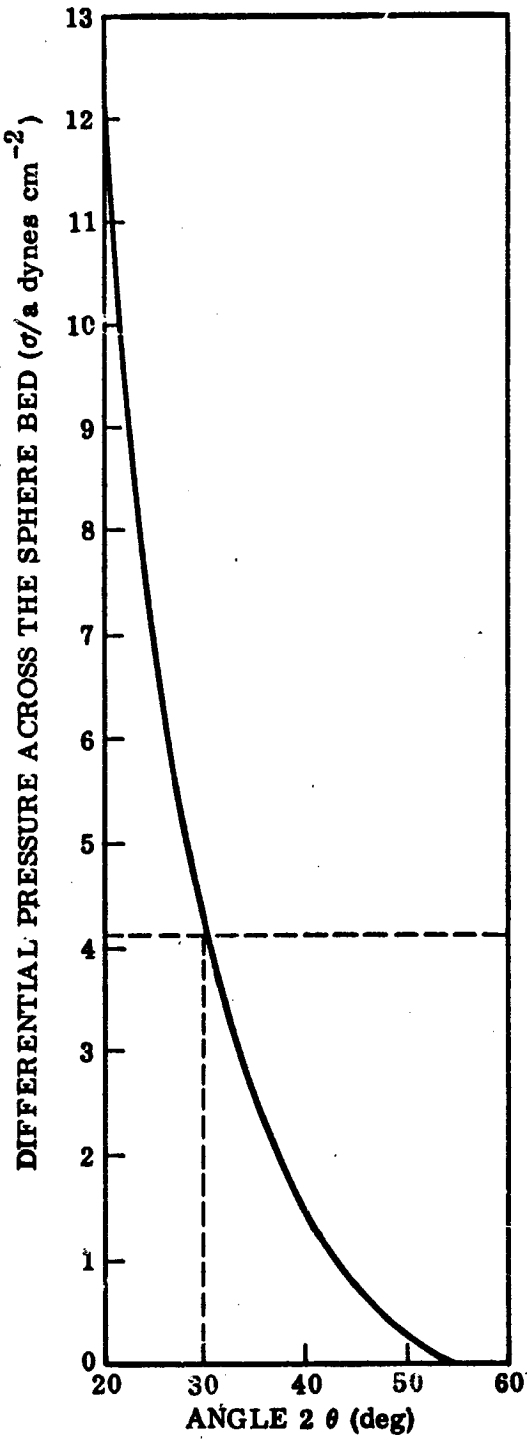

Fig. 61 Dependence of Internal Bulk Liquid Configuration on Differential Pressure for Ideal Sphere Bed

will take place, correspondingly, in a loosely packed sphere bed, provided three spheres are in mutual contact frequently enough so that the formed connections are continuous. From Eq. (2) and Fig. 61, it can be seen that for $2\theta = 30$ deg, the value of the differential pressure is $4.1\ \sigma/a$. For only a few degrees from 30 deg P may vary from 7 to 2 σ/a. The penetration pressure of the sphere bed should be approximately $4.5\ \sigma/a$ (e.g., see Ref. 5).

An expression for the fraction of surface area covered with liquid can also be made from the assumed geometry:

$$f = \frac{n}{2}(1 - \cos 2\theta) \tag{3}$$

where n is the number of nearest neighbors. In Fig. 62, f is plotted as a function of P and n with the use of Eqs. (2) and (3). Twelve nearest neighbors are present in a closest packing configuration with a fractional void volume (fvv) of 0.2595, whereas six nearest neighbors are present in a "most open" packing with a 0.4764 fvv. Our observed fvv is 0.41 (section 3.2). Using a linear correspondence, as suggested by Smith (Ref. 36), our beds have eight nearest neighbors and from Fig. 62 approximately 55 percent of the sphere surface is covered by bulk liquid for an ideal sphere bed with eight nearest neighbors. As the differential pressure is lowered below $4.1\ \sigma/a$, the remaining film area is quickly lost and vanishes at about $1.2\ \sigma/a$ for this idealized case.

5.3 CORRELATION WITH EXPERIMENT

The described observation of an optimum differential pressure for an oxygen gas electrode comprising a bed of spheres (section 4.2) is predicted by the p-f transition state theory. Also, the shape of the peak near the optimum differential pressure can be explained by the theory, e.g., Fig. 27. As pressure is increased and the f-p transition state is approached, a gradual formation of larger supermeniscus film areas would occur. For small differential pressures greater than the differential pressure at the optimum pressure, a sudden decrease in performance would occur as observed when the funicular filaments are ruptured.

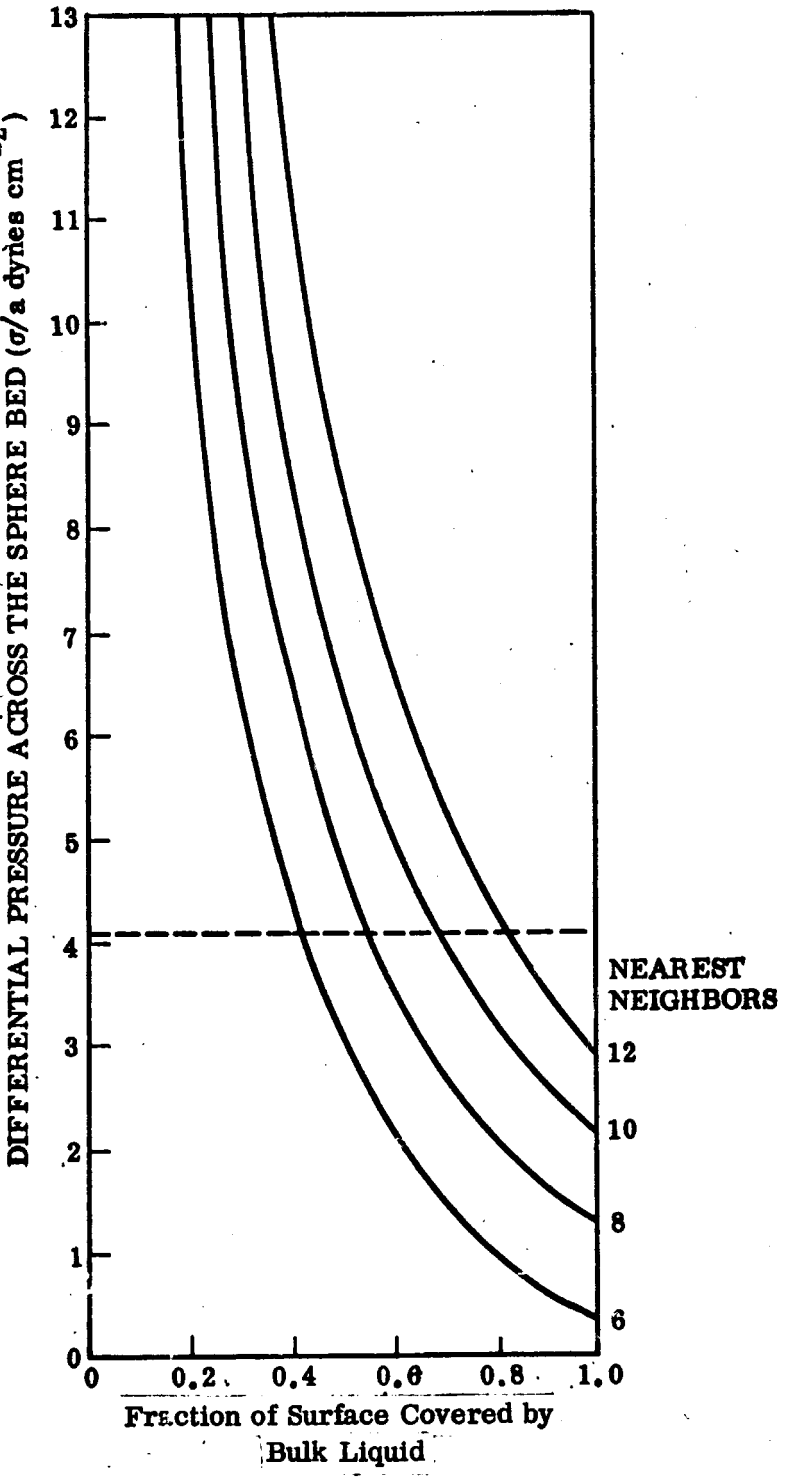

Fig. 62 Surface Coverage by Internal Bulk Liquid in Ideal Sphere Bed

By comparing the bubble pressure from a fritted glass disk in water and in 13.5 M KOH at 95°C, an evaluation of the surface tension of the 13.5 M KOH at 95°C was made and found to be 90 ± 1 dyne cm^{-1}. This value may be used to estimate the p-f transition differential pressure with the following equation:

$$P = 4.1 \frac{\sigma}{a} \tag{4}$$

For a bed of 156-μ spheres in contact with 13.5 M KOH at 95°C, P should be 48 cm of water, a value which should be compared with the measured 42 cm of water that was found after the sphere bed had been wetted but not completely flooded with a number of electrodes (e.g., Fig. 26). This agreement is considered to be good. It is noted that in the experiments of Section 4 the differential pressure was not cycled to determine a steady state optimum pressure. Instead, the pressure was only lowered from its initial value and then increased, and some incomplete wetting occurred, so that the observed optimum differential pressure should be somewhat less than the theoretical. In a similar experiment with glass spheres, 130 μ in diameter, Haines determined that for the first capillary rise and drainage the differential pressures should be 1.4 and 3.5 σ/a, respectively (Ref. 37). From the corresponding observations of Fig. 26, the values of 16 and 42 cm of water are used to estimate the surface tension of 13.5 M KOH at 95°C as 91 ± 3 dynes cm^{-1} which agrees well with the independently measured value of 90 ± 1 dyne cm^{-1}. The agreement with the theory is thus good considering that there is an 8-percent average deviation of the average sphere diameter of utilized 156-μ spheres and that only small deviations from the p-f transition configuration result in large changes in the optimum differential pressure, Fig. 61.

Indirect evidence for the theory can be obtained by comparing the work of Lindholm and Edwardsson (Ref. 24) and Haines (Ref. 1), who measured the ohmic resistance of liquid in porous media under partially flooded conditions. Haines made these measurements with the purpose of relating conductivity changes to the transition between the pendular and funicular regimes, while Lindholm and Edwardsson wished to relate the conductivity to the electrode performance. Examination of the conductivity curves (resistance curves) of both workers reveals a linear dependence until a

"shoulder" or change in slope is formed; Haines ascribes this shoulder to the transition between the two regimes, and from Lindholm and Edwardsson's work it can be seen that the shoulder corresponds approximately to the optimum differential pressure. The pendular-funicular transition and the appearance of an optimum differential pressure thus can be related by these two separate studies. This comparison may be considered as evidence of the importance of the funicular regime, removed by very small differential pressures from the pendular regime, as a condition where the film area is still maintained and where good ionic conductivity is supplied.

5.4 SUMMARY

A theory has been developed which explains that electrodes should be designed to be well characterized so that they can be used to provide a certain kind of controlled liquid distribution. The importance of the pendular-funicular transition state for internal liquid configuration was shown in its relation to the design and performance of oxygen gas electrodes.

Section 6
EFFECTS OF STRUCTURE DURING EVAPORATION

In this section, some effects of evaporation from gas electrodes are outlined. Gas electrode structure can have an additional influence in such cases. To adequately describe these evaporation effects, attention must be given to the pores and regions of the porous mass and to a method for representing the porous mass.

A pore may have changes in properties along its path for a continuous through-path from the gas side of the electrode to the bulk liquid. A sequence of zones may be present along this path, with each zone distinguished from others by differences in location and geometry and in physical and chemical properties. When these zones bear a certain relation to each other and to the porous mass and when some of these zones form regions which are free of liquid, evaporation from the electrode can materially affect performance. In this section, some of these relations and conditions are given for the zones and regions ("regions" being used to mean aggregates of zones having approximately the same properties).

To facilitate discussion, a system of symbols is introduced to represent a continuous through-path of an elementary pore with its zones in the following manner (e.g., see Ref. 38):

g/sg-1/sg-2/sg-3/.../slg-1/slg-2/slg-3/.../sl-1/sl-2/sl-3/.../1

In this system, the first letter represents the principal phase present, and, in the electrode, other letters consecutively represent the phases toward the central portion of the pore. Diagonal lines are used to separate zones having different pore properties which are numbered consecutively from the gas side for the gas-filled portions of the pores, sg; the liquid-filled portions, sl; and the gas-filled portions that contain a

liquid film coating the pore walls, slg. A series of such elementary paths, usually interconnected, is considered to form the electrode. A high degree of order of the zones may exist in regions that form layers parallel to the electrode faces, as in the double-porosity electrode, or order may be established in channels consisting of single pores or groups of pores in an interlaced and interconnected system, as in a Teflon-impregnated electrode. Capital letters are substituted for small letters when symbols represent regions having a higher degree of order or regularity of the pores (e.g., in Fig. 63).

6.1 THE PHENOMENA OF BUBBLING AND DISPLACED REGIONS, AND ELECTRODE DESIGN

In general, saturation should exist with water vapor in the gaseous portions of the slg zones. Here diffusion coefficients are on the order of 0.1 $cm^2 sec^{-1}$, and the pores are small (about 10^{-3} cm) so that $D/x \cong 100$ cm sec^{-1}. For an appreciable vapor pressure, it can be expected that saturation should be attained quickly in film-coated pores when the pore lengths are much greater than their effective diameters. Diffusion of gas toward slg can occur in the porous mass, with an accompanying total pressure build up at slg if slg is separated from g by a liquid-free or wet-proofed zone, sg, if the bulk gas is unsaturated in vapor and at a higher partial pressure at g than at slg, and if the pore at sg is sufficiently small (Ref. 39). It is necessary for some degree of order to exist and that dry regions be next to the gas region. Without order, the total pressure may be quickly relieved through pores connected to slg, and when slg zones are in contact with the gas region evaporation can saturate gas regions where the open mouths of the pores have dry or hydrophobic zones. As a general example, for the system G/SG/SLG/SL/L where the bulk gas is unsaturated in water vapor, evaporation from SLG and diffusion of vapor toward G will be accompanied by the formation of a water vapor partial pressure gradient in SG. For an initially constant total pressure in the pores, an equal and opposite partial pressure gradient of gas is formed, and gas is induced to diffuse toward SLG. If the pores of SG are small enough, e.g., less than about 0.1 μ in effective diameter at about room temperature and pressure (Ref. 40), and if bubbling is prevented, the total pressure in SLG will rise as gas diffuses

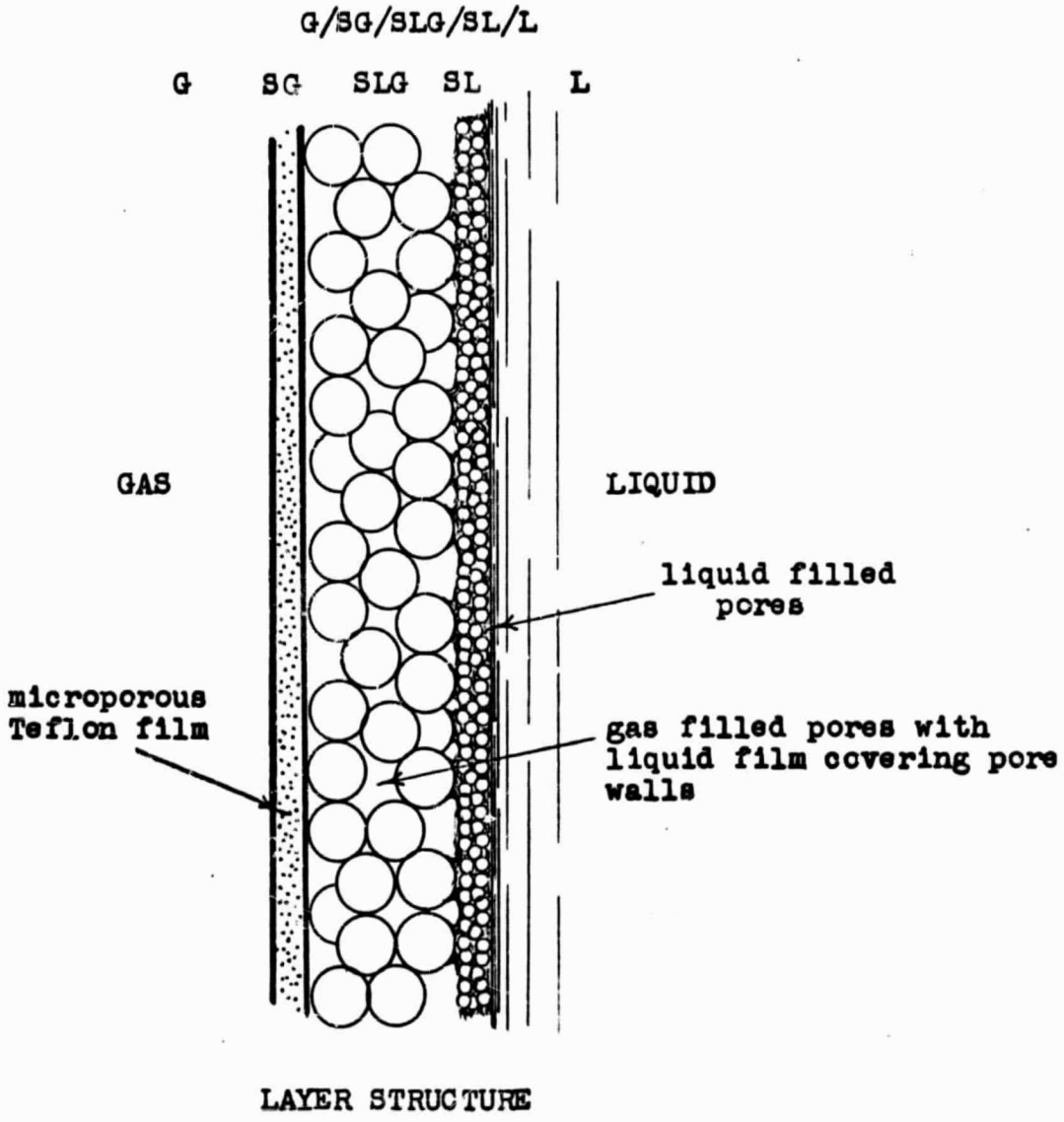

Fig. 63 Schematic Representation of a Double-Porosity Electrode With a Microporous Teflon Film

into SLG until the gas partial pressure at G equals the gas partial pressure in SLG. This diffusive process is independent of the total pressure difference. The maximum possible increase in pressure in SLG over that at G is thus the difference in water vapor partial pressures existing in these two regions. In practice, the increase may be expected to be somewhat less because of diffusion layers which are formed at the G/SG and SG/SLG interfaces and because of the wide distribution in pore sizes encountered with most porous media. The possibility of a total pressure buildup of this type was clearly shown by Wheeler in his treatment of catalyst pores (Ref. 40).

If the pores in SL are sufficiently large for the system G/SG/SLG/SL/L, the developed pressure may be relieved by the formation of bubbles, as shown in Fig. 64. This bubble formation can seriously disturb operation of a fuel cell system, and it constitutes a problem that has been studied by several workers (Refs. 41, 42, 43).

Bubbling can be prevented in the following ways: (1) The gas at G may be saturated in water vapor at the temperature of the operating electrode so that counter diffusion does not take place; (2) a total pressure may be applied to L, balancing the difference in water vapor partial pressure between G and SLG so that the gas partial pressure is constant; (3) a large fraction of the interconnected pores or all the isolated pores may be made to have their effective diameters in SG large enough so that convective interplay can offset the diffusive processes and relieve any developed total pressures toward the gas side, i.e., larger than about 1 μ for conditions near those of room temperature and pressure; or (4) the pores in SL may be made so small and hydrophilic that a bubble cannot be released because of the capillary attraction of the liquid. Actually, constant saturation of G is difficult during electrode operation because temperatures at SLG or SL may fluctuate and differ from those in G. Design considerations, such as the attainable electrode strength, often preclude application of pressure to L, so that the most practical approach is usually to control pore size at SG or SL.

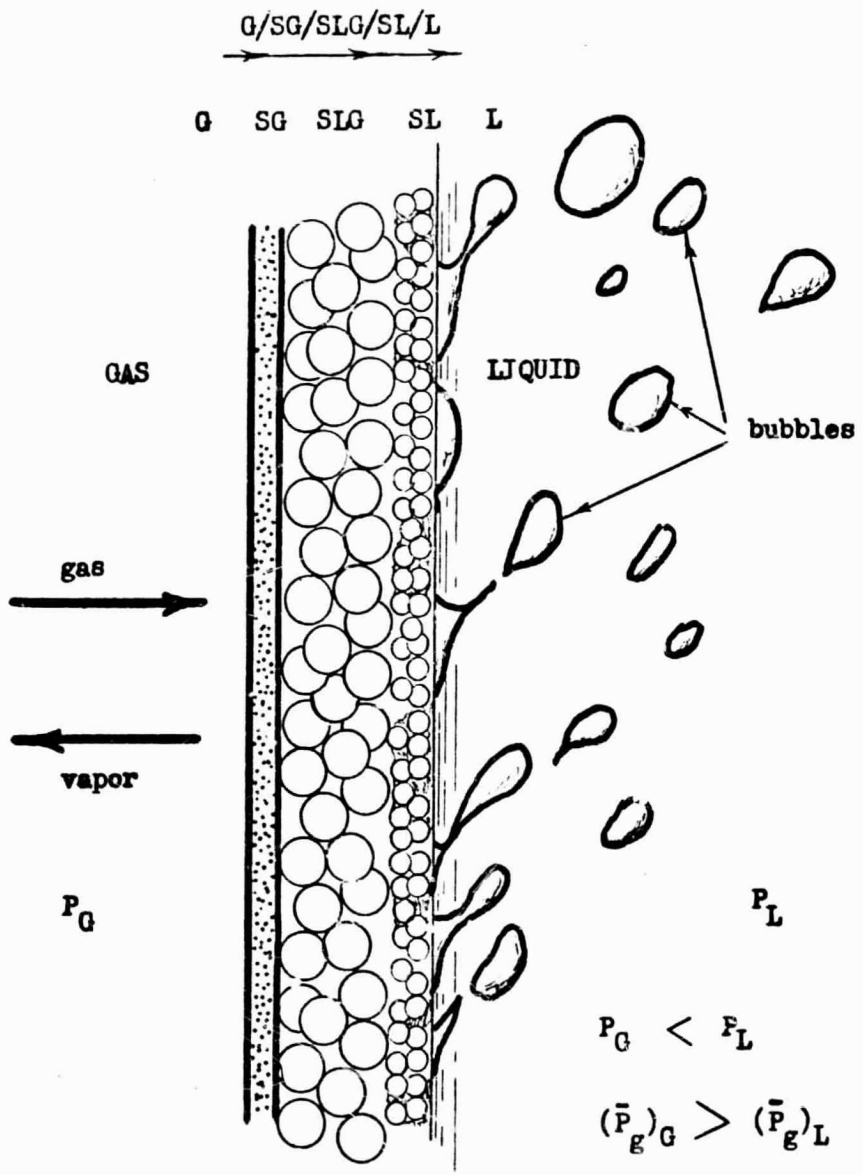

Fig. 64 Bubbling Caused by Evaporation

The total pressure at the electrode's gas side, P_G, is less than the total pressure in the electrolyte, P_L, but the partial pressure of the gas at the electrode's gas side, $(\bar{P}_g)_G$, is greater than its partial pressure in the electrolyte, $(\bar{P}_g)_L$.

A more subtle influence on electrode performance should result for evaporation from the system G/SG/SLG/SL-1/SL-2/L when pores in SG are sufficiently small, i.e., in the transition or Knudsen flow region (Ref. 43). The developed total pressure in SLG could displace electrolyte from SL-1, while the pores in SL-2 may be made so small that bubbling is prevented, as shown in Fig. 65. The occurrence of displacements of this kind was suggested by Palmer, Fishman, and Koslow (Ref. 44). It is further suggested that the formation of new SLG regions by pressure displacement may materially improve performance in some cases by making more void volume available for electrochemical reaction beneath a supermeniscus film which could extend throughout portions of this volume (Refs. 28, 45), by causing a more favorable pendular-funicular transition state, and by causing an increase in the partial gas pressure at SLG regions. A pressure balance is formed by which regions are made available for electrochemical reaction; i.e., the system would then be changed to G/SG/SLG-1/SLG-2/SL/L with SLG changed to SLG-1, SL-1 to SLG-2, and SL-2 to SL (Fig. 65).

Such pressure displacements may occur in Teflon-impregnated electrodes (Figs. 66 and 67) or in porous electrodes having a wet-proofing film placed on the gas side (Fig. 67), with an increase in the feed-gas partial pressure at SLG-1 and SLG-2. The region between the wet-proofing film and the intrinsic meniscus could be increased by the increased total pressure. With Teflon-impregnated electrodes, wet-proofed gas channels may form an interconnected network throughout the electrode mass. SL regions adjacent to this network are then changed to SLG regions. The advantage of this structure is in the possible presentment of short film lengths to the feed gas throughout the porous mass. The first lengths of the supermeniscus film contribute most to performance (Ref. 46), and a larger area of first lengths is made available throughout the electrode structure. A system resembling that of two superimposed scales of pore structure (Ref. 47) may be formed in which region SLG is connected to many different pores of the sl type leading to L. Similar advantages could result if the increased total pressure inside the electrode caused a favorable approach toward the formation of a pendular-funicular transition state, as described in Section 5.

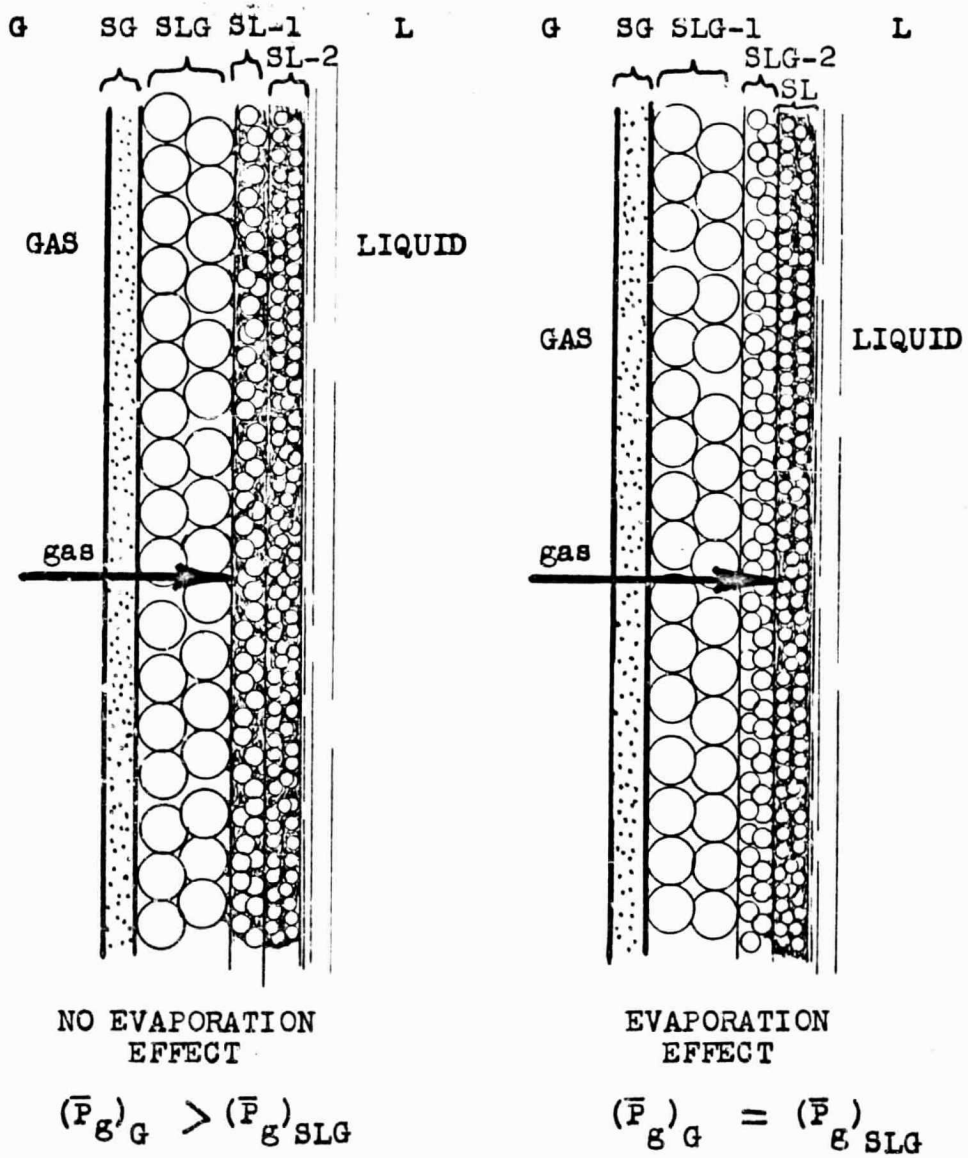

Fig. 65 Regions Displaced by Evaporation

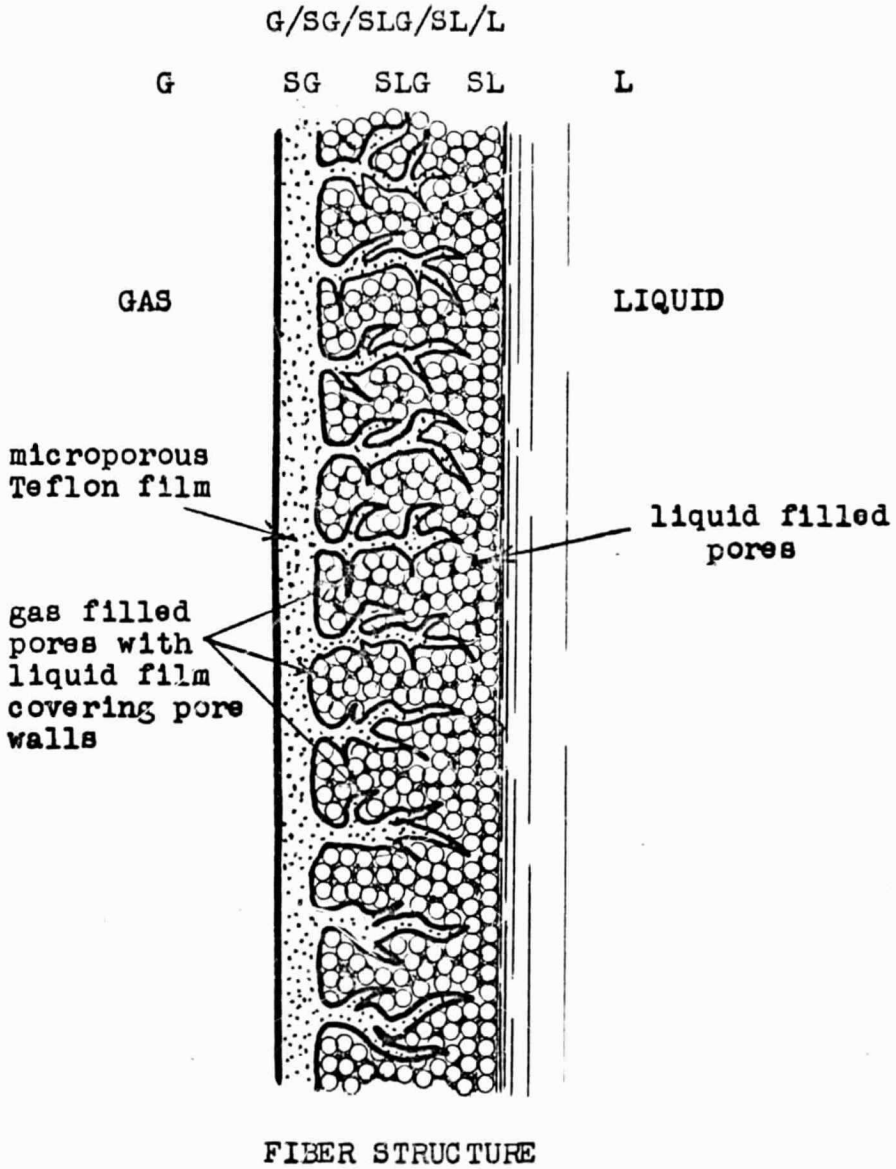

Fig. 66 Schematic Representation of Teflon-Impregnated Electrode Having Fibers of Teflon in the Porous Mass

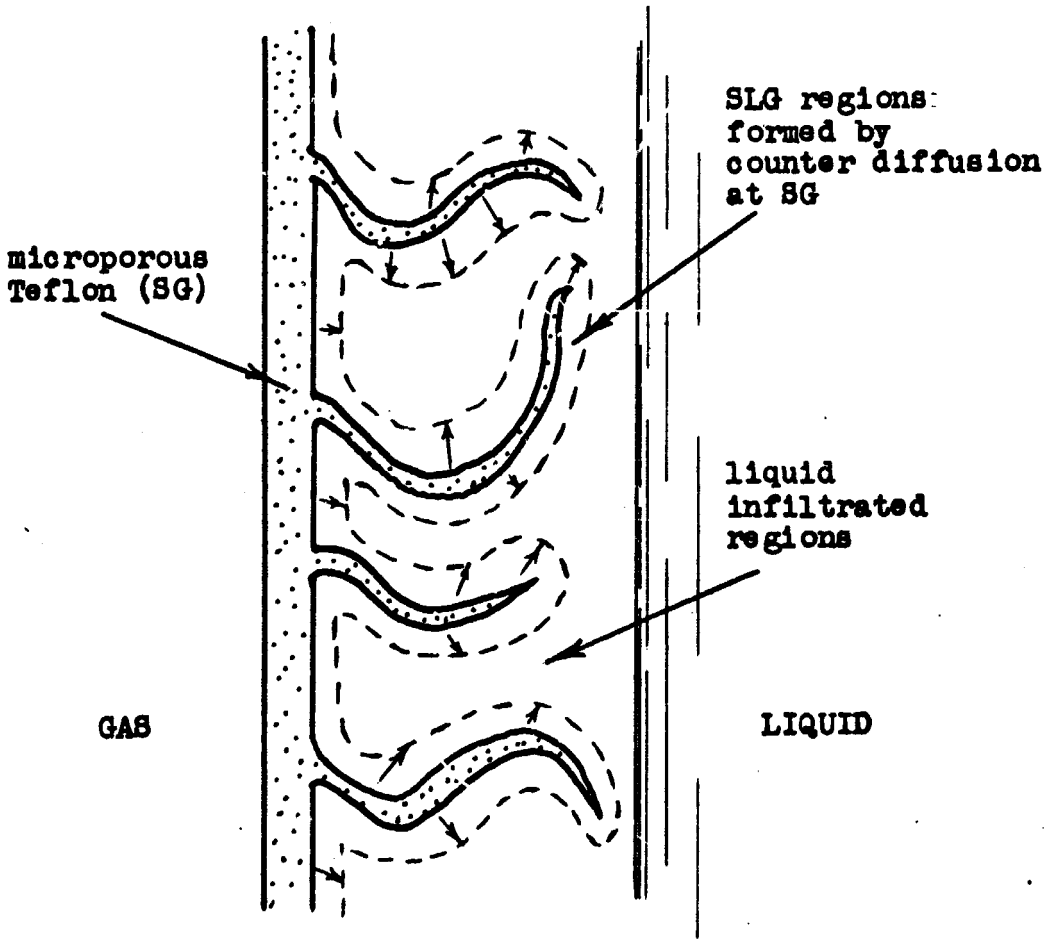

Fig. 67 Evaporation Effect With Porous Teflon Fiber Structure (gas flows through microporous Teflon filaments)

Another effect may result when sufficiently narrow pores are connected to large pores in the slg zones near sl or l. Induced gas flow into the narrow slg zones could develop a total pressure at slg which is easily relieved out of the large pore back toward g. A circulation of gas may develop, accompanied by evaporation as long as g is kept unsaturated at the mouth of the narrow pore.

In Fig. 68 a sketch is shown of this type of circulating electrode which may be generalized symbolically as follows:

Narrow: g/sg/slg-1/slg-2/sl/1

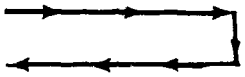

Wide: g/sg/slg-1/slg-2/sl/1

This type of design may be beneficial when continuous purging is required to remove inert impurities or contaminants (e.g., see Ref. 48). In other cases, it may bring water-saturated gas to cooler regions where condensation can cause blockage if pores in the cooler region are improperly designed (Ref. 41).

Evaporation is often encountered in fuel cell operation, and it is a natural consequence that effects such as those described should be considered in electrode design.

6.2 DESIGN METHODS FOR EVAPORATING ELECTRODES

The advantages of accurately placed regions of uniform pores cannot be easily realized because of present-day fabrication limitations and because pore sizes usually vary over a wide range. Pore zones may be randomly present which are in the Poiseuille, the Knudsen, and the transition ranges of size. Conversely, in considerations of electrode design even the description of porous masses can be difficult (Refs. 49, 50), and although several treatments for gas transport in gas-filled pores have been published (Refs. 51 – 55), it appears that they have not been

GAS

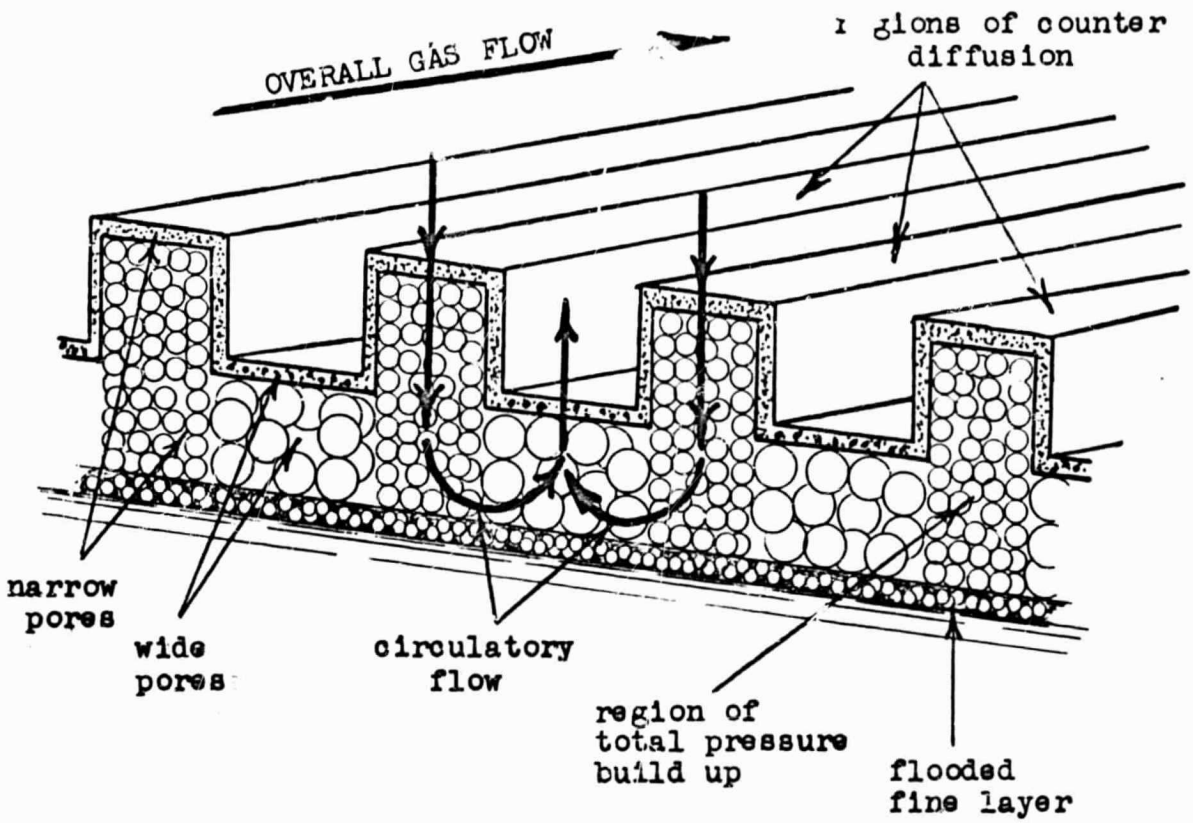

LIQUID

Fig. 68 Circulation of Feed Gas With Evaporation

applied to cases of evaporation from gas electrodes. Several design aids are available, however, which although approximate are useful as guides, and they are briefly outlined below.

In diffusion through porous media and in considerations of effective diffusion coefficients, the above cited works are helpful, together with some good reference works (e.g., Refs. 56, 57). The approximation technique suggested by Wheeler (Ref. 40) can be used by applying the Pollard-Present equation (Ref. 58) to estimate the diffusion coefficient in an ideal pore and to obtain an approximate value for the largest pore diameter for the onset of a total pressure gradient formation. In Fig. 69 the results of such an approximation are shown for the air-water system at 95°C. When the imaginary "Poiseuille Diffusion Coefficient" defined by Wheeler, D_p, has the value of the diffusion coefficient of air in water vapor in the example of an idealized cylindrical pore, the diffusive processes may be expected to become competitive with the convective processes, with consequent development of a total pressure gradient in a porous body having a pore size distribution with an average pore diameter which is equivalent to that of the cylinder. For the given example, such total pressure gradients become important in the transition range of flow or for pores with effective diameters less than about 3 μ. The results of this calculation are corroborated to some extent by experiments which have been conducted with microporous Teflon membranes (Ref. 43).

The equations developed by Stefan (Ref. 59) for the evaporation rate from a liquid at the end of a single pore may be used for the case of pores in a porous body with flow in the Poiseuille range to estimate evaporation rates. For transition range flow, Stefan's equations may be used with Poiseuille's law to estimate the manifested total pressure for small pressures as the pore diameter is assigned successively smaller values. Technically, such an application to the domain of transition range flow is incorrect, but even an approximation of this manifested total pressure for total pressures which are small compared with the value of the vapor pressure of the liquid is of interest in design. In Fig. 70 the results of such an approximation

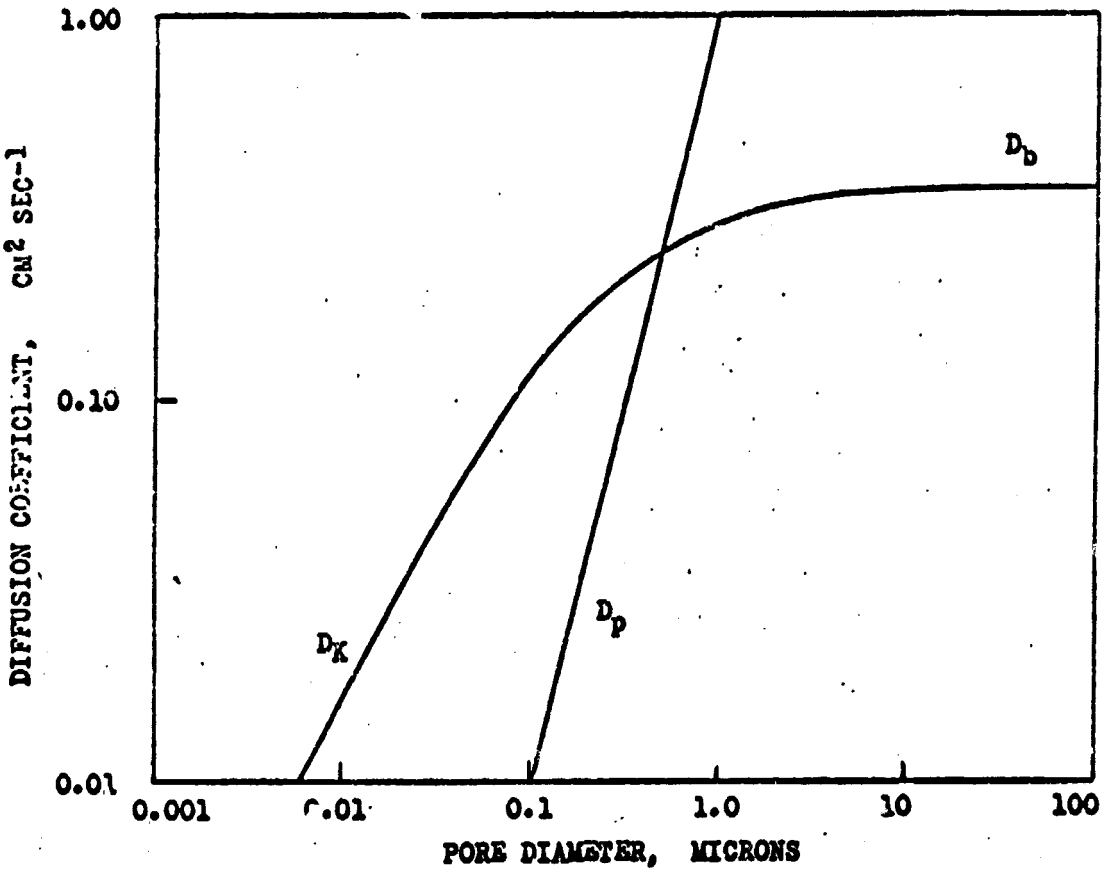

Fig. 69 Comparison of the Effective Poiseuille Diffusion Coefficient and the Pore Diffusion Coefficient Considering Onset of Knudsen Flow (Air-Water System at 95.0°C)

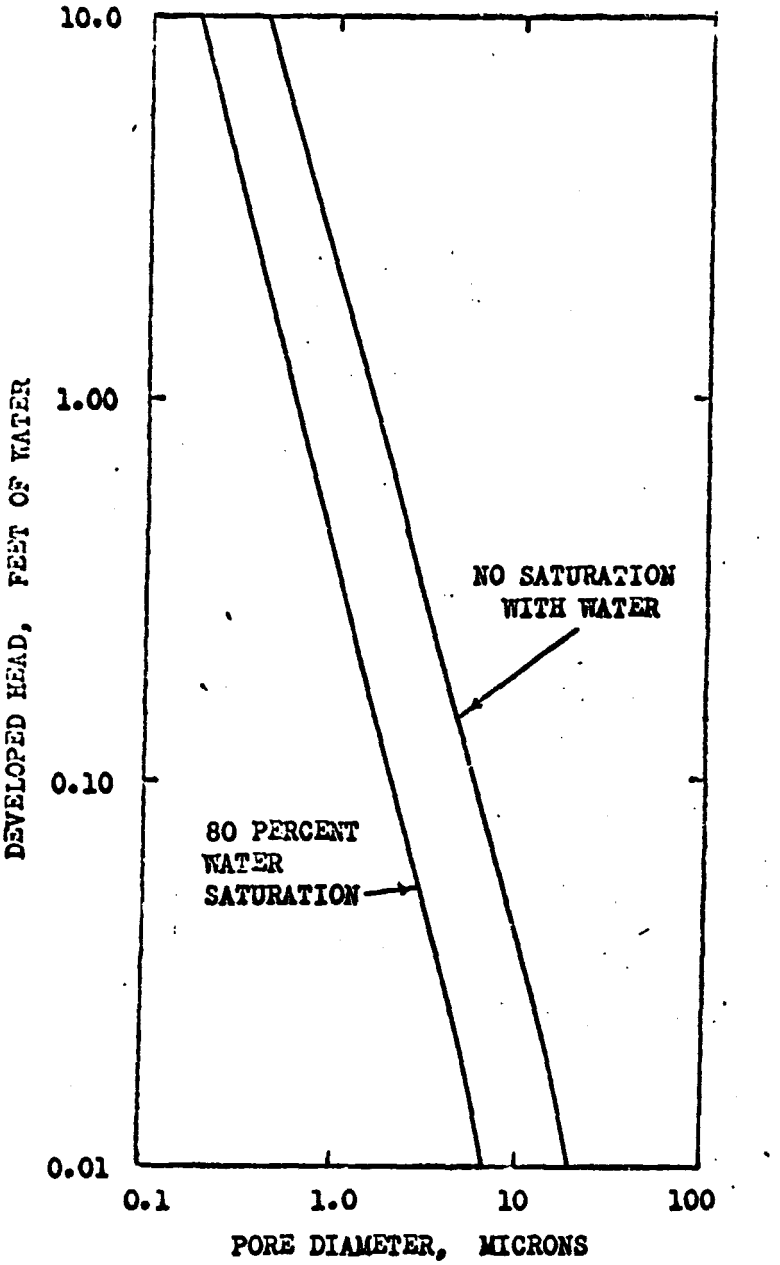

Fig. 70 Estimations of Developed Head for Various Pore Diameters Using Generated-Convective-Flow Approach (Air-Water System at 70.0°C)

are shown for unsaturated gas and gas which is 80 percent saturated in the vapor at the mouth of the pore. The possible developed pressure is seen to increase rapidly as the effective pore diameter is decreased below 1 to 10 μ. For pores much smaller than 1 to 10 μ when Knudsen flow is governing, the approximation can no longer be used, and the maximum possible manifested total pressure is the displacing vapor pressure of the electrolyte. This maximum is usually reduced by the formation of diffusion layers which are influenced by the gaseous flow rate past the electrode (Ref. 43).

Other theoretical tools are also available for use in the design of electrodes in accord with the described effects of evaporation. The treatment of Shropshire, Okrent, and Horowitz (Ref. 41) is convenient in predicting pore properties such as effective diameter and hydrophobicity which will prevent condensation within the pore, and a series of papers has been provided by Haines (Refs. 1, 3, 4, 60),who has experimentally and theoretically treated the pressure required to expel varying amounts of liquid from a bed of spheres (see also Ref. 5). These last results may be replaced by the classical expression for a cylindrical pore for some special electrode designs.

6.3 EXPERIMENTAL EVIDENCE FOR EVAPORATION EFFECTS

Although bubbling at fuel cell electrodes has been repeatedly observed (Refs. 41, 42, 43). there appears to be no known direct evidence of the other, beneficial effects outlined in this section. However, some indirect evidence was collected with a previously described apparatus (Ref. 43) which is capable of measuring induced gaseous fluxes through microporous Teflon membranes. In Fig. 71 are shown the results of such measurements with a randomly selected microporous TFE Teflon membrane 230 μ thick and 1.17 cm^2 in diameter. The data of Fig. 71 serve to confirm the practical import of the predicted effects caused by induced gaseous flow and spontaneously developed total pressures by indicating approximate values of the fluxes and pressures which are easily attainable when evaporation occurs at gas electrodes.

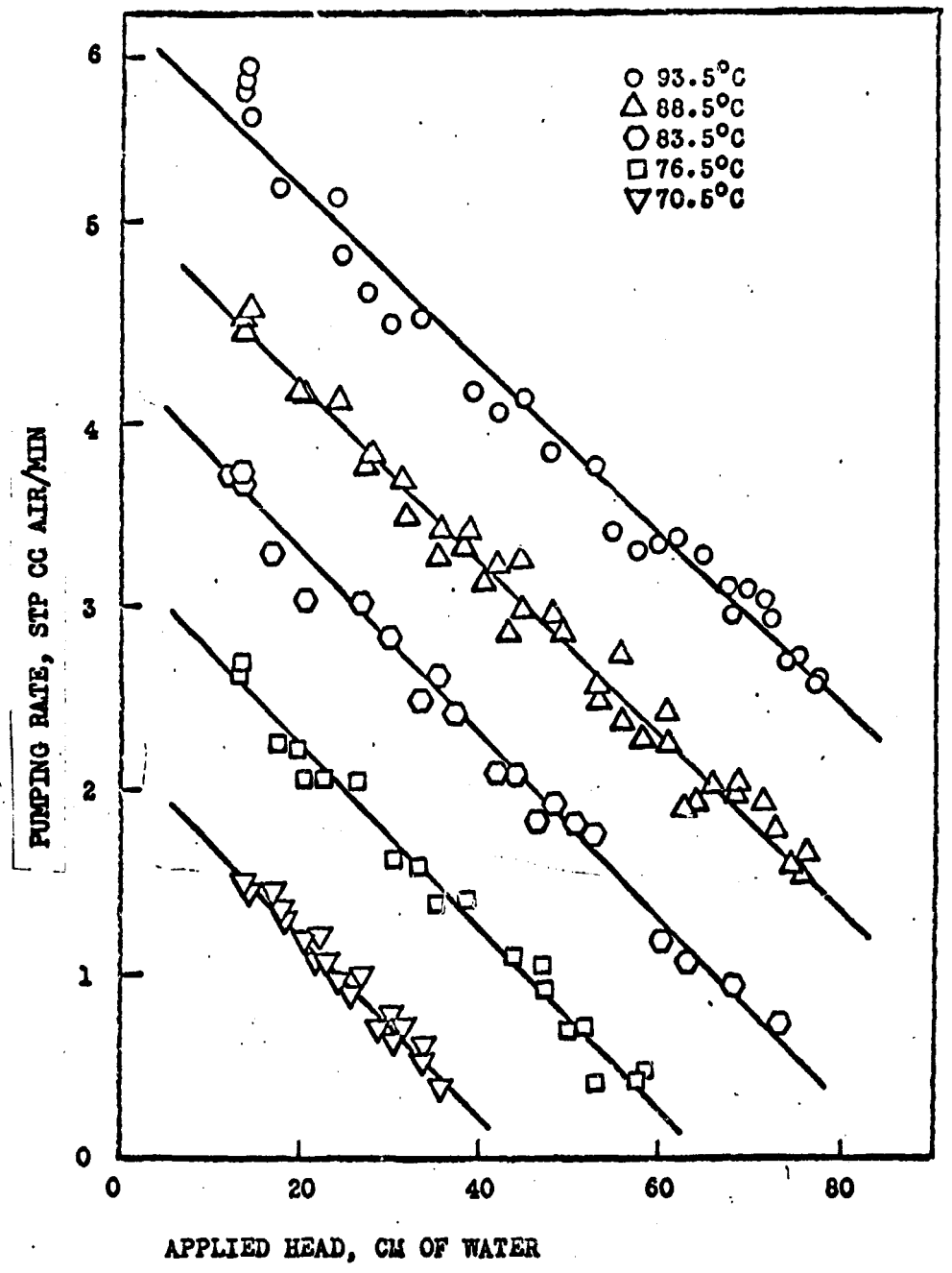

Fig. 71 Effect of Applied Head on Pumping Rate (Air-Water System; Flow-by Rate, 43.0 STP cc/min; 1.17 cm^2 Area; Microporous Teflon Membrane; 263 μ Thick)

For example, with oxygen with a 4-electron change per molecule, 1000 mA cm^{-2} is equivalent to

$$1 \frac{\text{coulomb}}{\text{sec}} \times 22,400 \text{ cm}^3 \text{ mole}^{-1} \times \frac{1}{4} \times \frac{1}{96,520 \text{ coulombs mole}^{-1}} \times 60 \text{ sec min}^{-1} \text{ cm}^{-2}$$

or 3.5 cm^3/cm^2 min of surface. From Fig. 71, it can be seen that this flux is obtained with the tested microporous Teflon membrane over a wide range of temperatures and developed total pressures. Such fluxes are practically possible. Also from the work of Haines and others (Refs. 1, 3, 4, 5) the pressure required to force a liquid from a sphere bed is about 4.1 σ/r where σ is the interfacial tension of the liquid in the sphere bed and r is the radius of the spheres. From the results of Section 4, a gas electrode may be designed to consist of spheres having a radius of 5.0×10^{-3} cm, and a typical value for σ may be 90 dynes cm^{-1}. The required pressure is then

$$4.1 \times \frac{90 \text{ dynes cm}^{-1}}{5.0 \times 10^{-3} \text{ cm}} \times \frac{1033 \text{ cm of } H_2O \text{ per atm}}{1.01 \times 10^6 \text{ dynes cm}^{-2} \text{ atm}^{-1}}$$

or 76 cm H_2O pressure. Such developed total pressures are practically possible, as shown in Fig. 71.

6.4 SUMMARY

Evaporation from the intrinsic meniscus and the supermeniscus film of fuel cell gas electrodes may cause counter diffusion of vapor and reactant gas in gas-filled pores of the porous mass. This counter diffusion may sustain a total pressure gradient and appreciably influence transport in the gas phase of the electrode. When evaporation occurs from gas electrodes in fuel cell systems, electrode designs which can accommodate the effects of counter diffusion should be considered. Important design parameters are the extent and position of hydrophilic, catalyzed regions of uniform pore size within the electrode; the placement of hydrophobic microporous regions for wet-proofing; and the pore size and extent of each region.

Section 7
RELATING STRUCTURAL PARAMETERS OF POROUS MEDIA

In this section, an idealized structure of porous media is treated to find typical relations between the structural parameters of porous systems. While it is recognized that the description of porous media is generally a difficult task (Ref. 49), simplified models of porous media have been presented for various purposes in the past (Refs. 8, 9, 10, 50, 51, 53, 54, 55, 61). These models usually satisfy certain requirements, but a model still appears to be needed specifically to relate the commonly accepted structural parameters of porous media. The parameters that are of concern in practical systems are the specific surface area, A, fractional void volume, θ, tortuosity factor, τ, effective pore radius, r, and solid radius, R.

In many fields, and especially in battery and fuel-cell electrode technology, it is necessary for the designer and fabricator to have a knowledge of the interrelations of structural parameters of porous media. At present, not only is the designer limited in his available knowledge of the effects of changing one or more parameters of complex structures of porous media but also the fabricator has no well-developed methods or clear guidelines for obtaining specified structures. Porous media are often expeditiously prepared with practical intent, without regard for the resulting complexity or effects on structure, and with poor understanding of the mutual influence of structural parameters.

It is the purpose of this section to present a scheme for theoretical but practical considerations of porous media and their structural parameters. A method or technique of developing imaginary structures is suggested which lends itself to facile, semi-quantitative interpretations for applications to design or fabrication. Examples are given in which the parameters are related and in which the effect is discussed of changing some of the structural parameters on the other structural parameters of the porous system. In this way, an attempt is made to bring some understanding and to supply a guide for work in porous media technology.

7.1 THE IDEALIZED MODEL

In this scheme, an idealized porous structure is postulated in which fibers are assumed to have their ends touching two parallel, facial planes of a porous mass. The fibers are assumed to comprise the solid part of the porous mass, to be electrically connected at the boundary of the facial planes, and to be positioned so that their ends are at the intercepts of Cartesian coordinate systems in the two planes. The effective pore radius is considered to be the radius of an imaginary pore which just fits between four fibers, as shown in Fig. 72. With this general model, further structural detail can be assigned depending on the construction materials used or on the desired resemblance to a given structure. A basis can be established for comparing and evaluating the structural parameters in terms of a model which approximates an actual electrode.

The idealized model enables some quick qualitative evaluations of the relations between A, θ, τ, and r, even without mathematical treatment. It is seen that variations in τ and $(1 - \theta)$ are more or less interchangeable and that other relations may be anticipated. The fibers may be placed as close to each other as required to vary porosity or fractional void volume, or they may be bent to change the tortuosity factor and porosity. Specific surface area may be changed in the same way. As r/R increases (e.g., see Fig. 72), so should θ, and an increase in τ should result in an increase in A. Fiber shape influences A. Fibers may be selected which are cylinders, stacks of spheres, or rods with square cross section. It should be noted that the peripheral area of a cylindrical fiber is the same as that for a fiber consisting of a stack of spheres with the same diameter and length. Also, cylindrical fibers can be notched, and it can be shown that for a cylinder of radius R with right angle, concentric notches with radius q and length l, the peripheral area per unit length of cylinder will be increased over that of the unnotched cylinder as long as $q + R > l$. Fibers of square cross section may be considered when it is required that the fibers completely fill the porous mass in the limit as they are made larger.

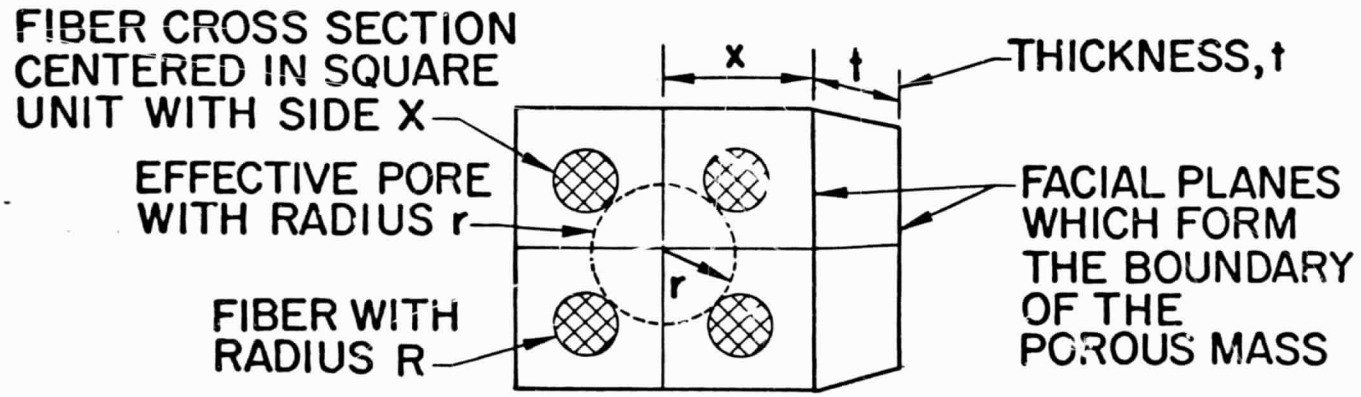

Fig. 72 Unit Section of Electrode Matrix With Four Fibers, Showing Location and Size of Pore

7.2 ANALYSES OF SPECIFIC SYSTEMS

In the following analyses, the ends of the fibers are considered to have negligible effect on the treatment. Tortuosity is taken as fiber tortuosity, and it is assumed that tortuosity is capable of unlimited variation within the confines of the unit fiber volume, x^2t. This last assumption introduces an impossible physical condition for large τ, and it should always be considered in interpretations of the mathematical treatments.

An analysis is made for the case in which the fibers consist of a row of spheres placed end-to-end. This structure resembles the loosely stacked spheres or particles used in a sintered fuel-cell electrode matrix or in a test electrode. The equations are derived by considering the cross-sectional relation of x, R, and r and by using the Pythagorean theorem,

$$x = \sqrt{2}\,(R + r) \tag{5}$$

Then, a unit volume, x^2t, is considered, and the fractional void volume is related to x, τ, and R:

$$(1 - \theta) = \frac{\text{sphere volume}}{\text{total volume}} = \frac{4/3\,\pi R^3(\tau t/2R)}{x^2t}$$

$$x = R\left[\frac{2\pi\tau}{3(1 - \theta)}\right]^{1/2} \tag{6}$$

Equations (5) and (6) are used together with the definition for A, i.e., unit area per unit volume of porous bulk, to obtain the following set of equations:

$$r = R\left\{\left[\frac{\pi\tau}{3(1 - \theta)}\right]^{1/2} - 1\right\} \tag{7}$$

$$A = \frac{3(1 - \theta)}{R} \tag{8}$$

$$A = \frac{\pi R\tau}{(R + r)^2} \tag{9}$$

A similar set of equations may be obtained for a rod fiber with a square cross section if the side of the square is taken as s:

$$r = \frac{s}{\sqrt{2}}\left[\left(\frac{\tau}{1-\theta}\right)^{1/2} - 1\right] \tag{10}$$

$$A = \frac{4(1-\theta)}{s} \tag{11}$$

$$A = \frac{4s\tau}{\left(\sqrt{2}\,r + s\right)^2} \tag{12}$$

The similarity of the functions for the two sets of equations should extend to other sets for cases in which the above derivation procedure is used. The minimum value for θ which is possible will vary depending on the selected fiber configuration. For $\tau = 1$, the following minimum values for θ can be determined:

For a fiber of spheres: $1 - \pi/6 = 0.4764 \leq \theta \leq 1$
For a cylindrical fiber: $1 - \pi/4 = 0.2146 \leq \theta \leq 1$
For a square fiber: $0 \leq \theta \leq 1$

The fractional void volume, θ, is 0.2595 for the closest packed arrangement of spheres.

7.3 DISCUSSION

The derived equations may be examined directly for interpretations of design and fabrication, but it is often advantageous to place the equations in the form of graphs so that trends and functional relations can be visualized. The graphs that are conveniently prepared are plots of r/R versus $1 - \theta$ and τ, A versus R, and τ versus $1 - \theta$. The equations and graphs are the tools that enable predictions in the relations between the structural parameters and that form the basis of electrode structure design recommendations.

Graphs are shown for the case of a fiber consisting of a stack of spheres in Figs. 73 through 76. In Fig. 73 is plotted r/R versus $1 - \theta$ for $\tau = 1$, 5, and 10. The fractional void volume is also shown. Here, it is seen how the increase in pore size or r/R results in an increase in porosity or 100 θ for a constant tortuosity. The porosity of a porous mass, for a constant tortuoisty factor, is most sensitive to changes in pore radius when the pore radius is very small. As the porosity approaches 100 percent, the pore radius or r/R approaches infinity. As the porosity approaches zero, the ratio r/R approaches a finite value depending on the minimum possible value of θ for a given value of τ which is compatible with physical reality.

In Fig. 74 is given the expected linear relation for τ and $1 - \theta$. A dashed line is included for $\tau = 1$ because physical meaning is lost for $\tau < 1$. This plot is interesting because reasonable values of the tortuosity factor are obtained, particularly for small values of tortuosity. Other relations are well shown. As tortuosity decreases, so does $1 - \theta$, and the slope for this decrease is greater for larger values of r/R. The latter effect can be readily understood because for larger effective pore radii or r/R the tortuosity must be greater to obtain a given porosity.

As the pore size or r/R is made larger for a given porosity, then the tortuosity must also increase so that the given porosity can be retained. This effect is shown in Fig. 75 for three different porosities. Finally, in Fig. 76 the increase of specific surface area to infinity is shown as the fiber (sphere) diameter is decreased to zero while the porosity is kept constant. The values of specific surface area in Fig. 76 are actually reasonable despite the generalizations and assumptions used in the model (e.g., Ref. 8).

With the presented scheme for treating structural parameters of porous media, the interrelations of the structural parameters can be easily shown (Figs. 73 through 76), at least in a semiquantitative fashion. The effect of changing any of the five structural parameters can be found at a glance with a suitable graph. For the three parameters, r/R, θ, and τ, the third is always set if the other two are fixed

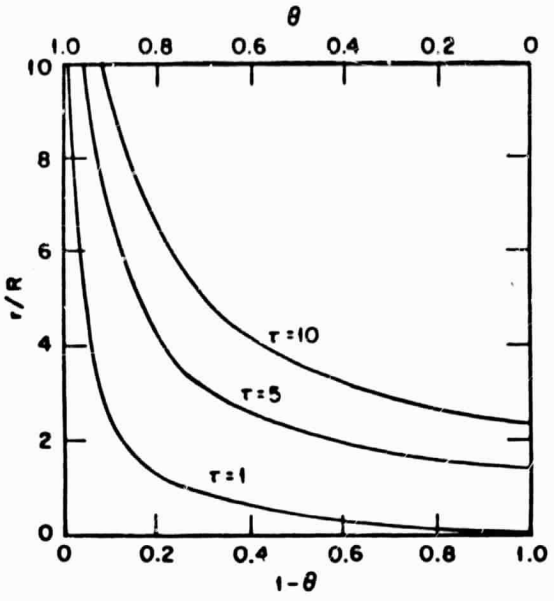

Fig. 73 Variation of Ratio of Pore Radius to Sphere Radius With Changes in Tortuosity Factor and Fractional Void Volume

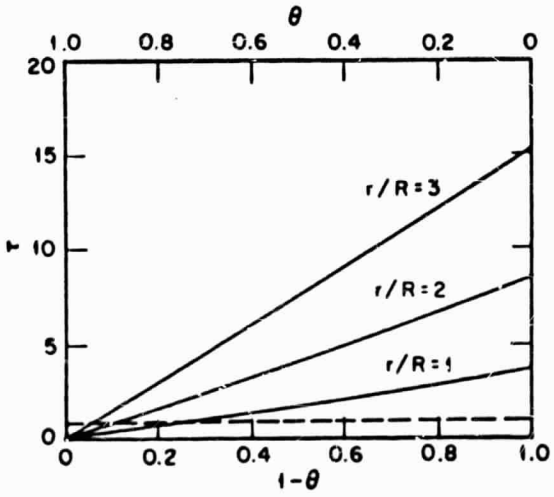

Fig. 74 Relation of Tortuosity to Porosity at Fixed Pore Radius and Sphere Radius Ratios

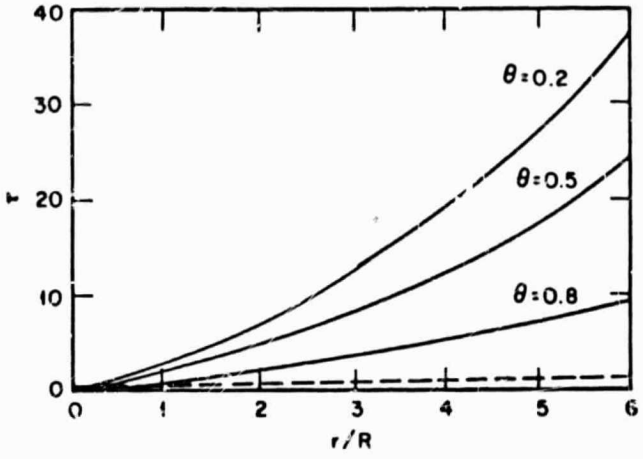

Fig. 75 Change of Pore Size With Changes in Tortuosity Factor for Fixed Fiber Size and Porosity

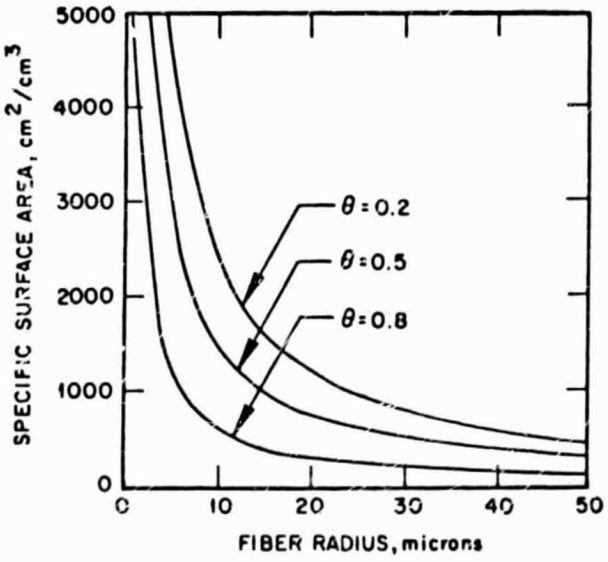

Fig. 76 Change in Specific Surface Area With Fiber Radius at Three Fractional Void Volumes

[Eq. (7)]. The specific surface area can be set by only θ and R [Eq. (8)] or by R, r, and τ [Eq. (9)].

The theoretical approach given in this section is necessarily general because every case will present a different challenge for a better fitted model and set of interrelations. Fiber structures closely resemble those structures encountered in practice. However, it is noted that the approach could be easily applied for the cases in which cylindrical pores or rods of voids are assumed to be interspersed in a solid block, i.e., the inverted form of the considered analyses.

7.4 CONCLUSIONS

The relations can be found between the structural parameters of idealized models which closely resemble actual porous media; i.e., the relations can be found between specific surface area, tortuosity factor, effective pore radius, effective fiber radius, and fractional void volume. These idealized models should find general application in the design and fabrication of complex porous media because a basis is formed for determining and understanding the principles relating the structural parameters. The idealized model may closely resemble a structure which is too complex for easy analysis. In this way, generalizations and semiquantitative evaluations can be made of the effect of changing some of the structural parameters on the others.

7.5 NOMENCLATURE

A = specific surface area of the porous media (cm^2/cm^3)
R = effective solid radius (cm)
r = effective pore radius (cm)
t = thickness of the porous media (cm)
τ = tortuosity factor of the fiber
x = side of a unit square housing one fiber (cm)
θ = fractional void volume

Section 8
SOME ELECTRODE RECOMMENDATIONS

Parameters of the electrode system are so interrelated that the considered electrode system must be specified before clear recommendations can be made. Throughout this report, general and specific design recommendations have been given for the sphere bed system. It is apparent that it is of prime importance to control liquid distribution and configuration and that this is best accomplished by using structures that are well characterized. An accurate control of differential pressure is indicated to maintain correct internal liquid configuration.

The use of a sphere bed system for the electrode structure has the advantage of simplicity with good characterization. Performances obtained in this study suggest that film-type oxygen electrode structures of this kind should yield satisfactory current densities over a range of polarizations in practical systems. Based on the results of this work, the following oxygen electrode structure is recommended:

Gas, oxygen, 13.7-psi differential pressure
1300-μ Ag, 7.8-μ diameter
400-μ Ag, 1.2-μ diameter
Liquid, 13.5 M KOH, 95°C

This recommendation is based on the assumption that the structure can be scaled down from that with the 156-μ spheres without sacrifices of performance by the onset of "film flooding." Supermeniscus films are probably on the order of ≤ 0.1-μ-thick (Ref. 13), so that two layers of film should just touch between three spheres which are $2(0.1)/0.155$ or 1.3 μ in diameter (Ref. 8), and film flooding should not be

serious. It is also assumed that the current density at a given potential is proportional to the specific surface area of the regular structure. In this connection, performance may be improved more than anticipated from a dependence on specific surface area because the isolated patches of supermeniscus films are made smaller and offer less resistance to ion transport.

With the 156-μ spheres, 50 mA cm^{-2} was obtained at 500 mV (Section 4). To obtain 1000 mA cm^{-2} at 500 mV [i.e., about 200 mA cm^{-2} at 900 mV (compare Fig. 25)], the sphere size should be (50/1000)156, or 7.8 μ. With the 156-μ spheres, the optimum differential pressure is 48 cm of water (Section 5), so this pressure should be (156/7.8)48 or 960 cm of water (i.e., 13.7 psi).

It is assumed that the optimum electrode thickness is not changed, and a fine-layer sphere size is selected which will cause the fine layer always to be flooded.

As a substrate to reduce cost, nickel spheres may be used which are silvered before assembly. The construction of the desired electrode may be accomplished by hot pressing at relatively high pressure and low temperature to minimize contact area loss, or by spark sintering (Refs. 62, 63), which is noted for its low area loss.

Some general recommendations may tentatively be made based on the findings of this investigation.

(1) A structure should be used which enables the formation of continuous networks of liquid and gas in the electrode (section 4.2). With this structure, internal liquid configuration should be controlled so that a suitable balance is obtained between liquid filaments or thickened film regions and the supermeniscus films as in the funicular regime near the funicular-to-pendular transition state (Section 5).

(2) Internal liquid configuration can be suitably controlled by using regular structures which allow regions of supermeniscus film to be periodically formed, distributed,and interspersed between continuous filaments of liquid at an optimum differential pressure (Section 5). Such structures may be sintered aggregates of spheres

or particles of uniform size. Liquid paths may be controlled by use of wedges which are uniformly distributed throughout the structure, as at the point of contact between two spheres or in cracks and valleys of irregularly shaped particles. Thin supermeniscus film areas, preferentially formed at convex surfaces, should be extensive enough and sufficiently numerous to account for approximately half of the specific area (section 5.2).

(3) Other techniques should be considered for obtaining the above-described liquid distribution throughout the porous mass. These may take the form of using a mixture of particles, some with roughened surfaces to bring in good ionically conducting paths of bulk liquid and others with smooth, convex surfaces for supermeniscus film formation; e.g., surface roughness may be accomplished by chemical deposition of platinum (section 4.7). Alternatively, the aforementioned roughened particles may have, instead, very fine through pores to serve the same function of bringing liquid in by capillarity. Another alternative may be to use a mixture of fine particles for capillary attraction of bulk liquid together with relatively large, smooth particles in a ratio which would not cause the flooding of the larger particles. In addition, a mixture of fine particles of a catalytic material and of a hydrophobic substance (e.g., Teflon) might be used if the proper ratio and structure could be obtained (section 4.11). With this mixture, continuous gas networks should form within and possibly on the surface of continuous networks of Teflon filaments which are porous. The interlacing continuous network of catalytic particles would draw bulk liquid in and throughout the electrode by capillarity to the liquid-gas interface, where Teflon filaments meet catalytic particle filaments and where gas is brought into contact with catalyst because of the hydrophobic properties of Teflon (Ref. 12), i.e., as in the Teflon-impregnated black-platinum electrode. Such techniques are limited by the imaginative approach of the designer and fabricator, and in each case the optimum differential pressure will change according to the structure used.

(4) Electrodes should be about 1300 μ thick at the optimum differential pressure according to the observations limited to this study. In the pendular regime, electrodes can be only 400 μ thick or less, depending on the differential pressure. In the funicular regime, near flooding, electrode thickness can be reduced to 120 μ for 38 μ spheres or less for smaller effective solid diameters in a loose sphere packing, although performances under these last two conditions are relatively poor (Section 4).

(5) The effective pore and solid radii should be made as small as possible before onset of flooding by supermeniscus films in the pores in order to maximize specific surface area. This limit will probably correspond to an effective pore radius of about 0.01 to 0.1μ or, for a loose sphere packing, to an effective solid diameter of about 0.13 to 1.3μ for a 0.4 fractional void volume. The limiting optimum differential pressures should then be from 820 to 82 psi, respectively (section 5.2), although the use of dispersed Teflon particles should reduce these values (section 4.11).

(6) Double-porosity structures should be used in the classical "Bacon sense" to prevent bubbling at the optimum differential pressure for the coarse layer and to gain resulting synergism (section 4.5). The pores in the fine layer should be completely flooded to increase ionic transport. Effective diameters in the fine layer then should be at least (4.1/1.2) or 3.4 times smaller than the effective diameter in the coarse layer (for loose-packed spheres) (section 5.2).

(7) In the use of wet-proofed structures from which evaporation of electrolyte occurs, advantage may be taken of the processes involving counter diffusion and an induced total pressure gradient to increase the internal reactant gas partial pressure to a value approaching the external gas partial pressure at the gas side of the electrode, to circulate gas, and to free flooded regions for electrochemical reaction (Section 6).

Appendix A

CALCULATION OF PERIMETER AND CROSS-SECTIONAL AREA OF CLOSE-PACKED ARRAYS OF SPHERES*

A.1 INTRODUCTION

In this appendix, the general equations for the positions of the sphere centers, for the cross-sectional area of metal in a horizontal plane, and for the wetted perimeter in a horizontal plane are developed for the two possible close-packed arrays that can be formed if the bottom layer is itself close packed.

A.2 PERIMETER AND CROSS-SECTIONAL AREA

If the first layer of a close-packed array of spheres is itself close packed, then the positions of the centers of the spheres in the first two layers are the same whether the array is hexagonal or close-packed cubic. Figure 77 shows the positions of the sphere centers, viewed from above, together with the sphere equators, for the first three layers. The array is disposed upon a set of coordinates, of which the origin is arbitrarily placed at the height of the centers of the spheres in the first layer, and along a vertical dropped from the center of a sphere in the third layer of a cubic array. In the horizontal plane the x and y axes are chosen such that the y axis is parallel to a line joining two nearest neighbor spheres in any layer.

---

*By A. J. Shaler, Consultant.

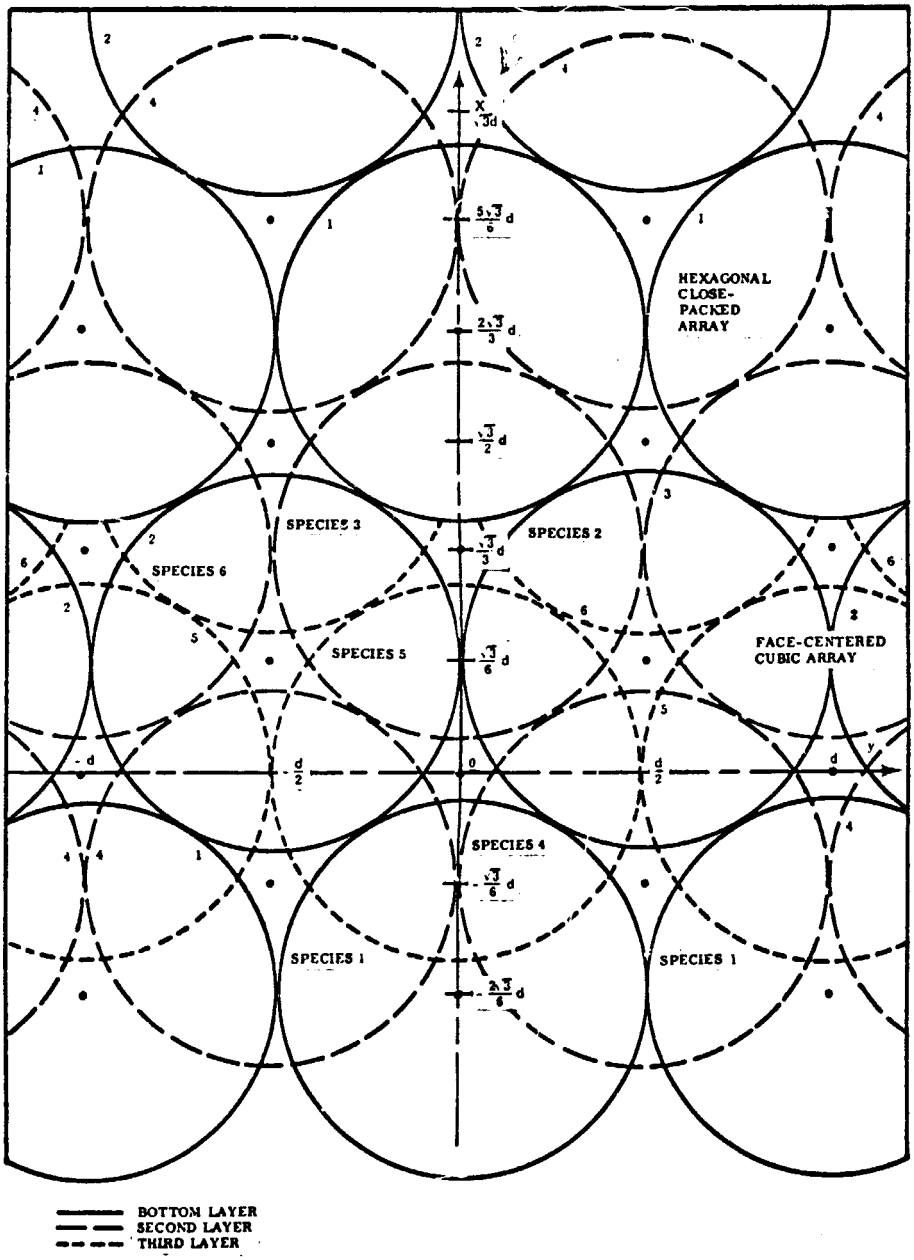

Fig. 77 Close-Packed Arrays of Spheres. Horizontal Planes

At the top of the figure, the solid lines are the equators of the spheres of the first layer in a hexagonal packing, the long-dashed circles are the equators of the spheres in the second layer, and the equators of the spheres in the third layer are, of course, superimposed upon those of the spheres in the first layer; this pattern is periodic upward from that third layer. In the middle third of the figure, a third set of circles is shown – the lines with the shorter dashes; these are the equators of the spheres in the third layer in a cubic packing.

In each layer, two species of spheres are shown: those with their centers on the x-axis and periodically one sphere diameter away from the previous one, and those with centers – half a sphere diameter away from the x-axis and periodically one sphere diameter away from the previous one. Thus, in the lower layer, species 1 and 2 are represented; in the second layer, species 3 and 4 are seen; and in the third layer, the species are again 1 and 2 in the hexagonal packing but 5 and 6 in the cubic. The pattern is made independent of the sphere diameter by scaling the axes as:

Multiples of $\sqrt{3}/6$ d in the x-direction (d = sphere diameter)
Multiples of d/2 in the y-direction
Multiples of $\sqrt{6}/3$ d in the z-direction (vertical)

In each horizontal (x-y) plane, the adjacent sphere centers form equilateral triangles of edge 2d. Thus, the centers are, for the six species of spheres, as follows:

Layer (From Screen)	Species	x_i	y_j	z_k
First	1	$(2+3i)\sqrt{3}d/3$	jd	$\sqrt{6}\,kd$
	2	$(1+6i)\sqrt{3}d/6$	$(1+2j)d/2$	$\sqrt{6}\,kd$
Second	3	$(1+3i)\sqrt{3}d/3$	jd	$(1+3k)\sqrt{6}d/3$
	4	$(5+6i)\sqrt{3}d/6$	$(1+2j)d/2$	$(1+3k)\sqrt{6}d/3$
Third (fcc only)	5	$\sqrt{3}id$	jd	$(2+3k)\sqrt{6}d/3$
	6	$(1+2i)\sqrt{3}d/2$	$(1+2j)d/2$	$(2+3k)\sqrt{6}d/3$

To determine the area attributable to a single sphere in the horizontal plane, one can begin with the equation for the surface of any sphere,

$$(x - x_i)^2 + (y - y_j)^2 + (z - z_k)^2 = d^2/4$$

At any integral value of k, a rectangle measuring one unit of i by one unit of j has an area of $\sqrt{3}d^2$. In that area are two full great circles of spheres, so the horizontal unit area per sphere center is $\sqrt{3}d^2/2$.

When any plane parallel to the x-y plane cuts horizontally through the array, it cuts either spheres of one layer only or spheres of two layers. In the first layer ($k = 0$), from $z = 0$ to $z = (\sqrt{6}/3 - 1/2)d$ it cuts spheres of layer 1; from $z = (\sqrt{6}/3 - 1/2)d$ to $z = d/2$ it cuts spheres of both the first and second layers. Thus, in the first of these ranges, the perimeters of species 1 and 2 are cut, and in the second, the perimeters of spheres of species 1, 2, 3, and 4 are cut. We need go no farther upward than $z = d/2$, since the pattern is then repeated equally in both the cubic and hexagonal arrays, but we must also find the special perimeter values from $z = 0$ to $z = -d/2$, where we encounter no new sphere layers but do find the screen.

If the screen opening is cylindrical and has a diameter s, then from $z = 0$ to $z = -\sqrt{d^2/4 - s^2/4}$ the spheres of species 1 and 2 only are cut. From that height down to $z = -d/2$, these spheres plus the screen are cut. The solid horizontal cross section of the screen is, in the unit area $\sqrt{3}d^2/2$, $\sqrt{3}d^2/2 - \pi s^2/4$ at any z below $z = -\sqrt{d^2/4 - s^2/4}$; its wetted perimeter in that area is, therefore, $2\pi/\sqrt{3}d^2$. The solid cross section per unit area is $1 - \pi s^2/2\sqrt{3}d^2$.

At any z, the perimeter per unit area of a sphere of layer 1 (species 1 and 2) is $(4\pi/\sqrt{3}d^2)\sqrt{d^2/4 - (z - z_k)^2}$. In the bottom layer, $k = 0$, so $z_k = 0$, and the perimeter is, from $z = -\sqrt{d^2/4 - s^2/4}$ to $z = (\sqrt{6}/3 - 1/2)d$,

$$(4\pi/\sqrt{3}d^2)\sqrt{d^2/4 - z^2}$$

Below the top level of the screen it is, from $z = -\sqrt{d^2/4 - s^2/4}$ to $z = -d/2$,

$$(4\pi/\sqrt{3}d^2)\sqrt{d^2/4 - z^2} + 2\pi s/\sqrt{3}d^2$$

and from $z = -d/2$ on downward it is

$$2\pi s/\sqrt{3}d^2$$

Above $z = (\sqrt{6}/3 - 1/2)d$, the plane z cuts spheres of layer 2 as well (species 3 and 4), so the perimeter is, from there to $z = d/2$

$$(4\pi/\sqrt{3}d^2)\left(\sqrt{d^2/4 - z^2} + \sqrt{2\sqrt{6}dz/3 - z^2 - 5d^2/12}\right)$$

To permit plotting the perimeter as a function of z, on coordinates in terms of d (to make them dimensionless in respect to the diameter of the spheres), it is further necessary to find a value of s in terms of d. We elect to define s such that the value of the cross-sectional area of metal, horizontally, per unit area of the screen, equals the least value of cross-sectional area of spheres from $-d/2$ to $+d/2$. The former is $1 - \pi s^2/2\sqrt{3}d^2$, and by inspection it is evident that the latter occurs infinitesimally above $z = -d/2$, just above the screen, where the cross-sectional area is always $\pi s^2/2\sqrt{3}d^2$. Therefore, $s = \sqrt{\sqrt{3}/\pi}\, d = 0.7425\, d$. If the cross section of the screen opening is hexagonal instead of round, this figure is $0.7241\, d$, and if it is triangular, $0.6458\, d$.

The cross-sectional area of the metal in the screen, per unit area as defined above, is then $1 - \pi s^2/2\sqrt{3}d^2 = 1/2$. For a hexagonal opening, it is 0.4756, and for a triangular opening, 0.3708. We can now numerically define the limits where the perimeter functions change as $z = 0.5000d$, $-0.3349d$, $0.3165d$, and $0.5000d$. The perimeters, computed from the expressions listed above for the various ranges, are shown in Fig. 78. To obtain the actual perimeter in centimeters (for example), at

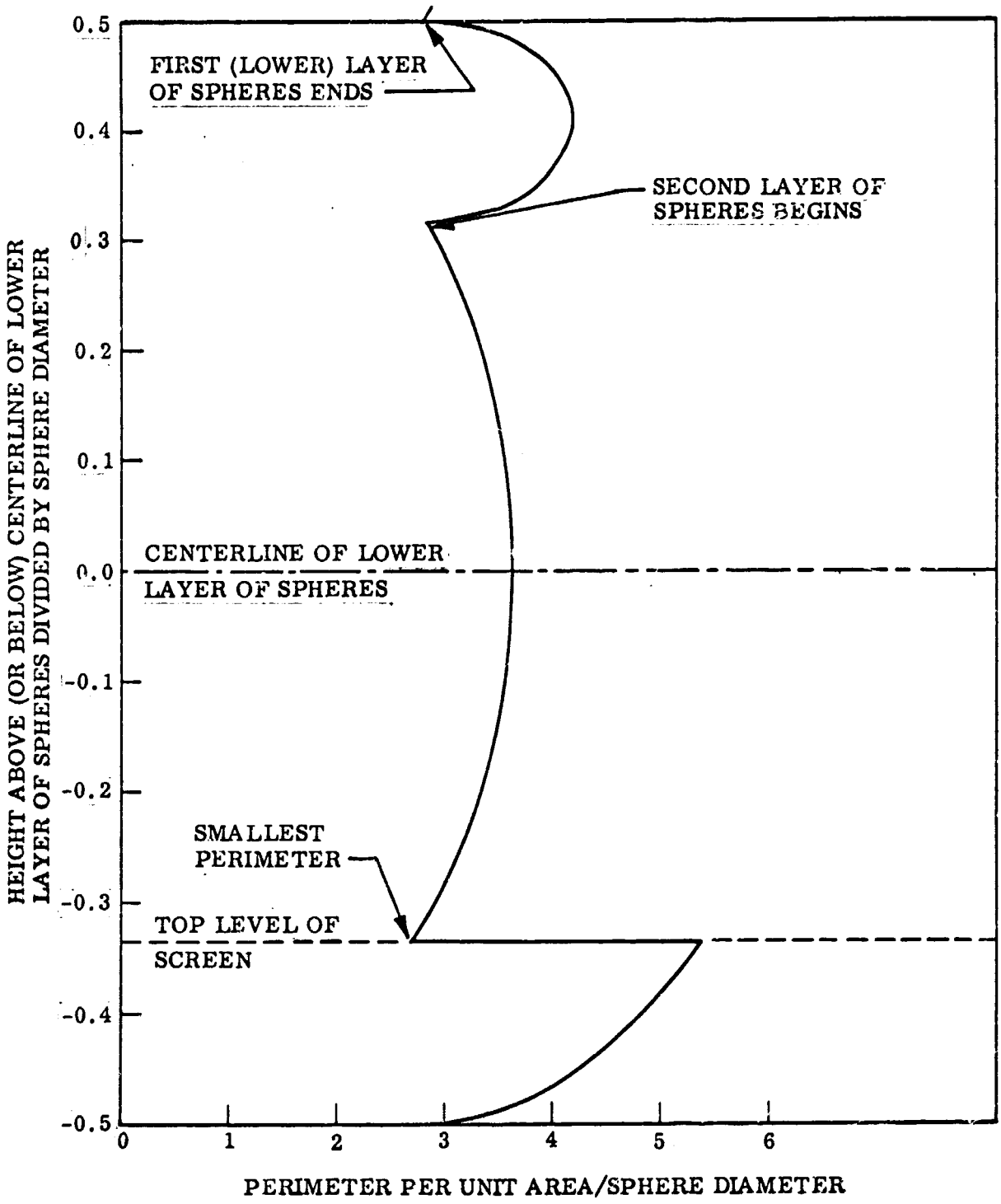

Fig. 78 Perimeter per Unit Area of Array of Spheres Lying on a Screen. Array is close packed in either face-centered cubic arrangement or hexagonal array. Screen opening is such that its cross-sectional area equals the minimum cross-sectional area of sphere array

any height z above the origin, it is sufficient to multiply the appropriate number on the ordinate by the sphere diameter d in centimeters, giving a value of z in centimeters, and to multiply the number corresponding to it on the abscissa by A/d, where A is the area in square centimeters for which the perimeter is required.

Thus, at the height marked 0.1, for spheres of diameter 100 μ (0.01 cm), the level is z = 0.001 cm above the origin, or 0.004349 cm above the top of the screen, and the perimeter per square centimeter of screen surface is marked 3.550, which corresponds to $3.550 \times 1/0.01 = 355$ cm/cm^2. In an electrode of horizontal cross-sectional area 0.1 cm^2, there would therefore be a wetted perimeter of 35.5 cm cut by a plane 0.004349 cm above the screen, the openings of which would be, if cylindrical, 0.007425 cm or 74.25 μ, in diameter.

The cross section of metal cut by a horizontal plane at any level z is similarly computed and shown in Fig. 79. Using the same 100 μ spheres at the same level, the abscissa reads 0.8706. Here the abscissa figures need only be multipled by A, so the cross-sectional area in an electrode of horizontal cross-sectional area 0.1 cm^2 at a level 0.004349 cm above the top of the screen is 0.08706 cm^2.

The formulations for the cross-sectional area of metal per unit area of horizontal plane at level z are:

From $z = -0.5000d$ downward	0.5000
From $z = -0.5000d$ up to $z = -0.3349d$	$(2\pi/\sqrt{3}d^2)(d^2/4 - z^2) + 1/2$
From $z = -0.3349d$ up to $z = 0.3165d$	$(2\pi/\sqrt{3}d^2)(d^2/4 - z^2)$
From $z = 0.3165d$ to $z = 0.5000d$	$(2\pi/\sqrt{3}d^2)(- d^2/6 - 2z^2 + 2\sqrt{6}dz/3)$

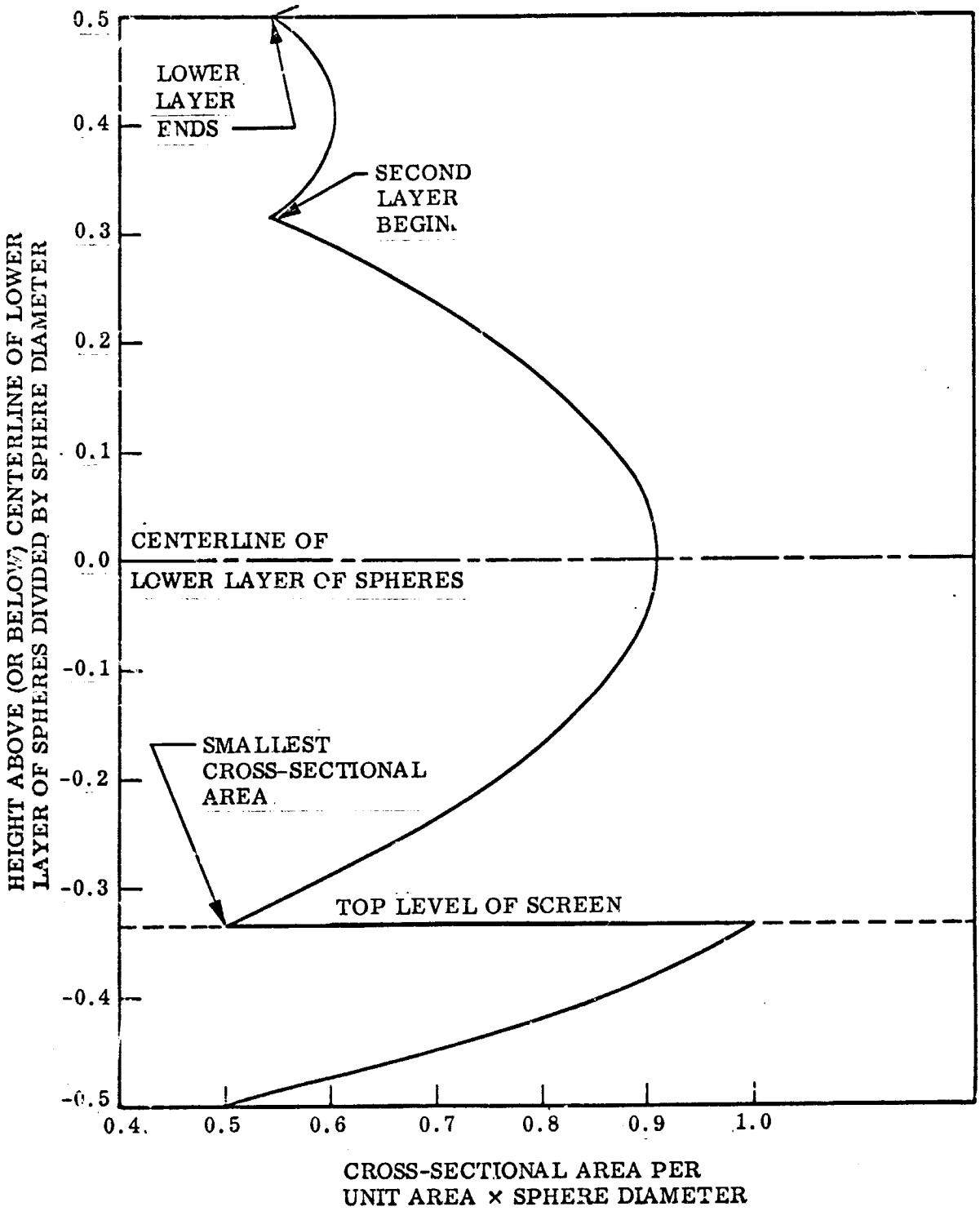

Fig. 79 Cross-Sectional Area of Metal per Unit Area of Array of Spheres Lying on a Screen. Array is close-packed in either face-centered cubic or hexagoal arrangement. Screen opening is round and is such that its cross-sectional area equals in metal the minimum metal cross-sectional area of sphere array

REFERENCES

1. W. B. Haines, J. Agr. Sci. 15, 529 (1925)
2. W. B. Haines, J. Agr. Sci. 15, 536 (1925)
3. W. B. Haines, J. Agr. Sci. 17, 264 (1927)
4. W. B. Haines, J. Agr. Sci. 20, 97 (1930)
5. R. P. Iczkowski, Ind. Eng. Chem. Fund. 7, 572 (1968)
6. A. J. Shaler, Int. J. Powder Metal. 1, 3 (1965)
7. S. Kruyer, Trans. Faraday Soc. 54, 1758 (1958)
8. J. M. DallaValle, Micromeritics, 2nd Ed., Pitman Publishing Corp., New York, 1948
9. A. E. Scheidegger, The Physics of Flow Through Porous Media, The Macmillan Co., New York, 1961
10. R. E. Collins, Flow of Fluids Through Porous Materials, Reinhold Publishing Corp., New York, 1961
11. A. H. Boerdijk, Philips Research Repts. 7, 303 (1952)
12. T. Katan, S. Szpak, and R. A. Botosan, "Development of Improved Electrodes for Fuel Cells," Bureau of Naval Weapons Contract NOw 64-0597-f, May 1965
13. T. Katan, S. Szpak, and E. A. Grens II, J. Electrochem. Soc. 112, 1166 (1965)
14. O. Loew, Ber. 23, 289 (1890)
15. Y. A. Mazitov, Elektrokhimiya 1, 349 (1965)
16. E. A. Grens, R. M. Turner, and T. Katan, Advanced Energy Conversion 4, 109 (1964)

17. E. W. Justi and A. W. Winsel, Fuel Cells, Franz Steiner Publisher, Wiesbaden, 1962

18. O. S. Ksenzhek, Fuel Cells, Ed. by V. S. Bagotskii and Yu. B. Vasil'ev, Consultants Bureau, New York, 1966, p. 1 (English Translation)

19. A. G. Pshenichnikov, Fuel Cells, Ed. by V. S. Bagotskii and Yu. B. Vasil'ev, Consultants Bureau, New York, 1966, p. 11 (English Translation)

20. I. Lindholm and I. Edwardsson, "Research on the Polarization in Porous Oxygen Electrodes," NASA Contract NASW – 15 36, First Quarterly Report, Jun 1967

21. O. Lindstrom, Energy Conversion 8, 33 (1968)

22. I. Lindholm and I. Jonsson, J. Electrochem. Soc. 116, 1150 (1969)

23. M. Bonnemay, G. Bronoel, and E. Levart, Electrochim Acta 9, 727 (1964)

24. I. Lindholm and I. Edwardsson,"Research on the Polarization in Porous Oxygen Electrodes," NASA Contract NASW – 1536, Third Quarterly Report, January 1968

25. T. Katan and S. Szpak, "Basic Studies on Fuel Cell Systems," Bureau of Naval Weapons Contract NOw 60-0738-d, Jul 1963

26. O. S. Ksenzhek, Russ. J. Phys. Chem. 37, 691 (1963)

27. H. J. R. Maget and R. Roethlein, J. Electrochem. Soc. 112, 1035 (1965)

28. R. H. Muller, J. Electrochem. Soc. 113, 943 (1966)

29. H. M. Cota, T. Katan, M. Chin, and F. J. Schoenewis, Nature 203, 1281 (1964)

30. R. A. Botosan and T. Katan, Electrochem. Tech. 5, 315 (1967)

31. R. Ch. Burshtein, M. R. Tarasevich, and S. Chernyshev, Extended Abstracts, 20th Meeting, CITCE, Strasbourg, Sep 1969

32. R. F. Amlie and R. Ruetschi, J. Electrochem. Soc. 108, 813 (1961)

33. G. C. Kuczynski, AIMME Transactions 185, 169 (1949)

34. R. Hultgren, Physical Metallurgy, Prentice-Hall, New York, 1952

35. W. J. Hamer and D. N. Craig, J. Electrochem. Soc. 104, 206 (1957)

36. W. O. Smith, Physics 4, 425 (1933)

37. W. B. Haines, J. Agr. Sci. 17, 286 (1927)

38. A. W. Winsel, Adv. Energy Conv. 3, 427 (1963)

39. T. Katan and G. W. Allen, J. Chem. Phys. 47, 1869 (1967)

40. A. Wheeler, Advan. Catalys. 3, 268 (1951)

41. J. A. Shropshire, E. H. Okrent, and H. H. Horowitz, Hydrocarbon Fuel Cell Technology, Academic Press, 1965, pp. 546 and 549

42. J. H. Fishman, R. H. Koslow, and N. I. Palmer, Nature 211, 1401 (1966)

43. T. Katan and G. W. Allen, Chem. Eng. Sci. 23, 739 (1968)

44. N. I. Palmer, J. H. Fishman, and R. H. Koslow, Deuxiemes Journees Internationales d'Etude des Piles a Combustible, Proceedings, p. 74, 1967

45. R. K. Burshtein, M. R. Tarasevich, S. F. Chernyshyov, and V. V. Karasev, Elektrokhim. 3, 907 (1967)

46. F. G. Will, J. Electrochem. Soc. 110, 145 (1963)

47. E. A. Grens II, I & EC Fundamentals 5, 542 (1966)

48. J. C. Jones and J. E. Cox, Energy Conv. 8, 113 (1968)

49. S. D. Holdsworth, Chemical and Process Engineering, 184 (April 1963)

50. A. J. de Bethune and R. L. Rowell, J. Phys. Chem. 67, 2065 (1963)

51. E. A. Mason, A. P. Malinauskas, and R. B. Evans III, J. Chem. Phys. 46, 3199 (1967)

52. E. Wicke and P. Hugo, Z. Phys. Chem. 28, 26 (1961)

53. R. N. Foster and J. B. Butt, A.I.Ch.E. 12, 180 (1966)

54. M. F. L. Johnson and W. E. Stewart, J. Catalysis 4, 248 (1965)

55. N. Wakao and J. M. Smith, Chem. Eng. Sci. 17, 825 (1962)

56. C. N. Satterfield and T. K. Sherwood, The Role of Diffusion in Catalysis, Addison-Wesley, 1963

57. E. E. Petersen, Chemical Reaction Analysis, Prentice-Hall, Englewood Cliffs, N. J., 1965

58. W. G. Pollard and R. D. Present, Phys. Rev. 73, 762 (1948)

59. J. Stefan, Sitzber. Akad. Wiss. Wien, Abt. II, 68, 385 (1873)

60. W. B. Haines, J. Agr. Sci. 15, 178 (1925)

61. D. H. Everett, The Structure and Properties of Porous Materials, Butterworths Scientific Publications, London, 1958, p. 95

62. U. S. Patent 3,241,956, Kiyoshi Inoue, 22 Mar 1966

63. U. S. Patent 3,250,892, Kiyoshi Inoue, 10 May 1966